LOW-DIMENSIONAL SUPRAMOLECULAR ARCHITECTURES AT METAL SURFACES

THÈSE N^{O} 3389 (2005)

PRÉSENTÉE À LA FACULTÉ SCIENCES DE BASE

Institut de physique des nanostructures

PROGRAMME DOCTORAL EN PHYSIQUE

ÉCOLE POLYTECHNIQUE FÉDÉRALE DE LAUSANNE

POUR L'OBTENTION DU GRADE DE DOCTEUR ÈS SCIENCES

PAR

Sebastian STEPANOW

Diplomphysiker, Friedrich-Schiller-Universität Jena, Allemagne
et de nationalité allemande

acceptée sur proposition du jury:

Prof. K. Kern, directeur de thèse
Dr R. Fasel, rapporteur
Dr M. Ruben, rapporteur
Prof. H. Vogel, rapporteur

Lausanne, EPFL
2005

Abstract

This thesis is concerned with supramolecular architectures assembled at metal surfaces. The investigations pursued two objectives. On the one hand, the focus was placed on the fabrication of low-dimensional surface-supported network structures by applying the concepts of conventional three-dimensional supramolecular chemistry at surfaces. Three main driving forces were explored for the construction of low-dimensional assemblies: hydrogen bonding, metal coordination and ionic interactions. The realized structures were characterized by scanning tunneling microscopy (STM) under ultra-high vacuum conditions. In particular, the interplay between the adsorbate-substrate coupling and lateral adsorbate interactions was addressed in the experiments. Further, the electronic and magnetic properties of the fabricated coordination structures were investigated. This characterization was done by x-ray absorption experiments at the synchrotron facility in Grenoble. Moreover, the response of the metal units and open cavity structures to the adsorption of large organic and small gas molecules was studied by temperature controlled STM experiments.

The first part of the thesis deals with hydrogen bonded supramolecular assemblies. Simple aromatic carboxylic acids were employed to study the assembly principles and in particular effects arising from the substrate and molecular structure. The investigation of TPA (1,4-benzenedicarboxylic acid) adlayers on Cu(100) at different substrate temperatures revealed how the protonation status of the carboxyl moieties affects the topology of the assemblies. Further, the influence of the molecular backbone functionality and symmetry is addressed in comparative investigations on TPA and PDA (2,5-pyrazinedicarboxylic acid) as well as BDA (4,4'-biphenyldicarboxylic acid) and SDA (4',4" *trans*-ethene-1,2-diyl-bisbenzoic acid) adlayers on Cu(100).

In the second part of the thesis, metal-ligand interactions were employed for the construction of supramolecular architectures at a Cu(100) surface. The concepts of conventional coordination chemistry were successfully applied at the surface. Iron atoms in conjunction with rod-like aromatic molecular linkers comprising carboxyl, pyridyl and hydroxyl functional groups assemble into a rich variety of open network structures with distinctly arranged mono- and diiron coordination centers and well-defined cavities. The results show that the adsorbate-substrate coupling considerably affects the local coordination environment of the iron units when the molecular backbone length is varied. The occurrence of structural isomerism in open network structures is addressed in a comparative study of heterofunctional and homofunctional linker molecules. It is shown that the former ligand allows only one topologically pure structure while the other linker forms two phases with different topology. The hydroxyl ligand has been used to construct distorted hexagonal coordination networks containing threefold coordinated single iron atoms. The comparison between the networks on Cu(100) and Ag(111) surfaces shows marked differences, which are attributed to adsorbate-substrate interactions. Finally, a novel design strategy for the fabrication of two-dimensional coordination structures at surfaces is introduced by using alkali metal ions in conjunction with carboxylate ligands. The interaction between the components is dominated by electrostatic forces and is of intermediate bond strength as in the case of hydrogen bonding and transition metal coordination. It is expected, that substrate symmetry and registry plays a larger role in the network formation, because the ionic interaction is not directional.

The chemical as well as magnetic properties of the fabricated coordination networks are examined in the last part of the thesis. The adsorption of C_{60} molecules on open network structures reveals how cavity size and chemical functionality affect the bond strength to the guest molecules as well as the number of accommodated C_{60} molecules. Since transition metal clusters, and in particular diiron units, are the catalytic active centers in various proteins, the reactivity of various mono- and diiron coordination structures to molecular oxygen was investigated in temperature controlled STM experiments. In particular, the focus was placed on the structural relaxation upon gas adsorption and chemical reaction. At last, the magnetic properties of the metal coordination centers are addressed in XMCD experiments. The iron units are found to be paramagnetic at temperatures down to 5 K and show distinct magnetic anisotropy and magnetization loops. These experiments demonstrate that surface-supported metal coordination structures are a promising class of materials for applications in the field of heterogenous catalysis and surface magnetism.

Kurzfassung

In der vorliegenden Dissertation wurde die Selbstorganisation supramolekularer Strukturen auf Metalloberflächen untersucht. Dabei wurden zwei Hauptziele verfolgt: Zum einen beschäftigt sich die Arbeit mit der Herstellung niedrig dimensionaler molekularer Netzwerkstrukturen auf Oberflächen mittels Anwendung der Konzepte konventioneller (3D) Koordinationschemie. Zu diesem Zwecke wurden die drei intermolekularen Kräfte, Wasserstoffbrücken, Metall-Koordinierung und elektrostatische Wechselwirkungen, zur Strukturbildung untersucht. Die erhaltenen supramolekularen Strukturen wurden mittels Rastertunnelmikroskopie unter Ultrahochvakuum Bedingungen charakterisiert. Dabei wird anhand der Strukturbildung versucht, das Zusammenspiel von Bindungskräften zwischen Molekül und Oberfläche sowie intermolekularen Wechselwirkungen herauszuarbeiten. Desweiteren wurden in der Arbeit die chemischen und magnetischen Eigenschaften der synthetisierten supramolekularen Strukturen untersucht. Letzteres wurde mittels Röntgenabsorptionspektroskopie (XAS, XMCD) am Synchrotron in Grenoble realisiert. Weiterhin wurden STM Experimente durchgeführt, um die Adsorption von großen organischen und kleinen Gasmolekülen an den hergestellten metall-organischen Netzwerke zu studieren.

Der erste Teil der Dissertation widmet sich den Wasserstoffbrücken gebundenen supramolekularen Strukturen. Es wurden einfache aromatische Karboxylsäuren verwendet, um die Auswirkungen des Substrates und der Molekülgeometrie auf die Strukturbildung der organischen Schichten zu studieren. Der Einfluß der Protonierung der Karboxylgruppen auf die Struktur der kompakten molekularen Inseln wurde am System TPA (1,4-Benzoldikarboxylsäure) auf Cu(100) untersucht. Desweiteren wurden die Auswirkungen der Molekülsymmetrie sowie der funktionellen Gruppen auf die Selbstorganisation in vergleichenden Studien an den Systemen TPA und PDA (2,5-Pyrazindikarboxylsäure) sowie BDA (4,4'-Biphenbyldikarboxylsäure) und SDA (4',4" *trans*-ethen-1,2-diyl-bisbenzolsäure) auf Cu(100) betrachtet.

Im zweiten Teil der Dissertation wird die Verwendung von Metall-Liganden Bindungen zur Herstellung von supramolekularen Strukturen auf einer Cu(100) Oberfläche besprochen. Die Prinzipien konventioneller (3D) Koordinationschemie wurden erfolgreich auf zwei dimensionale Systeme auf Oberflächen angewandt. Eine Reihe von Netzwerkstrukturen mit offenen Kavitäten konnte mit Hilfe von Eisenatomen und linearen organischen Molekülen mit funktionellen Enden wie Karboxyl-, Pyridyl- und Hydroxylgruppen realisiert werden. Die Strukturen sind charakterisiert durch die spezifische Anordnung von monoatomaren und dinuklearen Eisenkoordinationszentren sowie den wohldefinierten Kavitäten. Die Ergebnisse zeigen, daß die Adsorbat-Substrat Kopplung einen beträchtlichen Einfluß auf die Koordinationsgeometrie hat, wenn die Moleküllänge variiert wird. Das Auftreten von struktureller Isomerie in Netzwerkstrukturen ist Thema einer vergleichenden Studie zweier homo- und heterofunktionellen Liganden. Es wird gezeigt, daß die supramolekularen Strukturen des heterofunktionalen Moleküls mit einer Pyridyl- und einer Karboxylgruppe nur eine bestimmte Topologie aufweisen, wohingegen der andere Ligand mit zwei Karboxylgruppen isomerische Strukturen zeigt. Ein Molekül mit linear angeordneten Hydroxylgruppen wurde verwendet, um ein hexagonales Netzwerk mit dreifach koordinierten Eisenatomen zu synthetisieren. Der Vergleich zweier ähnlicher hexagonaler Strukturen auf Cu(100) und Ag(111) Substraten veranschaulicht direkt den Einfluß der Oberfläche auf das Koordinationsnetzwerk. Am Ende dieses Abschnitts wird eine neue Methode zur Herstellung von selbstorganisierten supramolekularen Strukturen auf Metalloberflächen eingeführt. Es wird demonstriert, daß sich langreichweitig geordnete Netzwerkstrukturen mit Hilfe von deprotonierten Karboxylsäuren und Alkali Ionen herstellen lassen. Die Wechselwirkung zwischen den einzelnen Komponenten wird dominiert durch elektrostatische Kräfte, die, wie im Falle von Wasserstoffbrücken und Metallkoordinierung, eine mittlere Bindungsstärke aufweisen. Es wird vermutet, daß die Symmetrie und Periodizität der Oberfläche eine größere Rolle bei der Netzwerkbildung spielt, da die elektrostatischen Kräfte ungerichtet sind.

Die chemischen und magnetischen Eigenschaften der realisierten Koordinationsnetzwerke werden im letzten Teil der Dissertation betrachtet. Der Einfluß der topologischen und chemischen Eigenschaften der Netzwerkkavitäten auf die Adsorption von organischen Molekülen wurde in STM Experimenten untersucht. Da Übergangsmetallcluster, und im besonderen dinukleare Eisenzentren, die katalytisch aktiven Zentren von diversen Proteinen repräsentieren, wurde die Reaktivität der Eisen koordinierten Netzwerkstrukturen mit molekularen Sauerstoff untersucht. Dabei interessierte im besonderen die thermische Stabilität der Koordinationsstrukturen. In XMCD Experimenten wurden die magnetischen Eigenschaften der Eisenatome bestimmt. Diese zeigen paramagnetisches Verhalten bis zu Temperaturen von 5 K. Desweiteren wurde die magnetische Anisotropie und das Magnetisierungsverhalten ermittelt.

Contents

Introduction

At the beginning of the 20th century quantum mechanics lead to the detailed understanding of the properties of condensed matter. Physical quantities like electric and heat conductivity, magnetization, mechanical parameters and chemical reactivity emerge from the peculiar behavior of nuclei and electrons. As a consequence a rapid evolution in understanding of the fundamental properties of matter took place. The development of novel experimental and theoretical tools has made big advances in the interdisciplinary domain of materials research, in which biology, chemistry and physics merge into a flourishing field. One of the most prominent successes of materials science are the advances in semiconductor research. Like no other field it demonstrates so clearly the fruitful entanglement of basic research and developments in material fabrication and preparation. In the last decades, the technological progress allows for the advanced control of matter at the atomic level. Molecules and atoms can be arranged into architectures of predesigned shape, size and chemical composition. On the other hand, the study of physical properties with high sensitivity and unprecedented structural and chemical detail has been made possible. As the size of the structures shrinks their properties deviate dramatically from those in bulk systems. The investigations and manipulation of such objects with dimensions smaller than 100 nm and that are composed of a few (up to 10^6) atoms or molecules are summarized by the term nanoscience. Since novel and intriguing phenomena emerge from the reduction in size nanoscience has attracted wide interest from both a fundamental research and a technological point of view. Besides the fascinating fabrication capabilities of conventional crystal growth and preparation techniques as well as other methods, supramolecular chemistry with its profusion of molecule-based compounds and processes constitutes an appealing method for engineering novel functional systems. The various coupling and molecular recognition schemes with intermediate bond strength enable the direct control of the materials' topology and functionality. Along with the quasi-infinite abundance of different molecules this method opens the way towards novel functional materials with unprecedented properties.

Interfaces and surfaces are of great scientific interest, since they play a major role in modern technology. At the surface a rich variety of physical phenomena is encountered partially arising from the altered structure and electronic states at the boundary of condensed matter. Furthermore, the surface is the place where different materials come into contact and possibly undergo chemical reactions. Interesting physical effects are also present when light interacts with the first few atomic layers at interfaces and the behavior of electrons and holes at the interface of non–metals is extensively exploited in semiconductor heterostructures. Thus, the chemical quality and morphology of interfaces (a surface is merely the interface between the solid/liquid and the air/vacuum) are decisive for many applications. With the advent of the scanning probe techniques in the 1980's the detailed evaluation of materials and structures has been made possible. By the increasing capabilities of fabricating nanostructured surfaces nanoscience has become a new flourishing research field. Among various tools, scanning tunneling microscopy (STM) provides a unique real–space resolution of conductive surfaces at the air/vacuum or liquid interface. In addition, its spectroscopic capability allows to obtain detailed chemical and electronic information at the atomic scale [1, 2]. Supported by computational modeling and in combination with other spectroscopic methods it has demonstrated its importance in a vast amount of studies for the elucidation of fundamental phenomena in surface chemistry in exquisite detail: topology of supramolecular assemblies and molecular conformations [3–12], chiral specificity [4, 7, 13–17], pathways of chemical reactions [2, 18–22], catalytic functionality [23–25] and ultra-thin magnetic films [26–28].

The structuring and functionalization of surfaces is of great technological interest for many applications. Among other approaches the deposition of molecules on surfaces, which bind in a specific way to it, is a promising way to bestow the substrate with certain chemical properties resulting from the molecular functionality. This process requires the detailed understanding of the coupling schemes of adsorbed molecules, i.e., the interplay between the inter-adsorbate and adsorbate-substrate interactions arising from their functional groups. These investigations on the organization principles open novel avenues for the molecular engineering of nanostructured surfaces with potential applications in the fields of molecular (opto-) electronics, chemical sensing as well as heterogenous catalysis. At the beginning of this approach it is of great importance to achieve control on the growth process, and thus, to relate the physical and chemical properties to the structural characteristics of the system. Apart from that, there is also a basic interest to study local elementary processes in chemistry or complex biological systems at surfaces.

The fabrication of surface-supported nanostructures is divided up into two main strategies: the top-down versus the bottom-up approach. Both approaches comprise a rich variety of tools with their specific advantages and drawbacks. While there is an ongoing technological progress over a few decades in the development of (photo)-lithography and other top-down methods, the manipulation of matter at the atomic scale is still in its infancy. Recent advances in the atom-by-atom manipulation by scanning probes demonstrate the increasing flexibility and precision of these techniques, but allow to create only a very limited number of structures per unit area of the sample [29–32]. Moreover, the time consumption for the construction of artificial structures by one atom at a time makes such architectures only interesting for fundamental research activities.

Molecular self-assembly, on the other hand, relies on the specific interactions between complex molecules comprising a vast variety of functional groups. Self–organization describes the modular assembly of simple building blocks into complex architectures, whose topology is determined by the kinetics and thermodynamics of the assembly process. The abundance of self-assembly processes in nature clearly demonstrates its power in the construction of functional biological structures. In the past decades the molecular level design of new materials [33–36] has expanded extensively in the interdisciplinary fields of crystal engineering [37–39] and supramolecular chemistry [40–42]. The employed design principles benefit from investigations of biological system, where a rich variety of coupling schemes and recognition types could be identified. At this level "beyond the molecule" [42] the spatial arrangement of the building blocks and the functionality of the supramolecular assemblies is determined by the directional intermolecular interactions. These bonds, non-covalent in nature, are of weak or intermediate strength. The various bonding types comprise metal-ligand interactions, hydrogen bonding, van der Waals interactions, electrostatic forces, etc. Each bonding type represents a different class of interactions differing in their directionality, degrees of strength, and dependence on distances and angles. In general these intermolecular forces are weaker than covalent bonds which is reflected in the thermodynamic properties of supramolecular species. The lack of stability is balanced by a high flexibility of the so-called soft bonds. Structural errors can be healed by annealing the species in order to obtain thermodynamic equilibrium structures.

Among the mentioned driving forces hydrogen bonding and metal-ligand interactions govern the molecular self-assembly of biological systems and the acceptor-donor interactions found in proteins. A few well-known examples, where hydrogen bonding plays a decisive role, are structural aspects of DNA, protein conformations and folding, and receptor functions in biological systems [41, 43]. Hydrogen bonding is thus one of the most important intermolecular interactions and therefore it has been studied extensively. Three-dimensional structures may be readily and specifically assembled by hydrogen bonding, incorporating a large degree of flexibility due to the weak intermolecular forces. As the interaction is weak, it may be reversed and therefore an intrinsic error correction mechanism is characteristic for hydrogen-bonded assemblies, which leads ultimately to the most thermodynamically favored structure. Another characteristics encountered in hydrogen bonded assemblies is the concept of cooperativity. Although each individual hydrogen bond is weak, the strength of many is sizeable enabling non-covalent synthesis based on the formation of multiple hydrogen bonds. Moreover, multiple bonds between two components often serve as a molecular recognition scheme and thus control the spatial arrangement of the components. In a vast number of supramolecular systems hydrogen bonding is indeed found to be responsible for the determination of molecular conformation, aggregation and functionality. The suitability of hydrogen bonding for the construction of highly organized assemblies at surfaces has been demonstrated in various experiments [6, 12, 44–50]. The great flexibility of this weak interaction allows to control the topology of complex surface-supported assemblies [8] and in conjunction with substrate interactions it may result in architectures at a mesoscopic scale [46].

One of the most widely used strategies for organizing molecular building blocks into supramolecular architectures is based on metal–ligand interactions [41, 42, 51, 52]. More than a century ago Alfred Werner developed the concepts of coordination chemistry [53]. Today it has evolved to a powerful tool for the predictable bonding and organization of organic ligands via secondary building blocks to engineer supramolecular coordination complexes. Extraordinary structures with unusual properties could be synthesized by this method: rotaxanes and catenanes, synthetic receptors, molecular cages, as well as multicomponent assemblies such as chains, nanoporous networks or helices to cite only a few examples [41, 54–58]. The enhanced rigidity, selectivity and directionality of this interaction makes it superior to hydrogen bonding. Thus, coordination interactions are fundamentally important in solid state chemistry for the rational crystal engineering. In particular, the independent design of molecular and metal containing secondary building blocks broadens the capability of this approach. Moreover, transition metal complexes also play a tremendous role in catalysis. The approaches of synthetic chemistry to mimic and understand the cofactors of enzymatic proteins have created a variety of metal-organic catalytic materials [59], which have been also extensively studied by theoretical means [60]. Under these considerations the exploration of transition metal coordination structures supported at surfaces is also of great interest for fundamental research and technological progress. The direct local accessability of coordination structures at surfaces by scanning probe techniques makes them to an appealing object in surface chemistry [2, 19–21, 61–64]. Molecular magnetism constitutes yet another promising facet of modern coordination chemistry. In recent years a variety of structures starting from single molecule magnets up to crystal structures of extended coordination networks have been synthesized bearing intriguing magnetic behavior [65–69]. Apart from the envisioned applications for data storage devices, these compounds are also studied for their interesting physical properties, such as spin crossover phenomena [70, 71]. However, the characterization of coordination structures at surfaces is still at the beginning, where the presence of a metal substrate rises interesting questions on the coupling between the magnetic moments.

This thesis presents the results of the investigations on supramolecular architectures self–assembled at well-defined metal surfaces. We start with the fabrication, where we employ the three above mentioned intermolecular forces, namely hydrogen bonds, metal–ligand interactions and electrostatic forces. The construction principles are deduced from scanning tunneling microscopy characterization of the realized structures. Then, we proceed to the functional aspects of surface-supported supramolecular assemblies. Both chemical and physical properties were studied by x-ray absorption as well as STM experiments.

The thesis is organized as follows:

Chapter 1 gives a brief introduction to the scanning tunneling microscopy and x-ray absorption techniques. The STM provides detailed structural information of the supramolecular assemblies, while the integral spectroscopy methods enable one to probe the chemical and magnetic state of the systems. At the end of the chapter a table containing information on the molecules used in this study is given.

The second Chapter of the thesis is concerned with supramolecular assembly via hydrogen bonding. We chose simple aromatic carboxylic acids to study the bonding motifs mediated by the carboxyl group at a Cu(100) surface. All molecular building blocks readily assemble into 1D and 2D supramolecular networks with the carboxyl and carboxylate moieties as active bonding sites. The protonation state of the acid group is subject of a combined STM and x-ray absorption experiment. The thermally activated deprotonation process of the carboxyl group is reflected in the topology alteration of the terephthalic acid (TPA) adlayers. Intermolecular interactions between the diterephthalate species mediate the evolution of two-dimensional domain structures extended over entire terraces. The comparative study of TPA and 2,5-pyrazinedicarboxylic acid (PDA) addresses the effect of a reduced number of binding sites on the dimensionality of the assemblies. An element substitution in the molecular backbone of PDA allows only the growth of one dimensional structures as the lateral binding of adjacent rows is prevented by the absence of potential hydrogen bonds. Finally, we studied the influence of the molecular backbone symmetry on the supramolecular architectures. The difference of the symmetry content in 4,4'-biphenyldicarboxylic acid (BDA) and 4',4" *trans*-ethene-1,2-diyl-bisbenzoic acid (SDA) is differently expressed in distinct supramolecular domains comprising similar H–bond configurations. The breaking of the molecular backbone symmetry is associated with a symmetry reduction of the supramolecular motifs. All H–bonded assemblies are subjected to molecule-surface interactions which is expressed in commensurable molecular arrangements with the substrate registry. Hence, the topology of the supramolecular structures is a result of the delicate balance between inter-adsorbate and adsorbate-substrate interactions and might change at different substrates.

In Chapter 3 we used metal coordination interactions to steer the molecular arrangement at a Cu(100) surface. The first part of this Chapter deals with the transition metal mediated arrangement of molecular linkers comprising carboxyl, pyridyl and hydroxyl functionalities. Subsequent deposition of iron atoms and organic ligands results in a rich variety of metal coordinated supramolecular structures. The reticular networks of the carboxylate linkers TPA, BDA and 4,1',4',1"-terphenyl-1,4"-dicarboxylic acid (TDA) are expected to possess identical topology but the interaction of the molecules with the substrate induces drastic changes in the coordination configuration of the diiron units as the number of the aromatic rings in the molecular backbone structure varies from one to three. Structural isomerism is frequently found in 3D coordination compounds and it is also present in the carboxylate networks due to the binding properties of the functional moieties. This issue is addressed in a comparative study of heterofunctional (4-[*trans*-2-(pyrid-4-yl-vinyl)]benzoic acid, PVBA) and homofunctional (BDA) linker molecules. The carboxylate group accounts for the evolution of diiron coordination centers in both networks. However, the carboxylate functionalities give rise for the occurrence of two isomeric structures in BDA networks, whereas the pyridyl group, preferentially binding to the axial side of the iron pair, allows the formation of only one structural type. The design of novel surface-supported coordination structures with specific properties requires the detailed knowledge of coupling schemes and binding configurations of various adsorbates on different substrates. In order to extend the established bonding motifs of carboxylate and pyridyl moieties at surfaces we synthesized a coordination network comprising single iron atoms coordinated by hydroxyl ligands in a trigonal planar geometry. Furthermore, we studied the influence of the substrate on the resulting distorted hexagonal network structures by using two distinct single crystal surfaces, Cu(100) and Ag(111). The hexagonal symmetry of the network is competing with the square symmetry of the Cu(100) leading to a significant distortion of the structure while on the Ag(111) facet a more relaxed honeycomb network is found. Finally, in the second part of this Chapter we introduce a novel construction principle for supramolecular assemblies at surfaces. We demonstrate the fabrication of well-ordered supramolecular arrangements via electrostatic interactions between the carboxylate groups and co–evaporated caesium ions. Due to the electrostatic nature of the interaction it is expected that the symmetry and registry of the substrate strongly affects the arrangement of the molecular linkers. This approach represents yet another powerful tool to construct 2D supramolecular assemblies supported at metal surfaces.

Chapter 4 addresses the functionalities of the transition metal coordinated networks discussed in Chapter 3. We explored the chemical functionality of the cavity structures by the adsorption of C_{60} guest molecules. The distinct type and strength of host-guest interactions is revealed in thermal desorption experiments. On the other hand, we probed the chemical reactivity of the mono- and dinuclear transition metal centers by the adsorption of oxygen molecules. In particular, we focus on the structural relaxation of the networks upon gas adsorption and chemical reaction. Finally, the magnetic properties of the coordination centers have been determined in XMCD experiments. The experimental results give valuable insights into the valence states of the iron centers in the ligand field of the surrounding oxygen atoms. Magnetic moments and their anisotropy are deduced from the data. Although theoretical modelling is a prerequisite for the conclusive interpretation of the experimental results, it is shown that the magnetic behavior is primarily determined by the symmetry and the nature of the ligand rather than by the metal surface. These experiments demonstrate that surface-supported metal coordination structures are a promising class of materials for applications in the field of heterogenous catalysis and surface magnetism.

Chapter 1

Experimental and Theoretical Foundations

This Chapter gives an introduction to the principles and theory of the experimental methods employed, namely scanning tunneling microscopy (STM) as well as the x-ray absorption spectroscopy techniques (XPS, NEXAFS, XAS, and XMCD). The experimental set-up and sample preparation used during this thesis are discussed in Section 1.2 and Section 1.3, respectively.

1.1 Experimental Methods

1.1.1 Scanning Tunneling Microscopy

Scanning tunneling microscopy, invented by Binnig and Rohrer in 1982 [72], is a technique strongly related to classical electron tunneling experiments pioneered in the early sixties by Giaever and coworkers [73]. In both cases the quantity of interest is the tunneling current I between two electrodes biased at a voltage V. The electrodes are separated by a thin insulating medium. The amount of current flowing for a given potential difference V depends on the density of electronic states (DOS) in the electrodes, and thus contains valuable information about the electronic structure of the surfaces of the electrodes. In classical tunnel junctions an oxide was mostly used as insulator, whereas a vacuum gap serves as tunnel barrier in STM. The gap can also consist of "insulating" gaseous and liquid substances, e.g. air or electrolyte. In STM one electrode is tip shaped, i.e., microscopic, and can be positioned in three dimensions relative to the second electrode, contrary to classical tunnel experiments, where two static planar electrodes were used. In Figure 1.1(a) the schematic of an STM is shown. A tip, normally

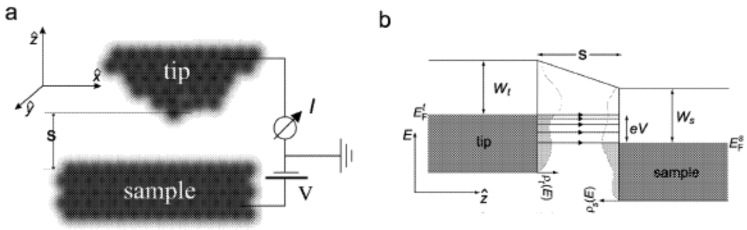

Figure 1.1: **(a)** Principle of an STM. **(b)** Corresponding potential energy diagram.

a sharpened metallic wire, is brought close to the conducting surface of a sample. In ultra–high vacuum (UHV) experiments the sample surface is atomically clean, usually by means of rare gas ion bombardment with subsequent annealing for metals, or by cleaving and subsequent annealing in the case of semiconductors. The lateral tip position (x and y axis), as well as the tip-sample distance, s, are controlled with picometer precision by means of voltage signals applied to piezo-electric materials. If the tip is brought close enough to the sample that the wave functions of the conduction electrons of tip and sample begin to overlap substantially, a measurable tunneling current I can flow between the biased sample (potential V with respect to ground) and the virtually grounded tip (Fig. 1.1(b)). The tip-sample (core-to-core) distance in typical tunneling experiments is about $5 - 10$ Å. Since the tunneling current depends exponentially on the tip-sample distance, it mainly flows through the few atoms at the very apex of the tip. Thus, the tunneling current is highly localized, leading to the atomic-scale resolution of STM. In the case of a positively biased sample (as in Fig. 1.1(b)) the net current comes from electrons tunneling from occupied states in the tip to unoccupied states of the sample. The current per energy unit, i, is represented by the density of horizontal arrows in Fig. 1.1(b). As can be seen i decreases with decreasing energy since the energetically lower lying states decay faster in the vacuum barrier region. While it is intuitively clear from Fig. 1.1(b) that the tunneling current will depend on the density of occupied and unoccupied states of tip and sample (ρ_t and ρ_s, respectively), the exact calculation of the tunneling current starting from the electronic structures of tip and sample is a difficult task. Compared to classical tunneling experiments the modeling of the tunneling current is additionally complicated in STM by the fact that the atomic structure and the chemical nature of the tip apex is normally not known.

To interpret our data we followed the widely used transfer Hamiltonian approximation introduced by Bardeen [74], where the tunneling current is given by [75]:

$$\begin{aligned} I(V) &= 2e \sum_{\mu,\nu} \frac{2\pi}{\hbar} |M_{\mu,\nu}|^2 \, \delta(E_\mu - eV - E_\nu) \times \\ & \quad (f(E_\mu - eV, T)\,[1 - f(E_\nu, T)] - f(E_\nu, T)\,[1 - f(E_\mu - eV, T)]) \ . \end{aligned} \quad (1.1)$$

Here the summation runs over all quantum states μ and ν of the unperturbed sample and tip, respectively, f is the Fermi–Dirac distribution function[1], T is the temperature and the transfer matrix $M_{\mu,\nu}$ is given by

$$M_{\mu,\nu} = -\frac{\hbar^2}{2m_e} \int_\Sigma d\mathbf{S} \, (\Psi_\nu^* \nabla \Psi_\mu - \Psi_\mu \nabla \Psi_\nu^*) \, , \quad (1.2)$$

which must be evaluated over a surface Σ within the gap region and with the wave functions of the unperturbed sample and tip, Ψ_μ and Ψ_ν, respectively. The matrix elements $M_{\mu,\nu}$ depend roughly exponentially on the barrier width s, and also on the electron momentum parallel to the surface, $p_{||}$. The larger $p_{||}$ the less energy is in the motion perpendicular to the surface, E_z, and thus the faster the vacuum tail of the wave functions decay. Therefore, electrons of total energy E with little parallel momentum tunnel with a higher probability than electrons of the same total energy E with large $p_{||}$.

To go beyond qualitative properties of the tunneling current one has to find good approximations for the matrix elements $M_{\mu,\nu}$. A common approximation in STM theory is the s-wave approximation for tip wave functions introduced by Tersoff and Hamann [76], leading to the expression for the tunneling current [77, 78]:

$$\begin{aligned} I(V, T, x, y, s) &\propto \int_{-\infty}^{\infty} dE \ \rho_s(E, x, y)\, \rho_t(E - eV) \times \\ & \quad \mathcal{T}(E, V, s)\,[f(E - eV, T) - f(E, T)] \, , \end{aligned} \quad (1.3)$$

where ρ_t is the DOS of the tip, x and y characterize the lateral position on the sample and s is the distance between tip and sample measured from a virtual plane passing through the uppermost atoms. ρ_s is the LDOS (local DOS) of the sample in this virtual plane. An often used expression for the tunneling transmission factor $\mathcal{T}(E, V, s)$ disregards the $p_{||}$ dependence of $M_{\mu,\nu}$ and reads [78]:

$$\mathcal{T}(E, V, s) = \exp\left(-2s\sqrt{\frac{m_e}{\hbar^2}}\sqrt{W_s + W_t - 2E + eV}\right) \, . \quad (1.4)$$

Here W_s and W_t are the work functions of sample and tip, respectively (cf. Figure 1.1). Although this is a crude simplification, the expressions in Eqs. (1.3) and (1.4) contain

---

[1] Energies are given with respect to the Fermi level if not otherwise is stated.

the essential physics and are a good starting point for qualitative and under certain conditions quantitative discussions. For low bias voltages $eV \ll W_s + W_t$ the bias and energy dependence of the transmission factor in Eq. (1.4) can be disregarded, leading to the following simplified expression for the current:

$$I(V,T,x,y,s) \propto e^{-2s\sqrt{\frac{2m_e}{\hbar^2}(W_s+W_t)}} \int\limits_{-\infty}^{\infty} dE\ \rho_s(E,x,y)\,\rho_t(E-eV)\,g(E,V,T)\,, \qquad (1.5)$$

where $g(E,V,T) = f(E-eV,T) - f(E,T)$. If in addition the measurements are performed at low temperatures, the integration limits in Eq. (1.5) reduce to the interval from E_F to $E_\mathrm{F} + eV$. If we assume furthermore that $\rho_s(E,x,y)$ and $\rho_t(E)$ are constant in this energy range, Eq. (1.5) simplifies to

$$I(V,x,y,s) \propto V\rho_s(E_\mathrm{F},x,y)\,\rho_t(E_\mathrm{F})\,, \qquad (1.6)$$

which is well known as the Tersoff–Hamann expression for the tunneling current. This model is only valid in the limit of low temperatures and bias voltages and for a weak coupling between the electrodes, but it shows that in first approximation constant-current STM topographs can be simply interpreted as contours of constant $\rho_s(E_\mathrm{F})$, the LDOS of the surface at the Fermi energy.

All STM images presented in this thesis are taken in the so-called *constant–current imaging* mode [79]. In constant–current imaging the tunneling current I is compared to a preset value I_0. The difference signal $\Delta I = I - I_0$ is fed back to the voltage applied to the z-piezo so that the tip-sample distance is adjusted in order to minimize ΔI [80]. The surface is then scanned by the tip and the voltage applied to the z-piezo is recorded. One thus obtains a so–called topograph $z(x,y)|_{I,V}$. This term is misleading because $z(x,y)|_{I,V}$ is rather a surface of constant local density of states (LDOS) at the Fermi energy (E_F) of the sample. Thus, it reflects the electronic structure and $z(x,y)|_{I,V}$ cannot be directly interpreted in terms of surface topography. The size, nature and chemical identity of the tip does not only influence the resolution and the shape of an STM scan but also the electronic structure to be measured.

The interplay between the topography and the electronic structure becomes crucial in interpreting STM data obtained on molecular adsorbates. A well–known counterintuitive example is atomic oxygen chemisorbed on a metal surface, which appears as a depression in STM images even if the atom is positioned above the metal surface layer (see [18] and Section 4.2). STM patterns of molecules often show internal structure and details but the interpretation is not straightforward due to the fact that protrusions on the STM image do not necessarily represent actual positions of atoms. It is rather expected that such features correspond to molecular orbitals, in particular the highest occupied (HOMO) and lowest unoccupied (LUMO) molecular orbitals.

Before the first successful STM experiments with clearly resolved organic molecules were reported [81–83] it appeared questionable whether "insulating" molecules can be imaged by STM at all. As stated above, the tunneling current is proportional to the sample LDOS near the Fermi level E_F within the framework of the s-wave theory of STM. Most organic molecules have a large energy gap between the HOMO and LUMO. If physisorbed on a metal surface, the molecule-related states are usually far away from the substrate Fermi energy. The HOMO- and LUMO-derived resonances are typically several eV below and above E_F, respectively. Therefore, the molecule's contribution to the LDOS near E_F is rather small and at a first glance one might expect organic molecules to be transparent for tunneling electrons at low bias voltage.

These findings are of general importance for the imaging of molecules adsorbed on metal surfaces. Nonresonant tunneling occurs and the contribution of the adsorbate to the current originates from tails of molecular orbital resonances crossing the Fermi level. These tails are usually rather small at the Fermi level, which explains why contributions from the substrate itself cannot be neglected, despite the rather important difference in height.

To interpret STM images of molecules the electronic structure of the adsorbate-substrate system can be calculated, whereby various levels of approximation ranging from effective Hückel to first-principles self-consistent methods (mainly based on the density functional theory (DFT)) are used. Again, the tunneling current is frequently associated with the LDOS of the sample at the Fermi energy. In this approach the tip and the surface are treated separately, which neglects any interaction between them, and is valid only in the limit of large tip-surface distances (similarly to the Tersoff–Hamann model, where the electrodes are treated separately and the result is derived for small voltages). Secondly, a severe approximation is made to the structure of the tip apex and any tip dependence of the image lost. This can be accounted for by regarding p and d states for the tip orbitals [84] or by describing the tip apex by a cluster of a small number of atoms [85, 86].

Another approach is the proper description of the interaction between sample and tip using the formalism of scattering theory. The influence of the tip-sample interactions becomes apparent in the imaging of adsorbed alkali metal atoms. Although they are known to substantially increase the LDOS at E_F, they are frequently transparent in STM data [87]. The basic idea of the scattering theory formalism is to consider the tunnel gaps as a two-dimensional defect inserted between two semi-infinite periodic systems. The tunnel event is then viewed as a scattering process. An example is the electron scattering quantum chemical approach (ESQC) developed by Sautet and Joachim [88]. The tunnel junction is modeled by the approach of substrate and tip semi-infinite bulk solids. The adsorbate is chemisorbed on the substrate surface, while the tip apex, attached to the second semiinfinite solid, is modeled by a cluster of 1–15 atoms. A coupling with the tip and substrate electron reservoirs is hence fully taken into account.

Aromatic molecules represent an important group of adsorbates, whose functionality can be exploited for building diverse molecular nanostructures at surfaces. Benzene was the first molecule of this class that was successfully imaged on a surface by high-resolution STM: coadsorbed with CO on Rh(111) [82], benzene molecules, which are bound to threefold substrate hollow sites as determinded by LEED [89], appear as three lobes arranged in a triangle in STM topographs. The lobes are located near the middle of C–C bonds, in between underlying Rh substrate atoms as evidenced by ESQC [90]: the molecule appears to have threefold symmetry because molecular orbitals are hybridized with the rhodium substrate atoms below. As a consequence the STM image of benzene does not show positions of molecular C atoms but specific C–C bonds.

High-resolution STM studies, combined with calculations of LUMO and HOMO, were performed with more complex aromatic species in the early 90's. Particularly, a comparative study of naphthalene ($C_{10}H_8$) and azulene ($C_{10}H_8$) adsorbtion on Pt(111) evidences that a simple calculation methodology based on extended Hückel molecular orbital theory adequately predicts details of internal structure [91]. Electron and hole density plots show very good agreement with the actual STM data and enable the reliable identification of molecular species.

A detailed descritpion of several theoretical approaches to the contrast mechanism of adsorbate imaging with the STM is given in a review by Sautet [92].

1.1.2 X-ray Absorption Techniques

X-ray absorption techniques are widely used to probe the occupied and unoccupied electronic states of given materials and thus the electronic structure of the compounds. The methods described in the following Sections are refered to as integral techniques, i.e., the detected signal is averaged over a relatively large area/volume of the sample and thus spatially homogenous materials are required. Furthermore these techniques are elementspecific as the x-ray absorption edges of different elements occur at specific energies.

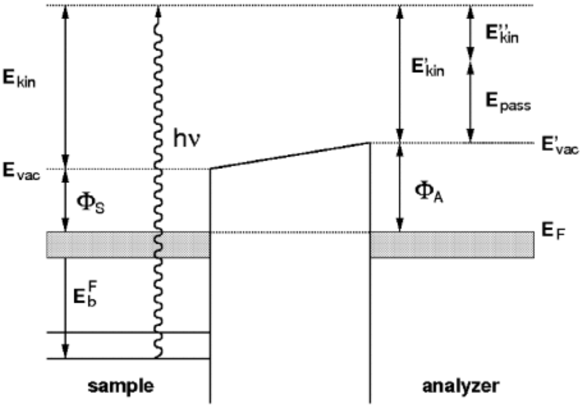

Figure 1.2: Schematic XPS energy diagram. The electrons leaving the sample with kinetic energy E_{kin} enter the analyzer with energy E'_{kin} and are detected with energy E''_{kin}. The Fermi levels of the two systems have been equalized by an electrical contact between sample and analyzer.

X-ray Photoelectron Spectroscopy (XPS)

X-ray photoelectron spectroscopy (XPS) is one of the most applied methods in surface science. It allows to determine the element composition of surfaces and the chemical nature of the elements of a large variety of materials such as metals, alloys, oxides, ceramics, organic solids, polymers and even biological samples. XPS is the energy-dispersive analysis of the emitted photoelectrons. It is based upon a single photon in/electron out process and it is therefore much simpler than the Auger process, which is also widely used for the chemical characterization of solid surfaces. Monochromatic photons with energy $h\nu$ are absorbed by atoms in a molecule or solid, leading to ionization and the emission of core (inner shell) electrons. The kinetic energy distribution of the emitted photoelectrons can be measured using an appropriate electron energy analyzer and a photoelectron spectrum can thus be recorded. Energy conservation requires that (cf. Figure 1.2):

$$E_{\text{kin}} = h\nu - E_{\text{b}} - \Phi_{\text{S}} , \tag{1.7}$$

where E_{b} and Φ_{S} denote the binding energy of the electron and the work function of the sample, respectively. The photoelectrons enter the analyzer with the kinetic energy E'_{kin} and are detected with energy E''_{kin} (cf. Fig. 1.2). The determination of the binding energy requires the values of the work functions of the analyzer Φ_A and sample Φ_S. However, it is sufficient to know the work function of the analyzer because the Fermi levels of the two systems have been equalized by an electrical contact. The spectrometer is then calibrated by measuring the binding energy of a well-known reference sample.

X-rays can easily penetrate metals several meters. XPS owes its surface sensitivity to the relatively small escape depth of the generated photoelectrons. The mean free path of the electrons depends on their kinetic energy [93]. In the energy range from 10 to 1100 eV the electrons possess a mean escape depth of approximately 1 to 3 nm. The limited escape depth of the electrons is exploited in angle-resolved XPS (AR-XPS) in order to obtain a depth profile of the chemical composition of the sample. Hence, it implies a background of inelastically scattered photoelectrons in the detected spectrum which has to be accounted for. The background correction is usually done by the method established by Shirley [94]. A typical XP spectrum shows characteristic lines for the core shells of the atoms at low kinetic photoelectron energy and structures for the valence band at high kinetic energy. There are also satellite peaks generated by plasmon excitations or shake-up processes. Furthermore, Auger peaks appear as the Auger process is a follow-up process of the photoemission. On the low energy side of the spectrum secondary electrons and inelastic scattered electrons are detected leading to the characteristic step-like shape of the spectrum.

The ratios of the peak intensities of a chemical element correspond to the stoichiometric ratios of the different chemical species in the sample since the cross section for the photoionization is virtually independent of the valence state of the atoms. In order to compare the content of different elements in the sample the experimental intensities have to be corrected by a specific photoionization cross section factor. The effect from the energy dependence of the mean free path of the photoelectrons is usually neglected, which is exact for submonolayer coverage of surfaces. One of the advantages of XPS is its sensitivity to the local charge distribution at the atomic positions, i.e., different effects contribute to the actual binding energy:

$$E_\mathrm{b}^{eff} = E_\mathrm{b} + \Delta E_\mathrm{chem} + \Delta E_\mathrm{Mad} + \Delta E_\mathrm{r}^\mathrm{int} + \Delta E_\mathrm{r}^\mathrm{ext}\,, \tag{1.8}$$

where the chemical shift ΔE_chem and the Madelung term ΔE_Mad take into account the static effects influencing the ground-state energy, whereas the ΔE_r terms describe relaxation effects due to dynamical processes related to core electrons $\Delta E_\mathrm{r}^\mathrm{int}$ and valence band electrons $\Delta E_\mathrm{r}^\mathrm{ext}$. The latter terms take account of the fact that one determines a larger binding energy for fast excitations in contrast to slow excitations, since a fast excitation does not reach the potential minimum of the whole system. Only afterwards the system relaxes into the minimum involving also geometrical changes. The effective charge (oxidation state) and the influence of adjacent atoms are described by ΔE_{chem}. This local charge distribution is often described by an effective charge (Pauling charge). On the other hand the Madelung term ΔE_{Mad} contains the contributions of all other atoms to the electric potential at the absorbing atom. Although only changes in the chemical shift of different compounds are discussed the Madelung term cannot be neglected. The chemical shifts can be completely compensated by this term. But in general the following rule is valid: The more negative the Pauling charge the lower the binding energy. This is intuitively clear as the repulsive interaction lowers the binding energy.

The chemical species are usually identified by comparing peak positions to values compiled in reference books for X-ray photoelectron spectroscopy (see, e.g., ref. [95]).

X-ray Absorption Spectroscopy (XAS) and Near-Edge X-ray Absorption Fine Structure (NEXAFS)

Opposite to the related XPS technique (see previous Section) in x-ray adsorption spectroscopy (XAS) and the more specific near-edge x-ray absorption fine structure (NEXAFS) spectroscopy the x-ray energy is scanned and the absorbed x-ray intensity is measured. The latter technique refers to the absorption fine structure close to an absorption edge, about the first 30 eV above the actual edge. This region usually shows the largest variations in the x-ray absorption coefficient and is often dominated by intense, narrow resonances. As the x-ray energy is scanned the technique requires a tunable light source which is provided by synchrotron facilities. The synchrotron radiation offers high intensities and brilliance in a wide energy range allowing an access to core electron excitations in light as well as heavy atoms. This enables absorption experiments with submonolayer sensitivity.

The fine structure arises from excitations into unoccupied molecular orbitals, thus the technique is very sensitive to the bonding environment of the absorbing atom. The comparison of measured spectra with reference lines, the so-called spectral “fingerprint” technique, is often used to identify the local bonding environment of the chemical species. The spectra exhibit chemical shifts for each chemical species similar to XPS spectra but more importantly considerable different fine structure for an element in different local bonding environments. This makes it superior to XPS, which does not provide local structural information. Another advantage of NEXAFS spectroscopy is its polarization dependence of the incident x-rays. Linear polarized light is best suited for covalent systems with directional bonds. In this case the electric field vector of the x-rays serves as a "search light" that can look for the direction of chemical bonds of the atom selected by its absorption edge. The detected signal takes a maximum if the electric field vector is aligned with the bond direction. Especially the unoccupied orbitals of σ and π symmetry of aromatic molecules, which are oriented in and out of the ring plane, can be used to obtain information on the alignment of such molecules. For flat-lying chemisorbed aromatic molecules at surfaces the π resonances can broaden significantly, because the π orbitals are involved in the bonding to the surface. For a more detailed description of this technique see, e.g., ref. [96].

NEXAFS spectra can be recorded in different ways. The most common methods are transmission and electron yield measurements. The former technique requires thin foils while the latter, often called total electron yield (TEY) detection, can be used for conventional samples. The absorbed x-ray intensity is measured by the photoelectrons that are created by the absorption process. Core electrons are excited into empty states above the Fermi level. The generated holes are then filled by Auger decay, which is dominant in the soft x-ray region over x-ray fluorescence. Thus the intensity of the emitted primary Auger electrons is a direct measure of the absorbed x-ray intensity and is used in so-called Auger electron yield measurements (AEY). As they leave the sample the primary Auger electrons create scattered secondary electrons which dominate the total yield (TEY) intensity. The sampling depth in TEY measurements is typically a few nanometers while it is often less than 1 nm for AEY measurements, similar to XPS.

Modern NEXAFS spectroscopy uses linear as well as circularly polarized light to probe the anisotropy of charge and spin. In the following Section the power of the polarization dependence in conjunction with surface magnetism will be discussed.

X-ray Magnetic Circular Dichroism (XMCD)

In rare-earth magnetic materials and transition-metal ferromagnets the strong dipole-permitted excitations (core $3d$, $4d \rightarrow$ valence $4f$ and core $2p \rightarrow$ valence $3d$, respectively) are of great interest. The transition energies lie in the soft x-ray range. X-ray absorption experiments with polarized light allow therefore to extract a great deal of information on the magnetic state of such systems. After the first practical demonstration of x-ray magnetic dichroism (XMD) using linearly polarized light in 1986 [97] XMCD, i.e., usage of circularly polarized light, has been developed both experimentally [98–105] and theoretically [106–114] into a powerful quantitative magnetometry tool. XMCD is elementspecific, has submonolayer sensitivity, and can be used to measure magnetization loops. It allows to identify the moment orientation in ultrathin magnetic films, being unique among surface sensitive magnetooptical techniques, to determine separately the spin and orbital magnetic moments of a given element together with their anisotropies.

The absorption of polarized light by a magnetized sample depends on the orientation of the magnetization **M** relative to the light polarization direction.[2] XMCD is defined as the difference in the absorption coefficients for parallel μ^+ and antiparallel μ^- orientation of the magnetization direction of the sample with respect to the helicity of the circularly polarized exciting light. For $3d$ transition metals the dipole selection rules allow the following transitions:

$$\begin{array}{lll} \mathrm{K}: & 1s & \rightarrow & 4p_{1/2} \\ \mathrm{L}_2: & 2p_{1/2} & \rightarrow & 3d_{3/2}, 4s \\ \mathrm{L}_3: & 2p_{3/2} & \rightarrow & 3d_{3/2,5/2}, 4s, \end{array}$$

where the subscript indicates the quantum number j of the total angular momentum. The properties of $3d$ electrons are probed by excitation of $2p$ core electrons to unfilled $3d$ states, thus we are interested in the intensities of the L_2 and L_3 absorption edges. The energies corresponding to the L_2 and L_3 main lines are $\mathrm{L}_2 = 721$ eV and $\mathrm{L}_3 = 707$ eV for Fe. Figure 1.3 shows the L_2 and L_3 adsorption edges of a ~ 0.025 ML thick Fe film on Cu(100). The background contributions due to $p \rightarrow s$ transitions is accounted for by the substraction of step functions; in practice the exact form of the s background is not known, even if smoothed step functions are commonly used in the literature [103]. The $p \rightarrow d$ channel, however, largely dominates the spectrum. The sum of the L_2, L_3 line intensities after the correction for the s transitions is proportional to the number of holes in the $3d$ band.

Following Stöhr [105], a qualitative understanding of the physics underlying XMCD can be given in the following way: right (R) or left (L) circularly polarized photons are absorbed which is accompanied by transfer of their angular momentum ($\Delta m = \pm 1$, respectively) to the excited photoelectron. If the photoelectron originates from a spin-orbit split level, e.g. the $p_{3/2}$ level, the angular momentum of the photon can be transferred in part to the spin through the spin-orbit coupling.[3] R polarized photons transfer the opposite momentum to the electron than L polarized photons, and hence one obtains large transition matrix elements between final states of opposite spin polarization in the two cases. In other words, for a given initial state, R and L polarized photons will excite photoelectrons having opposite spin polarization. Since the $p_{3/2}$ (L_3) and $p_{1/2}$ (L_2) levels have opposite spin-orbit coupling ($l + s$ and $l - s$, respectively), the

---

[2] The photon helicity or photon spin projection P is taken to be positive (negative) when it is parallel (antiparallel) to the light propagation direction, corresponding to R (L) polarization.

[3] The $\Delta S = 0$ selection rule of dipole transitions holds only in the $L - S$ coupling. In the $|nljm\rangle$ base that is used to represent spin-orbit split states, the single particle spin eigenvalue s_z is not a good quantum number. Its expectation value $\langle jm|s_z|jm\rangle$ yields the spin polarization of each state $|jm\rangle$.

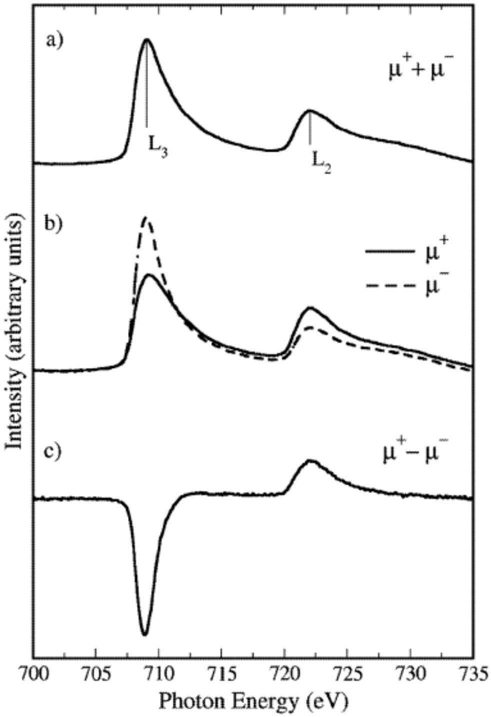

Figure 1.3: **(a)** XAS spectrum of a ~ 0.025 ML thick Fe film on Cu(100) taken at 10 K. The Fe was deposited on the substrate held at 410 K followed by an annealing for 10 min at the same temperature. **(b)** Absorption spectra for parallel (μ^+) and antiparallel (μ^-) alignment of the magnetic field H and the photon helicity P. **(c)** XMCD signal obtained by taking the difference of the two absorption spectra shown in (b).

spin polarization will be opposite at the two edges, L_3 and L_2. The magnetic properties enter in the transition of the excited photoelectron to an unfilled $3d$ state of the valence band. In the absence of a net magnetization, the number of excited electrons for a given light polarization would be the same for any of the L_3, L_2 edges because the total spin polarization for both the $p_{3/2}$ and $p_{1/2}$ manifolds is equal to zero. Suppose now that the $3d$ band is split into a spin majority and a minority band, i.e., the empty states have predominantly minority character. The final states act then as a filter for the spin of the excited photoelectron. The quantization axis of the filter is given by the magnetization direction which, for maximum dichroism effect, needs to be aligned with the photon spin direction, thereby allowing to probe its orientation. The XMCD spectrum is obtained by taking the difference $\mu^+ - \mu^-$ of the two spectra shown in Fig. 1.3(b). From the above reasoning it follows that the XMCD signal is proportional to the imbalance between the minority and majority $3d$ states above the Fermi level of the element under consideration, which in turn is proportional to the element magnetization.

Similarly, if the d valence shell possesses an orbital moment, it will act as an orbital momentum filter for the excited photoelectrons [105]. By using appropriate sum rules [108, 110, 111] it is possible to extract the orbital and spin contribution to the magnetic moment from a XMCD spectrum such as the one shown in Fig. 1.3.

Sum rules

Three important magnetooptical sum rules [108, 110–112] relate the XAS and XMCD data to the elementspecific orbital and spin magnetic moments, and to the anisotropy terms of the spin and charge densities in the unitcell. The derivation of these rules [108, 110, 111] has been carried out for electric dipole transitions in a localized model, considering a single ion in an arbitrary crystal field symmetry. Hybridization of the final states is only allowed for intrashell orbitals, i.e. there is no mixing of the d states with sp-like states. The sum rules have been tested by bandstructure calculations [115, 116] and have been verified experimentally [103].

The first rule relates the shell-specific groundstate expectation value of the orbital angular momentum operator L_P (P is the direction specified by the incident photon beam) to the integral of the XMCD absorption spectrum taken over the complete core level edge ($\mathrm{L}_3 + \mathrm{L}_2$ in our case) of a magnetically oriented ferromagnetic or ferrimagnetic material [108, 110]. In the case of L_3, L_2 transitions, one calculates the d-shell orbital momentum expectation value as

$$\frac{1}{2n_h} \langle L_P \rangle = \frac{\int_{\mathrm{L}_3+\mathrm{L}_2} dE \ (\mu^+ - \mu^-)}{\int_{\mathrm{L}_3+\mathrm{L}_2} dE \ (\mu^+ + \mu^- + \mu^0)}, \tag{1.9}$$

where n_h is the number of holes in the d shell, and the denominator term normalizes the XMCD signal to the unpolarized (isotropic) absorption spectrum (μ^0 is the absorption coefficient for linearly polarized light and is usually taken to be the average between μ^+ and μ^-).

The second rule relates the XMCD signal to the shell-specific ground-state expectation values of the total spin operator S_P and of the intra-atomic magnetic dipole operator T_P [111]:

$$\frac{2}{3n_h}\left(\langle S_P\rangle + \frac{7}{2}\langle T_P\rangle\right) = \frac{\int\limits_{\mathrm{L}_3} dE\ (\mu^+ - \mu^-) - \int\limits_{\mathrm{L}_2} dE\ (\mu^+ - \mu^-)}{\int\limits_{\mathrm{L}_3+\mathrm{L}_2} dE\ (\mu^+ + \mu^- + \mu^0)} \tag{1.10}$$

The term containing $\langle T_P\rangle$ arises from the multipole expansion of the spin density: the largest (monopole) term integrated over the atomic volume, corresponds to the isotropic magnetic spin moment; the next higher (quadrupole) term reflects the lowest order anisotropic spin distribution in the atomic cell and it gives rise to the intra atomic magnetic dipole moment $\mu_\mathrm{D} = -7\mu_\mathrm{B}\langle T_P\rangle$, where $\mu_\mathrm{B} = e\hbar/2m_e$ is the Bohr magneton [105].[4] First principle calculations [114] show that the $7\langle T_P\rangle$ term in Eq. (1.10) can be safely neglected for atoms in cubic symmetry, but that its contribution might be of the order of 10% of $\langle S_P\rangle$ for atoms at surfaces and interfaces.

In the derivation of Eqs. (1.9) and (1.10), the sample magnetization is supposed to be completely saturated, which might not always be the case in an experiment. If we, on the other hand, consider the $\langle L_P\rangle / \langle S_P\rangle$ ratio, the above contributions cancel out and the comparison between theory and experiment becomes straightforward. The orbital and spin magnetic moments are related to the expectation values of the L_z and S_z operators by $\mu_L = -\mu_\mathrm{B}\langle L_z\rangle$ and $\mu_S = -2\mu_\mathrm{B}\langle S_z\rangle$, respectively, where z is the direction of the spin quantization axis. If $\langle T_P\rangle$ can be neglected with respect to $\langle S_P\rangle$, the μ_L/μ_S ratio can be easily evaluated.

1.2 Experimental Set-up

All STM measurements presented in this thesis have been performed with the *variable temperature* UHV-STM setup, described and used in previous studies [118, 119].

The variable temperature STM [120] is operational in the temperature range 40–800 K. It is incorporated into an ultra-high vacuum (UHV) chamber (base pressure $\approx 2\times10^{-10}$ mbar), which is equipped with standard surface preparation and analysis tools (see. Fig. 1.4 for schematic drawing). Several evaporators for metals and organic

---

[4] The magnetic dipole operator is defined as $\mathbf{T} = \mathbf{S} - \hat{\boldsymbol{r}}(\hat{\boldsymbol{r}}\cdot\boldsymbol{S})$, and it represents the anisotropy of the spin distribution in the unit cell due to the crystal field and/or to the spin-orbit interaction [111]. Since the *sp* contribution to the spin density is negligible [117], the spin operator $\boldsymbol{S}$ can be expressed only by the sum of its d orbital projected components: $\boldsymbol{S} = \sum_i \boldsymbol{s}_i$. In materials with lower than cubic symmetry (typically monolayers and lowdimensional structures) the d electron density deviates strongly from spherical symmetry [105, 117]; due to the small spin-orbit coupling, the charge distribution is not significantly altered if the spin is rotated by an external magnetic field. As a consequence the anisotropy of the spin density is related to that of the charge density [105].

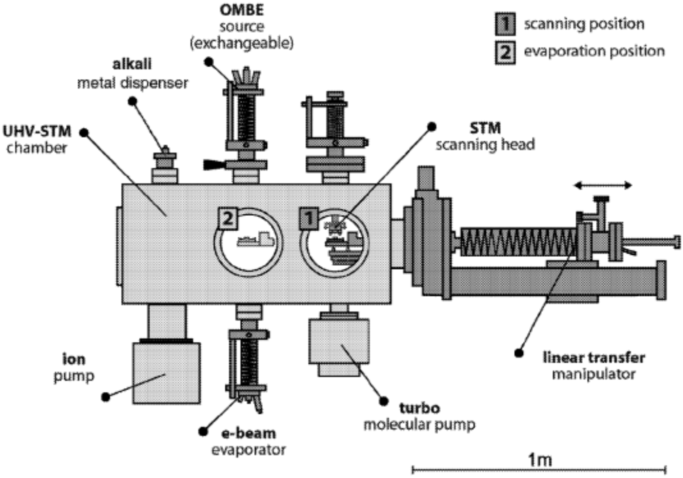

Figure 1.4: Schematic drawing of the UHV-STM system, employed in the experiments. The sample can be transferred to specific positions for STM measurements and sample preparation, where the materials are sequentially evaporated onto the substrate. Gate valves at the OMBE sources allow for the quick exchange of molecules without breaking the vacuum.

molecules can be added. The sample is tightly mounted on the sample holder, cooling is realized with a Helium flux cryostat via a copper-braid and the sample can be heated radiatively or by electron bombardment using a tungsten filament mounted below the crystal (cf. Fig. 1.5).

During STM measurements the sample holder is decoupled from the precision tube and rests on the viton-damped copper-stack (cf. Fig. 1.5) [122]; for low frequency vibration damping the whole UHV chamber is suspended by springs from the ceiling. The STM is a home-built "beetle type" STM (cf. Fig. 1.6).

For operation, the STM is simply placed on the sample holder and by applying proper voltage pulses to the outer piezo legs it walks down the ramp. Once the STM is in tunneling range, scanning is effectuated through the inner piezo. The sample remains mounted to the manipulator during all operations, which throughout guarantees full temperature control. For a more detailed description see ref. [121].

The x-ray absorption experiments have been conducted with similar UHV systems at the ID–08 beamline of the ESRF in Grenoble (XAS and XMCD) and at the HE–SGM

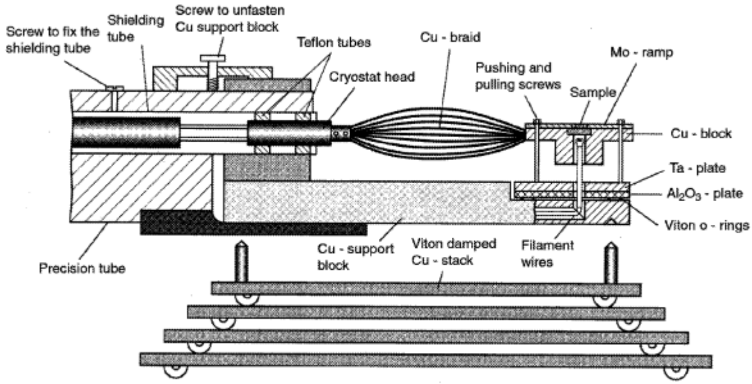

Figure 1.5: Side view of the manipulator and the sampleholder. In the STM mode the copper support block is decoupled from the precision tube and rests on the viton-damped copper-stack. (Figure taken from [121])

beamline of the Berlin synchrotron radiation facility BESSY II (XPS and NEXAFS). The very same OMBE sources as for the STM experiments were used for the sample preparation at the synchrotrons.

The UHV system at the HE–SGM beamline at BESSY II is equipped with standard facilities for sample preparation, a quadrupole mass spectrometer, as well as a twin anode X-ray source and a CLAM2 energy analyzer. All NEXAFS spectra were recorded in the total electron yield (TEY) mode using a homemade electron detector based on a double channel plate (Galileo). For the energy calibration of the NEXAFS spectra, the photocurrent of a carbon-contaminated gold grid with a characteristic peak at 285 eV was recorded simultaneously with each spectrum. This grid was also used as a radiation flux monitor. For the NEXAFS experiments, the resolution was set to $\Delta E = 0.4$ eV at 300 eV. The C 1s NEXAFS raw data were normalized by a procedure consisting of several steps. First, the spectrum recorded for the clean substrate was multiplied with a correction factor to yield equal intensities in the energy range 272-278 eV and then subtracted. The resulting data were then normalized to the photon flux by division through a spectrum obtained for a freshly sputtered gold wafer. Finally, the spectra were normalized to yield an edge jump (difference intensity between 275 and 325 eV) of one. The XP data for the carbon 1s and oxygen 1s peak were acquired with a beam energy of 400 and 650 eV, respectively. The pass energy of the analyzer was set to

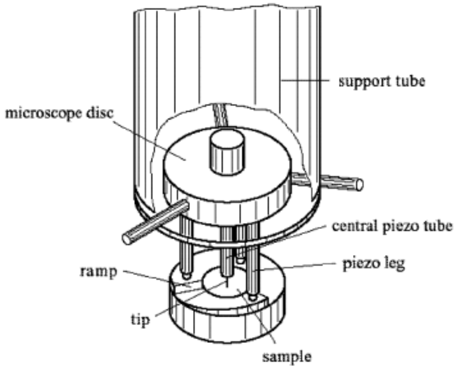

Figure 1.6: Principle of the "beetle type" STM. The body of he STM, consisting of a microscope disc and three piezo legs, is placed onto a circular ramp. For the coarse approach between the tip and the sample the STM "beetle" - driven by a electrical signal provoking a "stick and slip" movement - walks down the circular ramp on the piezo legs. Once the STM is in the tunneling range scanning is effectuated through the central piezo, which is a single tube scanner. The STM "beetle" is lifted from the sample with the help of a support tube. (Figure taken from [118])

50 eV. For quantitative analysis, a complete set of XP spectra was acquired in addition with the Al K_α-radiation of the laboratory source with a pass energy set to 100 eV. All spectra have been referenced to the Cu $3p_{3/2}$ line at 75.1 eV.

The XAS and XMCD measurements at the ESRF have been conducted with a similar UHV system. It consists of three different stages: the preparation chamber, STM chamber and the measurement chamber. The former has been only used for sample transfer from the STM chamber to the cryomagnet. The samples were prepared and checked in the STM chamber. It is equipped with standard tools for sample cleaning and material deposition. Furthermore a combined LEED/AES analysis tool and a room-temperature STM (purchased from Omicron GmbH) are installed and used to monitor the proper sample preparation. The XMCD experiments were done in the measurement chamber equipped with a variable ±6 Tesla cryomagnet operable in the range $\approx 5-300$ K with the magnetic field being collinear with the incident photon beam from the electron storage ring. The base pressure in the three stages were of the order 10^{-10} mbar.

By rotating the sample spectra for magnetic fields being either normal or parallel

(70°) oriented to the surface can be recorded. The XAS spectra were taken in the total electron yield (TEY) mode by measuring the drain current of the photoexposed sample. All spectra have been normalized by the photocurrent emitted by a gold mesh positioned before the sample which serves as a measure of the incident photon flux. The XMCD signal was obtained by substraction of consecutive XAS spectra taken with reversed helicity-magnetic field orientation.

More information on the technical specifications of the beamlines are available on the internet [123, 124].

1.3 Sample Preparation

Crystal Preparation

All VT-STM experiments described in the present thesis have been performed on the single crystal Cu(100) surface. The crystal is hat shaped with a circular surface of 7 mm in diameter and a total thickness of 3 mm (supplier: MaTeck GmbH, orientational misfit $< 0.1°$). The sample was cleaned under UHV conditions by sequential cycles of Ar^+ sputtering at 300 K and subsequent annealing to 800 K providing smooth surface with low amount of impurities. We typically used a 0.4 μA ion beam (as detected on the sample) of 500 eV energy and an incidence angle of 45° for sputtering. One sputter cycle typically lasted 15 min and the pressure while annealing was always below 4×10^{-9} mbar.

This procedure resulted in atomically clean and flat surfaces with regions showing terraces of around 100 nm width. For the prepared surface we observed a coverage of less than ≈ 0.05 % of a monolayer (ML) impurities.

A similar preparation procedure was used for the UHV facilities at the synchrotrons BESSY II and ESRF at Berlin and Grenoble, respectively.

Electron-Beam Heating Evaporation of Metals

Iron atoms were deposited on the sample *in situ* using an e-beam heating evaporator (EFM-3, Omicron GmbH). Coverage calibration was performed by area estimation using STM in submonolayer regime. One monolayer of Fe correspond to one Fe atom per a_0^2 ($a_0 = 2.55$ Å is the nearest-neighbor spacing of copper atoms of the Cu(100) surface). Depending on the needs of a particular experiment, Fe atoms were deposited on substrates, kept at low (100 K), room or elevated (up to 500 K) temperatures. The Fe flux was typically in the range of $\approx 1 - 3$ % ML/min.

The Fe flux for the experiments performed at the ESRF synchrotron was calibrated by a quarz microbalance and furthermore estimated by the normalized edge jump height of the Fe L_3 x-ray absorption peak.

Alkali Metal Dispenser

Cs atoms for the experiments described in Section 3.4 were deposited using an alkali metal dispenser purchased from SAES Getters SpA [125]. A metal stripe contains the caesium chromate salt and reducing agent mixture. The generation of the caesium vapour escaping through the slit of the dispenser starts at a temperature of about 600°C. The release of caesium depends on time and temperature. While the latter is controlled by the amount of current passed through the dispenser, the former is adjusted by a moveable shutter plate positioned between the sample and dispenser. The practical range of currents is around 4.0 to 7.5 A.

In order to ensure the proper thermalization of the dispenser during warming we followed a similar heating schedule reported in ref. [126]. After a careful degassing procedure we obtained highly reproducible flux rates at a fixed current. One dispenser contains a few mg of material and can be used at least 50 times for submonolayer despositions.

Organic Molecular Beam Epitaxy

The organic layers have been prepared *in situ* under UHV conditions. Due to the molecules' high stability and moderate vapour pressure, a molecular beam can be generated by thermal evaporation under UHV conditions [127, 128]. All molecules indicated in Table 1.1 have been deposited by a resistively heated crucible at background pressures of at most $\approx 1 \times 10^{-8}$ mbar and below. In Table 1.1 the temperatures of the crucible employed for the different materials are given. The corresponding flux ranges in between several percent of a ML/min up to one ML/min. One monolayer of molecules is defined as the surface is fully covered by the flat lying molecule species. This corresponds usually to the density of molecules in their compact island phase at the surface.

Using quadrupole mass spectroscopy analysis during evaporation tests characteristic peaks could be identified for the different molecular species. For molecules lighter than the detectable limit of 200 amu the non-destructive sublimation could be checked.

Material	Chemical name	Structure	T_{sub}	Supplier (purity)
TPA	1,4-benzenedicarboxylic acid	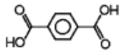	440 K	Fluka (99%)
TMA	1,3,5-benzenetricarboxylic acid	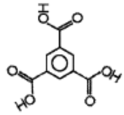	465 K	Aldrich (99%+)
TMLA	1,3,4-benzenetricarboxylic acid	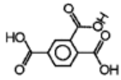	415 K	Aldrich (99%+)
BDA	4,4'-biphenyldicarboxylic acid	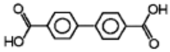	490 K	Aldrich (97%)
TDA	4,1',4',1"-terphenyl-1,4"-dicarboxylic acid	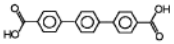	530 K	synthesized[a]
SDA	4',4" *trans*-ethene-1,2-diyl-bisbenzoic acid	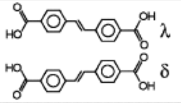	500 K	synthesized[b]
PVBA	4-[*trans*-2-(pyrid-4-yl-vinyl)]benzoic acid	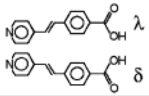	445 K	synthesized[a]
PDA	2,5-pyrazinedicarboxylic acid	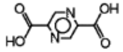	408 K	synthesized[b]
DHBP	1,4'dihydroxybiphenyl	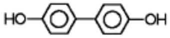	415 K	Fluka (98%+)

Table 1.1: Materials and their sublimation temperatures employed in this thesis. The specially synthesized materials were provided by the groups of [a]C. Cai (Department of Chemistry and Center for Materials Chemistry, University of Houston, Houston, Texas 77204-5003, USA) and [b]M. Ruben (Institut für Nanotechnologie, Forschungszentrum Karlsruhe GmbH, PF3640, D-76021 Karlsruhe, Germany).

Remarks on the Modelling of Structures

The molecular geometries of the species in Table 1.1 we used in modelling were calculated for isolated molecules in the PM3 approximation [129, 130]. In the models we assume an unrelaxed molecular geometry. Recent DFT calculations show that the C–C bond relaxation of chemisorbed benzene on a Cu(100) surface results in an increased bond length of less than 2% and can be neglected for the rough determination of intermolecular distances [131]. Furthermore, we also neglect the local relaxation of the Cu substrate.

Chapter 2

Bonding and Ordering of Aromatic Carboxylic Acids on Cu(100)

Hydrogen bonding is ubiquitous in the *aufbau* of biological systems and complex supramolecular structures [42, 43, 132, 133]. Distinct three-dimensional architectures can be obtained using appropriately programmed molecular species, often designated as tectons. As the interaction is weak, it may be reversed. Accordingly, intrinsic error correction mechanisms are frequently operative in the self-assembly of hydrogen-bonded systems, leading ultimately to highly organized stable arrangements. In recent years, supramolecular engineering via hydrogen bonding at surfaces has attracted considerable interest and represents a promising route toward novel construction principles of materials with nanoscale control [4, 6, 8, 12, 15, 44, 46, 134–137].

The careful choice of functional species providing geometrical (steric) and chemical complementarity allows for the tuning of two-dimensional molecular self-assembly [6, 8, 136]. On the other hand, substrate chemical activity and symmetry may strongly influence low-dimensional nanostructuring [6, 15, 138]. To guide the assembly of molecular architectures at surfaces, it is thus of great interest to elucidate the response of specific molecular moieties upon adsorption and their role in the evolution of supramolecular organizations [135, 136].

Benzoic acids proved to be versatile tectons for supramolecular engineering. A common motif in their organization is hydrogen bonding of the self-complementary carboxyl groups [136, 139–142]. In this Chapter we study the organization of simple aromatic carboxylic acids at a Cu(100) surface. In the following Sections 2.1 and 2.2 we investigate the self-assembled structures arising from the presence of a certain bonding motif and chemical activity of the substrate. The influence of the backbone molecular symmetry on the assemblies is addressed in Section 2.3.

2.1 Deprotonation-Driven Phase Transformation in TPA Self-Assembly

With the positioning of aromatic carboxyalic acids at copper surfaces, it turned out in the study of related systems that both flat-lying and upright-standing adsorption geometries can occur depending on the particular molecule used, substrate symmetry and temperature, and molecular coverage [136, 143]. The observed bonding configurations reflect (partial) deprotonation of the carboxyl groups, different carboxylate coupling schemes to the substrate, and molecular interweaving hydrogen bonding.

Here, we report the results of combined X-ray photoelectron spectroscopy (XPS), near-edge X-ray absorption fine structure (NEXAFS), and scanning tunneling microscopy (STM) studies addressing the bonding and organization of terephthalic acid (TPA, 1,4-benzenedicarboxylic acid C6H4(COOH)2, cf. Table 1.1) adsorbed on a Cu(100) surface at different temperatures. We find that the carboxyl groups of the TPA molecules are (partially) deprotonated for temperatures exceeding 275 K. Three distinct phases are identified by STM in the temperature range 190-400 K. Their irreversible transformations with increasing temperature are associated with the deprotonation of carboxyl groups driving changes of intermolecular hydrogen bond configurations. XPS and NEXAFS measurements reveal the chemical nature of the molecules. The NEXAFS data show furthermore unambiguously that both the integral molecule and the terephthalate species adsorb in a flat-lying geometry.

Temperature-dependent XPS measurements were carried out to characterize and identify the chemical states of carbon and oxygen. In Figure 2.1, the XP data for a TPA adlayer on the Cu(100) surface is presented. The upper curves show the XP spectra of TPA deposited and measured on a substrate held at 190 K, whereas the graphs below show the spectra measured at room temperature after the same sample was annealed at 400 K for 30 min. For deconvolution and determination of the exact peak positions, the data were fitted after background subtraction by one to six Voigt-type curves for the oxygen and carbon 1s peaks, respectively, with an asymmetry parameter very close to 1. Within a given spectrum, the full width at half-maximum (fwhm) parameter was fixed for the fit curves. For TPA deposited at low temperature in the O 1s region, a broad peak exists at 533.1 eV (Figure 2.1, upper-right), which can be decomposed into two almost equal-height contributions with peak positions at 532.3 and 533.8 eV. In accordance with earlier observations, [139, 144–148] these two peaks are assigned to oxygen in the carbonyl and hydroxyl group, respectively. Upon annealing, a marked sharpening of the O 1s peak occurs, which is now centered at 531.4 eV (Figure 2.1, bottom-right). The

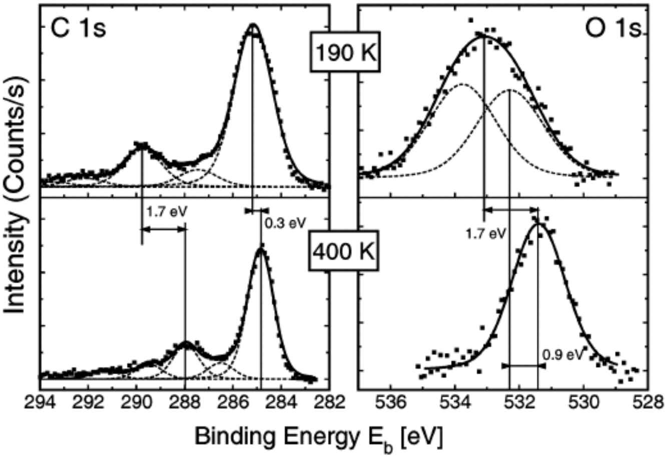

Figure 2.1: XP spectra of the C 1s and O 1s for a TPA layer prepared at 190 K (upper graphs) and following annealing at 400 K for 30 min (measured at room temperature, lower graphs). The data (squares) have been fitted by a set of one to six Voigt-type curves. The fwhm parameters for the Voigt-curves in the O 1s region are 2.47 and 1.98 eV for the substrate at low and room temperature, respectively. Peak positions are marked by vertical lines. The deconvolution of the broad low-temperature oxygen peak reflects the two chemically different carboxyl oxygen, while the sharpened peak appearing upon annealing is associated with equivalent oxygen in the diterephthalate species. The larger low-energy peaks in C 1s are from aromatic carbon and the smaller high-energy peaks are attributed to carbon of carboxyl and carboxylate side groups, respectively.

single symmetric and narrow peak is associated with two chemically identical oxygen atoms in the carboxylate moieties, clearly distinguishable from the broader peak in the low-temperature spectrum. The binding energy of the oxygen 1s electron in the carboxylate moieties is by 0.9 eV lower than in the carbonyl group [148].

Two well-separated peaks can be identified in the C 1s region for the low-temperature phase, at 285.2 and 289.7 eV (Figure 2.1, upper-left). The large peak at low energy is assigned to the six carbon atoms in the aromatic ring and the high-energy peak to the two carbon atoms in the carboxyl groups [145, 147]. The origin of the intensity around 287 eV is not known. It is not found in the multilayer C 1s core level spectrum of TPA (not shown here). Possible explanations are final state effects or a partial decomposition of the TPA molecules at defects on the copper surface. The small peak at about 292 eV is attributed to a $\pi - \pi^*$ shake-up transition of the aromatic system. Upon annealing, the position of the main carbon peak remains almost constant at 284.9 eV, whereas the smaller high-energy signal vanishes and instead a peak shifted to a lower binding energy at 288 eV emerges, which is attributed to carbon in carboxylate groups [145, 148]. The ratio of the total intensity of the oxygen 1s and carbon 1s spectra does not change upon annealing, which signifies that apart from the carboxyl deprotonation the TPA molecules remain intact (the overall intensity reduction is attributed to thermal desorption of a fractional second molecular layer existing at low temperature).

The XPS data of both oxygen and carbon strongly suggest the following scenario: at 190 K TPA molecules exist as integral species on the substrate, whereas upon the annealing carboxyl groups are fully deprotonated and the diterephthalate is formed. Deprotonation of carboxyl groups upon adsorption at Cu surfaces was similarly reported for other benzoic acid species [135,136,139,143,149]. There is general agreement that the hydrogen formed in this process is thermally desorbed. We will demonstrate below that the deprotonation plays a decisive role in the two-dimensional molecular self-assembly.

NEXAFS spectra recorded for the different TPA adlayers are displayed in Figure 2.2. Following deposition of TPA at 190 K, several pronounced π^*-resonances are clearly discernible. The π^*-resonance at 284.6 eV and the shoulder at 285.3 eV are assigned to transitions related to the carbon atoms of the aromatic ring, whereas the prominent peak at 288.1 eV, the shoulder at 288.8 eV, and the small resonance at 289.9 eV are assigned to transitions related to the carboxyl carbons. The remaining transitions at 292.8 eV, 296.4 eV, and the broad hump at 301 eV reflect σ^*-transitions. Both the π^*-resonances of the phenyl carbons and of the carboxyl carbons show a pronounced dichroism with almost completely vanishing intensity for normal photon incidence (90°). For perfectly flat-lying molecules, the intensity of the π^*-resonances should vanish completely at normal photon incidence. The small intensity remaining at 90° in the experimental spectra can be interpreted in terms of a uniform tilt of the plane of all molecules about 5° relative to the surface. However, it is more likely that the vast majority of the molecules is indeed adsorbed in a perfectly flat geometry and merely a small number of molecules deviates significantly from a flat adsorption geometry. These latter molecules can be adsorbed at defects or step edges or even in a second layer. This can occur especially at 190 K where molecular mobility is low and second layer thermal desorption does not occur.

Upon warming to 400 K and measuring the sample again at 300 K, the dichroism of the π^*-resonances is even more pronounced (cf. Figure 2.2, upper graph). This indicates that the molecules remain in a flat-lying geometry on the Cu(100) surface. In

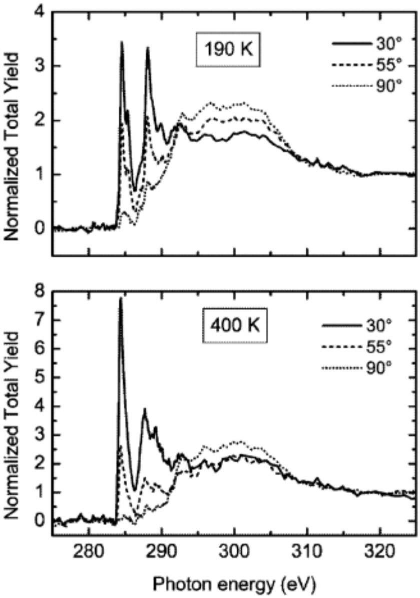

Figure 2.2: NEXAFS spectra recorded at the C *K*-edge for a TPA monolayer prepared at 190 K (lower graph) and after annealing at 400 K for 30 min (measured at room temperature, upper graph). Solid and dashed lines indicate spectra obtained at different angles of incidence of the synchrotron light (90° means normal incidence to the Cu(100) surface).

the benzene ring region, the first π^*-resonance at 284.6 eV has increased in intensity and the second resonance at 285.3 eV is not resolved anymore, whereas in the carboxyl carbon region now two π^*-resonances at 287.8 and 289.2 eV of almost equal intensity prevail. The latter two resonances seem to be shifted to lower energy upon warming to 400 K, which is in good agreement with the shift of the carboxyl peak in the C 1s core level data. The marked change in the carboxyl carbon region in the NEXAFS spectrum thus supports the XPS data, notably confirming complete deprotonation of the carboxyl groups upon annealing.

In the STM measurements three distinct topologies were observed when TPA molecules were adsorbed at substrate temperatures in the 230-400 K range. In Figure 2.3(a-c), we show representative STM images of the three phases. Besides step decoration, the molecules form ordered structures on the terraces. All phase transformations are irreversible when the sample is cooled to low temperatures.

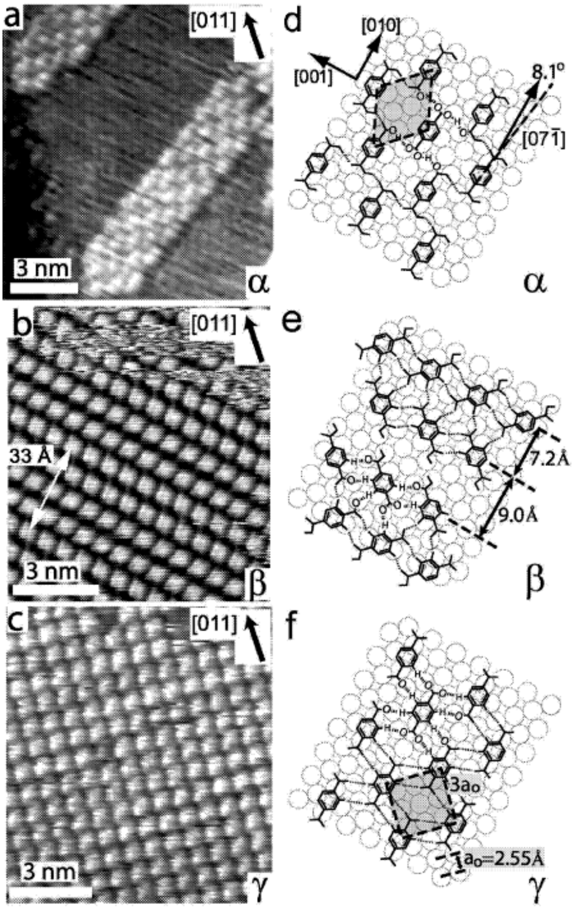

Figure 2.3: (a-c) STM images of the three molecular phases of TPA observed at different temperatures. Arrows indicate the [011] direction of the Cu(100) surface. (a) One of the four domains of the α-phase imaged at 230 K. (b) β-phase imaged at room temperature. (c) γ-phase obtained by 400 K annealing imaged at room temperature. **(d-f)** Tentative models for the three phases shown in (a-c). Hydrogen bonds are represented by dashed lines. Bonding motifs are highlighted by oxygen and hydrogen atoms marked as "O" and "H" for one molecule in each model. Aromatic ring hydrogen not involved in hydrogen-bond formation is omitted for clarity. The unit cells of the three phases are found to be [3, 0 / 1, 3], [2, -2 / 8, 10], and (3×3), highlighted for the α- and γ-phase. Open circles represent copper surface atoms. The high-symmetry [001] and [010] directions of the substrate are indicated.

An ordered low-temperature phase (cf. Figure 2.3(a)), henceforth denoted as α-phase, was observed upon TPA deposition at 230 K. The existence of molecular ribbons implies that there is appreciable mobility and anisotropic interactions under these conditions. The molecules are free to transport on the surface until they are incorporated into the ribbons, whose formation also implies edge mobility; otherwise, irregular or fractal islands in a diffusion-limited process would be expected [6, 15, 150]. Defining the orientation of a ribbon as its principal axis, four different orientated principal axes are identified. Considering the fourfold symmetry of the substrate, there are two distinguishable island directions forming an angle of about ± 8 degrees with the substrate high-symmetry directions [010] or [001]. Each island consists of several (at least two) rows of molecules running in the principal direction. Size and shape of the molecular features in the STM images agree well with the size of the TPA backbone, which is $\sim$7 Å length (cf. Table 1.1). This confirms the flat-lying adsorption geometry concluded from the NEXAFS data. Within a row, the distance between the adjacent molecules is about 12.8 Å, whereas adjacent rows have a spacing of about 4.1 Å. The long axis of the molecular features in the STM images is parallel to the principal direction of the islands.

At a temperature of $\sim$275 K, a first structural transformation occurs. The α-phase is replaced by close-packed molecular domains. This new molecular phase (denoted as β-phase) is depicted in Figure 2.3(b). The β-phase can either be obtained upon annealing the α-phase or - as for the experiment of Figure 2.3b - directly by molecular deposition on the substrate held at 275- 300 K. A detailed inspection reveals that the β-phase domains consist of paired molecular rows following either [010] or [001] direction of the substrate. TPA molecules now exhibit a rhomb shape with the diagonal aligning along [011] or $[01\bar{1}]$. Shape and size of the two differently oriented molecules are identical. The periodicity along the molecular rows amounts to about 7 Å. Molecules within a paired row are oriented in a complementary way. The row-to-row distance between TPA within a paired row is about 7 Å, whereas the interpair distance is about 9 Å. This is reflected in the more pronounced dark stripes between the paired rows. The alternative arrangement of the paired rows produces a wavelike structure with a periodicity of about 33 Å perpendicular to the row directions.

The β-phase is further transformed into a third layer structure, the γ-phase, upon 400 K annealing. It is depicted in Figure 2.3(c) and can be obtained similarly with the β-phase either via sample annealing or directly by molecular deposition with the substrate at 400 K. It is stable up to a temperature of 500 K. The molecules in this phase can form large regular domains extended over entire terraces with an almost perfect long-range ordering. The structure is built up from a square-shaped unit cell with a dimension of 7.6 Å, which matches three times the surface lattice constant (2.55 Å). The long axis of the oval molecular features in the STM image (Figure 2.3(c)) is aligned either in the [010] or [001] direction, reflecting the existence of two rotational domains.

Taking into account the XPS data, the structural transitions observed by STM are ascribed to the deprotonation of the carboxyl groups of the TPA molecules. Respective tentative models are shown in Figure 2.3(d-f). The molecular geometry of TPA used in the modeling is taken from diffraction studies of organic crystals [142]. In the models, the molecules are adsorbed flat, with their aromatic rings parallel to the surface, in accordance with the NEXAFS data. From the absence of long-range height modulations in the STM topography, we conclude distinct molecular adsorption sites for all phases. For the modeling, the aromatic ring is positioned at the fourfold hollow site, since this site has often been observed for other aromatic molecules on metal surfaces [91,151,152]. Hydrogen bonds stabilize all three phases; the respective bond lengths at surfaces can relax from the ideal hydrogen bond lengths observed in three-dimensional arrangements because of the influence of substrate atomic lattice and metal surface electrons.

For the α-phase, the data analysis suggests that TPA molecular rows are coupled by hydrogen bonds between the oxygen of the carbonyl groups and the hydrogen of the hydroxyl group in the *cis* position in contrast to the well-known 1-D carboxyl chain motif in bulk TPA [142] (cf. the model shown in Figure 2.3(d)). Each TPA is engaged in four hydrogen bonds with its neighbors, that is, the number of bonds per molecule is two. The $\mathrm{O}\cdots\mathrm{H{-}O}$ distance in the hydrogen bonds is estimated to be 3.0 Å, larger than the bulk TPA distance of 2.69 Å reported in ref. [142]. The molecules are aligned along $[07\bar{1}]$ or equivalent directions, forming an angle of 8.1° with respect to substrate high-symmetry direction, as indicated in Figure 2.3(d). This alignment is defined by two factors: the positioning of the aromatic ring and an appropriate intermolecular distance for hydrogen-bond formation. The molecular rows similarly follow the $[07\bar{1}]$ direction, agreeing well with the observed angle between the two observed reflection domains. The unit cell of this phase can be assigned as $\left(\begin{smallmatrix}3&0\\1&3\end{smallmatrix}\right)$ with respect to the (100) substrate. Because of the fourfold symmetry of the substrate, the model explains naturally the occurrence of four domain orientations. Since the packing of the ribbons accounts for an enantiomorphic structure, two domains are mirror-symmetric configurations, respectively (cf. detailed discussion in ref. [6]).

The model of the β-phase is depicted in Figure 2.3(e). It consists of paired molecular rows running along the [001] direction. The molecular axis - as inferred from the rhombohedral shape - either aligns with the [011] or the $[01\bar{1}]$ direction. We propose that each TPA molecule has at least one deprotonated carboxyl group; whether the second one is deprotonated or not is not obvious from our data (cf. detailed discussion below). The pairing suggests two types of hydrogen bonds, both involving carboxylate coupling to aromatic ring hydrogen. The respective O$\cdots$H$-$C distance is 3.0 (3.1) Å for the intrarow (inter-row) case, slightly shorter than a value found for a similar motif in a 3-D structure (> 3.3 Å) [153]. Each TPA forms six hydrogen bonds with its neighbors; the number of bonds per molecule is thus three. The inter-row distance is 7.2 Å within and 9.0 Å between the paired rows, consistent with the measured values (as shown in Figure 2.3(e)). We suggest that the inter-row hydrogen bonds are only present within paired rows but not between them (cf. detailed discussion below). The unit cell of this structure is $\left(\begin{smallmatrix} 2 & -2 \\ 8 & 10 \end{smallmatrix}\right)$.

The model of the γ-phase is depicted in Figure 2.3(f). In this case, both carboxyl groups of TPA molecule are deprotonated (cf. XPS analysis). TPA molecules arrange in a (3×3) unit cell with respect to the substrate (hightlighted by the gray square in Figure 2.3(f)), with the molecular long axis aligned in the [010] direction. Similar to the case in the β-phase, the arrangement of the molecules suggests hydrogen bonds between carboxylate oxygen and aromatic ring hydrogen, with an O$\cdots$H$-$C length of 3.4 Å, which is comparable to similar bonds in the solid state, while remaining at the lower limit [153]. Every molecule is now engaged in eight hydrogen bonds of the same type to its neighbors. Thus, the number of bonds per molecules has further increased to four.

Upon deposition of TPA molecules on the substrate held at room temperature, we observed the coexistence of β and γ-phases. To directly investigate the temporal evolution of the molecular structures, a series of consecutive STM images were taken at the same area on the surface. The data, shown in Figure 2.4, were acquired at 4-min intervals (Figure 2.4(a-c)) with the exception of the last one (Figure 2.4(d)), taken 1 hour after the first image (Figure 2.4(a)). An arrow marks a vacancy representing a reference feature. At first glance, it is conspicuous that the molecules in the β-phase are brighter than the features in the γ-phase, which is believed to correspond to a higher conductivity of the β-phase molecules. In this series of images, the area of the γ-phase grows with time at the expense of the β-phase, as seen, for example, in Figure 2.4(a-c) at the left part of the γ-phase. We have never observed the reverse process. In this particular example (Figure 2.4(a-d)), the influence of the tip seems irrelevant since Image 2.4(d) was taken 45 min later without any scanning after Image 2.4(c). However, the tip influence cannot be excluded in general: we always observed pure β-phase even 4 hours after the initial molecular deposition, but after a first scan in such a region parts of the island turned into the γ-phase. Nevertheless, after an annealing at 400 K for 5 min, the β-phase totally disappeared and only the γ-phase was observed.

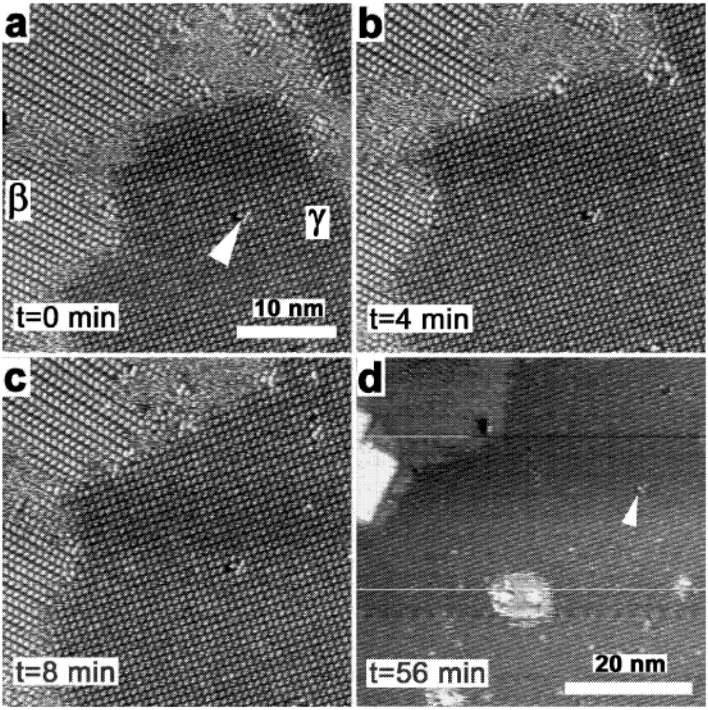

Figure 2.4: (a-d) Series of consecutive STM images recorded at the same surface area at room temperature following TPA deposition at 300 K. The images were acquired at 4-min intervals (a-c) and (d) 1 hour after (a). An arrow marks a defect representing a reference position. The area covered by the γ-phase grows with time at the expense of the β-phase.

Experimentally, it is nontrivial to correlate the β-phase to the XPS data because of its metastable nature; thus, we cannot determine conclusively the deprotonation state of the β-phase carboxyl groups unambiguously. Nevertheless, the observed room-temperature transition from β- to γ-phase is interpreted as follows: Presumably in the β-phase, TPA is only partially (i.e., one carboxyl group) deprotonated, and between TPA molecules in neighboring paired rows hydrogen bonds are prevented. Under the 400 K annealing or tip influence, the second carboxyl groups are deprotonated and tansformation to γ-phase may occur. The second possibility is that both carboxyl groups of the molecules are already deprotonated in the β-phase but the gap between the paired rows is too wide for hydrogen bond formation. In the 275-300 K temperature range, this phase is thermally metastable and an external disturbance (thermal energy or tip-induced influence) may trigger the transition to the energetically favored γ-phase.

Benzoic acid adsorption on copper surfaces was similarly studied for related systems [5, 135, 136, 138, 139, 143, 149, 154]. Quite generally, the carboxyl groups deprotonate (partially) upon adsorption and exceeding system-specific threshold temperatures, and highly ordered phases evolve. For example, on Cu(100) benzoic acid deprotonates between 120 and 170 K [139] whereas the deprotonation of trimesic acid sets in at about 290 K [136]. Interestingly, a molecular reorientation has been encountered with several of these systems. Evidence exists that in the structural transition of TMA layers on Cu(100) partially deprotonated molecules change to an upright-standing adsorption geometry to switch back to flat adsorption upon when the tri-trimesate species is formed [136, 149]. By contrast, for trimellitic acid deposition on the Cu(100) substrate held at 400 K, a highly ordered phase evolves with just one deprotonated carboxyl group, where the aromatic ring is strongly tilted away from the surface plane [5]. In addition, a coverage-dependent phase transformation was reported for benzoic acid and TPA on Cu(110), where the orientation changes from flat-lying to upright with carboxylate anchoring at surface atoms at high coverage [139, 143]. Moreover, in a series of experiments, the formation of 2D Cu-carboxylate coordination compounds incorporating copper adatoms and flat-lying molecules interferes [139, 149, 154]. At the present stage, no general rules can be derived describing the evolution of benzoic acid arrangements on Cu surfaces. While (sequential) carboxylate formation is a common feature, the delicate balance of intermolecular H-bonding, carboxylate formation with surface or adatoms, and steric matching decides on the specific structure formed.

The bonding and self-assembly of TPA on a Cu(100) surface has been studied by STM, XPS, and NEXAFS in the temperature range 190-400 K. The molecules organize in highly ordered domains comprising well-defined structural motifs. We identified three phases with distinct topologies. Deprotonation of the carboxyl moieties of the molecule underlies the respective irreversible phase transformations occurring with increasing temperature. The supramolecular ordering is rationalized by the interplay between molecule-substrate interaction and intermolecular hydrogen bonding. With the present system, the structural changes with increasing temperature reflect carboxylate formation with TPA retaining a flat bonding geometry, which drives changing 2D hydrogen bond configurations.

2.2 Dimensionality of Molecular Assemblies - TPA vs. PDA

Here we report on the two- and one-dimensional hydrogen bonded assemblies of 1,4-benzenedicarboxylic acid (TPA) and 2,5-pyrazinedicarboxylic acid (PDA) (see Table 1.1). The two linear dicarboxylic acids differ in their backbone structure, i.e., in PDA the C atoms in the 2,5 phenyl ring positions of the TPA molecule are substituted by N atoms. Note that due to the broken mirror symmetry of the PDA molecule it exists as two chiral species upon flat-lying adsorption on the surface. Both molecules easily deprotonate on the copper surface above 300 K, as shown for TPA in the previous Section 2.1. The carboxylate moieties give then rise to hydrogen bond formation to the aromatic ring hydrogen. The substitution in the molecular backbone of PDA reduces the number of potential hydrogen bonds to be formed. It is expected that this lack of binding sites is expressed in the topology of the supramolecular assemblies. Both molecules were deposited on a clean Cu(100) substrate held at room temperature. The substrate was subsequently annealed at temperatures above 360 K to facilitate the growth of the structures.

The diterephthalate molecules form long range ordered two-dimensional domains as described in the previous Section 2.1. A model of the diterephthalate molecular phase is presented in Figure 2.3(f). The arrangement of the molecules allows for two symmetric $O\cdots H\text{–}C$ bonds between adjacent molecules (cf. Figure 2.3(f)). This self-complementary bonding motif is repeated in two directions resulting in the extended two-dimensional domains. Another bonding motif could be the following: the carboxylate group of one molecule points to the side of another 90° rotated molecule forming two $O\cdots H\text{–}C$ bonds. This bonding scheme is realized in assemblies of related molecular species, see, e.g., next Section 2.3. We ascribe the absence of this motif here to the preferential adsorption sites of the TPA molecules, which would make this arrangement energetically unfavorable.

PDA assembles into chain structures oriented along the [011] and $[0\bar{1}1]$ high symmetry substrate directions as shown in Figure 2.5. The chains consist of well ordered molecular features, although kinks are frequently encountered. For both row directions the long axis of the oval shaped molecule is either aligned with the [001] or [010] substrate orientations. The spacing between the molecules amounts to $3a_0$ (with $a_0 = 2.55$ Å) as in the case of the TPA domains. The chain length can exceed 20 molecules while the the dimer was found to be the smallest stable configuration. Due to the existence of two perpendicular growth directions the maximum chain length is limited. The spac-

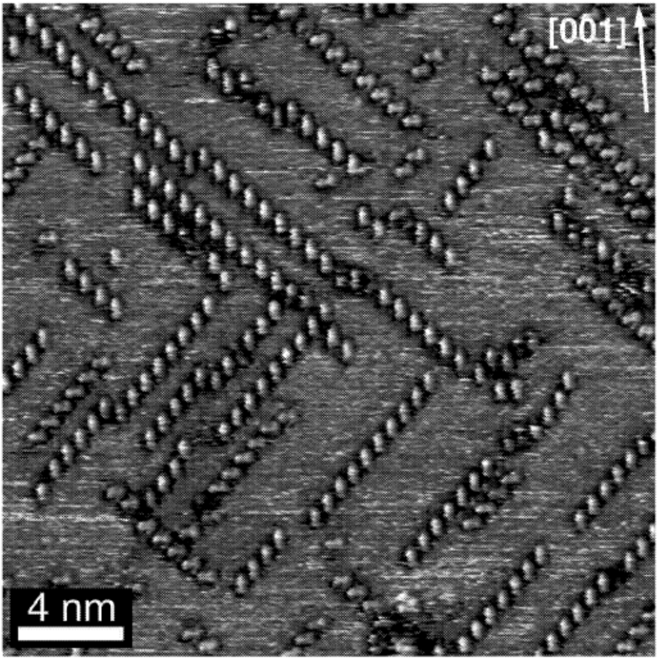

Figure 2.5: STM topograph of self-assembled PDA chains on Cu(100). The rows are oriented along the [011] or [0$\bar{1}$1] substrate directions. For each direction the long axis of the oval features is either aligned with the [001] or [010] directions.

ing between neighboring rows can take any integer number of the Cu surface lattice constant a_0, i.e., no preference for a certain distance is found [15, 137]. Chains of both orientations seem to be randomly distributed on the substrate with no clear indication for domains with parallel molecular rows at low coverage [15]. Only rarely two adjacent rows with a close distance are encountered.

Figure 2.6(a) shows a high-resolution STM image of three PDA rows. In this topograph one PDA molecule is represented as four distinct lobes. The two big and bright central bumps are associated with the molecular backbone. A bone-like black contour in Figure 2.6(a) highlights the shape of these two features. The other two round lobes are asymmetrically aligned with respect to the molecular long axis. Furthermore, they differ in their apparent height. The small protrusions appear on different positions in two mirror domains as can be seen in the upper two chains in Figure 2.6(a).

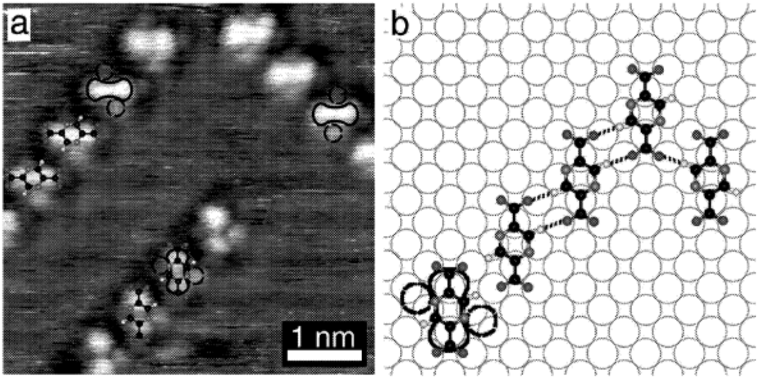

Figure 2.6: (**a**) High-resolution STM image of three distinct chains. The shape of some molecular features is highlighted by black contour lines. Structures superimposed over the data show the chirality and alignment of the molecules. (**b**) Tentative model for the PDA chains. Orange circles mark the atomic positions of the Cu lattice. C, N, O and H atoms are represented by black, light grey, dark grey and white spheres. The contour from the STM image is superimposed over one molecule. Dashed lines mark potential hydrogen bonds between the molecules.

A tentative model is superimposed over the STM topograph in Figure 2.6(a). As shown, the formation of hydrogen bonds between the molecules requires the chirality of the molecular species to be the same within a chain. This implies that the molecules in mirror chains possess opposite chirality. Note that for the formation of lateral hydrogen bonds along the chain direction the molecules need not to be deprotonated, as shown, e.g., in Figure 2.6(b), where the second oxygen atom of a carboxylate moiety is not involved in the bonding. However, 2D islands similar to TPA can be formed if the chains are laterally coupled via OH$\cdots$N hydrogen bridges. Thus, the 1D growth indicates a deprotonated scenario. The lobes within the bone contour can be assigned to the C–C bonds between the carboxylate and pyrazine group. Similar inner structures were also found for TPA and TMLA molecules [5,155]. The lateral round protrusions are located nearby the position of the nitrogen atoms (cf. Figure 2.6(b)). The difference in the brightness of these two features can be a result of a tilted aromatic ring alignment. The actual adsorption position of the molecules can also deviate from the hollow site shown in Figure 2.6(b). Since all molecules reveal the discussed features we presume that they are not due to Cu adatoms as encountered with related molecular systems [139,149,154] (cf. discussion below). However, we cannot exclude that Cu adatoms are involved in the molecular chain formation as they appear to be often transparent to STM [139,154].

The bonding motif is the very same as found in the TPA domains. But in contrast to TPA the attractive lateral interaction between the PDA chains is prevented as the outer C–H groups in the molecular chains are replaced by nitrogen atoms. Thus, other PDA molecules with the appropriate chirality can only effectively bind to the termination of the rows. Kinks can evolve if a molecule of opposite chirality is attached to the terminating PDA molecule as shown in Figure 2.6(b). Only one potential hydrogen bond can be formed in this configuration. Furthermore a potential 2D phase as in the case of TPA can be achieved by an alternating arrangement of molecules with opposite chirality. Similar to the chain structures the molecules in such a phase would be engaged in four $O\cdots H$–C hydrogen bonds as exemplified by the two adjacent different enantiomers in Figure 2.6(b). However, molecules at the boundary would be weaker bound as in the chain phase. Moreover, this structure could be unfavorable because the short distance between the opposite oxygen and nitrogen atoms could give rise to a repulsive interaction. Another possible reason why the vast majority of the molecules form straight rows can be a result of the specific adsorption geometry. An asymmetric adsorption configuration, e.g., a tilted aromatic ring geometry, would hinder the formation of kinks as well as 2D extended phases.

An intriguing feature of the chains is their lateral chemical functionality. Although the alternating arrangement of nitrogen and oxygen atoms prevents direct bonding between the rows it may lead to attractive interactions to metal ions. This may already have consequences for closely spaced chains which can potentially coordinate Cu adatoms in the channel between the rows. The inspection of such row arrangements do not unambiguously reveal the presence or absence of incorporated Cu adatoms. Since closely spaced rows do not occur very often in the low coverage regime the Cu adatom coordination is not very likely.

Despite the detailed and intricate mechanisms of the intermolecular bonding, including substrate mediated and electrostatic interactions, the dimensionality of the self-assembled architectures is a direct consequence of the molecular functionality. The common bonding motif found in the TPA and PDA assemblies results, on the one hand, in two-dimensional long-range ordered domains in the case of TPA and, on the other hand, it leads to the evolution of linear chains. TPA allows for four lateral connections and thus directs the assembly into two dimensions. By contrast, the linearly aligned connective sites of PDA permit only one-dimensional growth.

2.3 Reflecting Molecular Symmetry in 2D Assemblies

Supramolecular chemistry provides powerful methodologies for the controlled generation of nanostructures following bottom-up fabrication principles [34, 42, 132]. Recent studies reveal that surfaces represent platforms to direct the assembly of novel low-dimensional supramolecular architectures using appropriate molecular building blocks [50, 154]. The flexibility of the underlying non-covalent interactions facilitates the formation of thermal equilibrium structures, whose functionalities can be either brick-based or emerge as new or altered quality from molecule-surface interactions [12, 141, 156, 157]. A particularly interesting feature, frequently occurring in low-dimensional supramolecular assemblies, is the rich variety of chirality phenomena encountered at different levels [7, 15, 137, 158, 159].

We performed a comparative scanning tunneling microscopy study addressing the supramolecular ordering of two related molecular building blocks - 4,4'-biphenyldicarboxylic acid (BDA) and 4',4" *trans*-ethene-1,2-diyl-bisbenzoic acid (stilbene dicarboxylic acid, SDA) (cf. Table 1.1) - at the Cu(100) surface. Although bearing the same functional endgroups, the two dicarboxylic acids have different length (13.3 vs 15.5 nm) and symmetry, with BDA belonging to the D_{2h} point group and SDA to the C_{2h} point group (assuming symmetric endgroups by deprotonation). This notably implies that two 2D chiral SDA configurations exist when the molecules are confined to two dimensions (as denoted by δ and λ in Table 1.1). As shown previously, deprotonation of carboxylic groups typically occurs on copper surfaces at the conditions employed for the present study [138, 149, 160]. Consequently, it is concluded that BDA and SDA exist as deprotonated dicarboxylate species at the Cu(100) substrate.

BDA and SDA were deposited onto the substrate held at 298 K. To facilitate the self-assembly processes, we used a coverage slightly below monolayer saturation. Both molecules assemble readily into well-ordered 2-D supramolecular networks with square unit cells of comparable size. The resolution of the rod-like molecules in the STM data as anisotropic protrusions, ≈1 nm in length, reveals that both species adsorb in a flat-lying geometry, in agreement with the bonding of related large aromatic species at metal surfaces [7,12,15,136–138,141,149,156–160]. The lateral intermolecular coupling is mediated by a rather unusual hydrogen bonding between carboxylate moieties and aromatic rings (cf. discussion below). However, the structural information of the higher symmetry BDA molecule is expressed in a single phase with C_4 symmetry (Figure 2.7(a)), whereas the self-assembly of the lower symmetry SDA species goes along with the for-

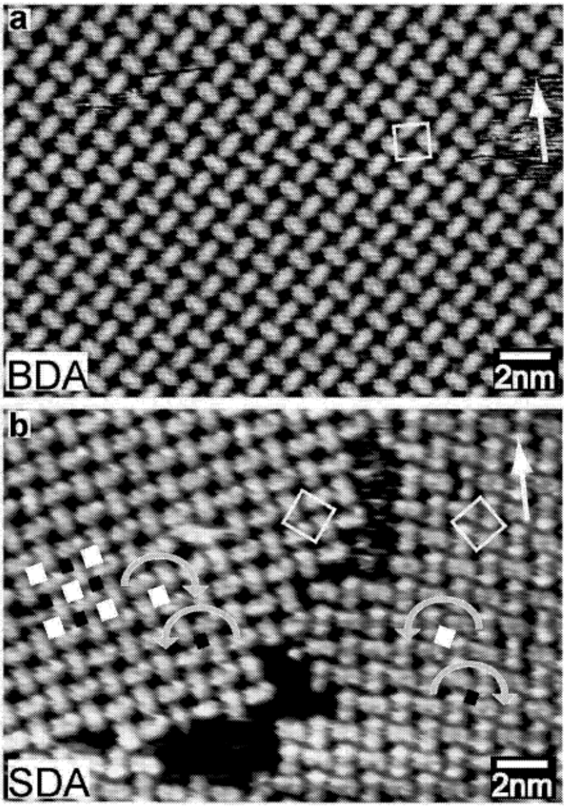

Figure 2.7: STM topographs of 2D dicarboxylate networks: **(a)** BDA; **(b)** SDA. White arrows mark the [001] direction of the Cu(100) substrate. Square frames show the unit cells of the supramolecular motifs. Bent arrows in **(b)** mark SDA folding; the white and black squares represent the large and small voids, respectively.

mation of two enantiomorphic arrangements with $p4$ symmetry (Figure 2.7(b)). Note that the molecular arrangement, bonding length and observed orientation excludes a Cu adatom mediated coupling of the molecules, which was encountered with related systems [149, 154].

The long axes of the BDA molecules align with one of the two high-symmetry directions of the square Cu(100) substrate ([011] and $[01\bar{1}]$). Adjacent BDA molecules are perpendicular to each other, with each endgroup pointing to the center of the next neighbor. This accounts for a quadratic motif with C_4 symmetry. The corresponding unit cell is marked by the square in Figure 2.7(a), which has a side length of 1.45 nm and runs along the substrate [001] direction (marked in Figure 2.7(a)). Following conventional surface science notation, this is a $c(4\sqrt{2}\times4\sqrt{2})$ superstructure. The arrangement shown in Figure 2.7(a) is the only phase observed on the entire sample, and it may cover entire terraces with widths as large as 100 nm.

In contrast, the reduced symmetry of the SDA molecule is reflected in two distinct network phases as shown in the left and right parts of Figure 2.7(b), respectively. Similar to BDA, adjacent SDA molecules are oriented orthogonally. However, the SDA endgroups do not point exactly to the center of the neighboring molecules. This dissymmetric arrangement produces two types of voids, large and small ones, as represented by the white and black squares in Figure 2.7(b), respectively. The corresponding unit cell has a size of 1.54 nm, which is slightly larger than that of the BDA phase and consistent with SDA being the longer molecule. Moreover, the unit cell is oriented 54° counterclockwise off the [001] direction and all large voids (white) are enclosed by four clockwise folding SDA molecules, while the small voids (black) by counterclockwise folding SDA (marked by bent arrows). This arrangement accounts for a $p4$ symmetry, which implies that the motif cannot be superimposed on its mirror image by 2D translation or rotation and that the SDA network is enantiomorphic. The chiral counterpart is found as a coexisting domain, resolved in the right part of Figure 2.7(b), where the large voids are surrounded by counterclockwise folding SDA and the small voids by clockwise folding SDA. This structure has a unit cell of the same size but rotated 54 degrees clockwise off the [001] direction, i.e., the two phases are mirror images with respect to [001]. The two superstructures are described as $[6, 1/-1, 6]$ and $[1, 6/-6, 1]$ in matrix notation, respectively. The different orientations of the molecular networks are associated with the different lengths and shapes of the molecular building blocks. Moreover, unlike the relatively large and perfect BDA networks, in the case of SDA defects and domain boundaries are encountered frequently and the network domain size is typically below 30 nm.

The high-resolution data shown in Figure 2.8(a) provide further insight into the BDA supramolecular assemblies. The symmetric rod-like shape of BDA is clearly resolved. A tentative model is depicted in Figure 2.8(b) (because substrate atomic structure and adsorbed molecules could not be resolved simultaneously, we assume for simplicity that the BDA phenyl rings reside at substrate hollow sites). The lateral coupling of the BDA molecules is associated with two equivalent hydrogen bonds between the carboxylato

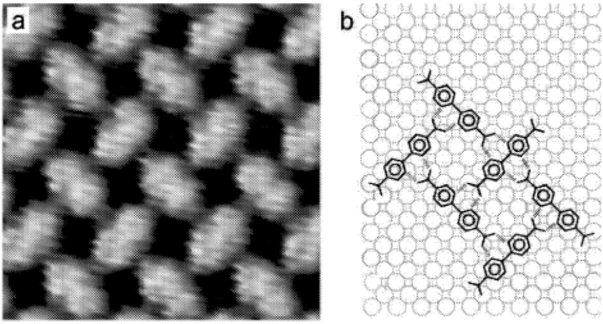

Figure 2.8: **(a)** High-resolution STM data of the BDA supramolecular motifs. **(b)** Tentative model. The red dashed lines indicate lateral hydrogen bonds. The symmetric rod-like species bind centrally to the adjacent molecules via hydrogen bonds between carboxylato groups and phenyl rings. Image size: 4.4 nm × 4.2 nm.

oxygens and the phenyl groups of the adjacent molecules symmetrically (cf. dashed lines in Figure 2.8(b)). Assuming that the adsorbed molecules do not undergo structural relaxations, the O$\cdots$H–C distance is approximately 2.7 Å, falling in the typical range of hydrogen bonds.

The STM topography of the SDA molecules in Figures 2.9(a) and (b) evidences an asymmetric shape, reflecting the crooked molecular backbone due to the ethenylene bridge. Because the molecules are confined flat to two dimensions, the ethenylene bridge accounts for 2D chirality. The chirality signature of the individual molecules can be determined unambiguously from the submolecular resolution images shown in Figures 2.9(a) and (b), where the flection must be associated with the shape of the ethenylene bridge. Figures 2.9(a) and (b) reveal that each of the two SDA phases consists of single enantiomers and hence is homochiral. Consequently, chiral segregation has occurred in the assembly process and the molecular chirality is expressed in the supramolecular motifs. With the tentative models in Figures 2.9(c),(d) the observed structures can be rationalized: the carboxylato groups point to the C–C single bonds, forming hydrogen bonds to a phenyl hydrogen and an ethenylene hydrogen (O$\cdots$H–C distances are estimated to 2.5 and 3.2 Å, respectively; note that this coupling and the molecular geometry imply that the molecules do not match as well with the substrate as in the case of the biphenyl species described above). This nicely explains the distinct large and small voids. Moreover, the smaller SDA network domain size can be attributed to the mass transport required for chiral resolution.

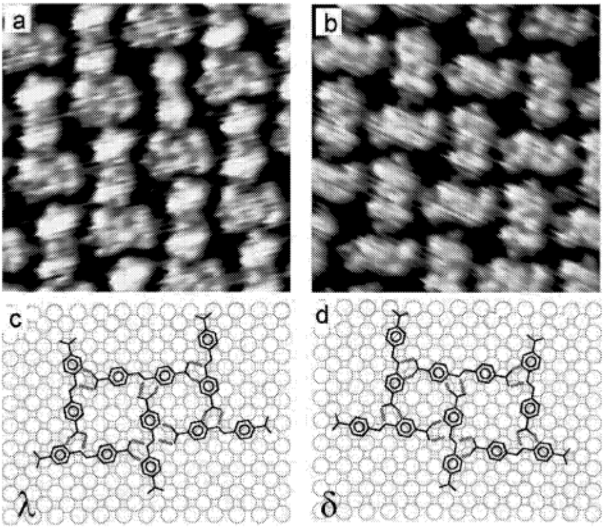

Figure 2.9: (a,b) High-resolution STM data of two enantiomorphic networks of SDA reveal chiral resolution of the 2D chiral (δ, λ) species. **(c,d)** Tentative models. The intermolecular hydrogen bonds reflect dissymmetric coupling (grey lines) of carboxylato to both phenyl and ethenylene moieties. Image size: 4.4 nm × 4.2 nm.

It is interesting to put the present results into perspective with earlier findings for the rod-like species 4-[*trans*-2- (pyrid-4-yl-vinyl)]benzoic acid (PVBA) and 4-[(pyrid-4-ylethynyl)] benzoic acid (PEBA), where intriguing 2D chiral supramolecular ordering phenomena were encountered on the close-packed Ag(111) substrate [15, 46, 161]. In all cases, the matching of the molecular dimensions with the substrate atomic lattice proved to be an important factor for the orientation of the molecules and the supramolecular assemblies. However, for the Ag(111) substrate, the carboxylic acid moieties remain unaffected and H–bonds that could be similarly expected in 3D are decisive for the self-assembly scenario. By contrast, for the case of Cu(100) the substrate modifies the chemical nature of the molecular building blocks. This accounts for carboxylate-mediated intermolecular coupling, whence a H–bond motif rarely encountered in 3D drives the network organization. This emphasizes the important role of the substrate chemical activity in steering the organization and chiral signature of 2D supramolecular assemblies.

Chapter 3

Metal Coordination Structures on Cu(100)

The principles of supramolecular chemistry have been proven to provide valuable strategies for the construction of complex assemblies using molecular building blocks and metal atoms. These design strategies have attracted wide interest due to their ability to synthesize materials with novel properties [34, 38, 41, 42, 52, 132, 162]. Deliberate fabrication of materials with pre-designed topologies, which is an appealing goal from both a scientific and technological point of view, is achieved by reversible, highly selective and directional non-covalent linkages such as hydrogen bonding [34, 41, 42, 132], $\pi-\pi$–stacking, van der Waals forces, metal–ligand interactions [38, 52, 162], etc. The first three interactions are relatively weak resulting in assemblies with limited thermal stability. Metal coordination interactions instead are stronger, more directional than hydrogen bonds and represent the most versatile and widely employed means to direct the organization of molecular building blocks. Such metal-organic coordination networks (MOCNs) have been realized with specific topologies and a high structural stability [38, 163–170]. Furthermore the coordination complexes are not only interesting for topological aspects but also for their intriguing functional properties, which one may exploit in the fields of catalysis, magnetism and optical applications [68, 69, 166, 169–185]. The promise of these construction strategies of creating functional materials has already been demonstrated for different applications, such as second harmonics generation [175, 176], gas storage including size selective sorption and molecular recognition [177–180], catalysis [166, 181–183] as well as applications for magnetic materials [68, 69, 184, 185].

The coordination interaction has been also employed to construct supramolecular architectures at surfaces offering the possibility to design novel low-dimensional materials [5,7,155,156,186–190]. These systems represent unique metal-organic supramolecular materials comprising distinctly arranged transition metal units and 2D cavities with a well–defined geometry and chemistry. In contrast to the traditional coordination chemistry in 3D solution phase, the two–dimensional confinement at the surfaces leads to rather uncommon coordination geometries of the metal centers. In addition the surfaces also actively influence the structures of the materials resulting from the preferred adsorption sites of the different adsorbate species on the substrate. Consequently the assembly principles applied to 3D are modified and a detailed understanding of the processes taking place during the assembly is required to establish the design principles for new 2D coordination chemistry in future.

In this Chapter the emphasis lies in the careful choice of the polytopic organic linkers. We studied the self-assembly of various molecular linkers in conjunction with iron atoms and reveal how the structural properties are determined by the selected subunits. In the following sections we demonstrate the ability of ligands comprising carboxylate, pyridyl and hydroxyl moieties to fabricate a rich variety of two–dimensional structures at a Cu(100) surface. In particular we will shed light on the distinct metal coordination environments and network topologies arising from the different ligand functionalities. In Section 3.4 we will introduce a new concept for the construction of two–dimensional network structures at metal surfaces employing ionic interactions between the charged alkali–metal and carboxylate subunits.

3.1 Fe-Carboxylate Coordination Networks

In this Section we address the influences of the substrate to the previously reported design principles [5, 155] in a comparative scanning tunneling microscopy (STM) investigation on the self-assembly of related metal-organic coordination networks on a Cu(100) surface. In particular we focus on the differences in the detailed structural arrangements emerging from the adsorbate-substrate interactions. The exclusive high-resolution scanning probe method allows us to directly identify the coordination motifs at a single-molecule level. Three rod–like symmetric polybenzene dicarboxylic acids, 1,4-benzenedicarboxylic acid (TPA), 4,4'-biphenyldicarboxylic acid (BDA) and 4,1',4',1"-terphenyl-1,4"-dicarboxylic acid (TDA), shown in Table 1.1, are used in our investigation. Because the three molecules possess the same functional endgroups and symmetry properties, it is expected, that in the absence of the atomic lattice of the substrate identical 2D network topologies evolve. However, while we observed that all three linker molecules form reticular two-dimensional open coordination networks with iron, there are marked differences in the local coordination geometry and overall network topology, which are ascribed to substrate-adsorbate interactions giving rise to preferred adsorption positions and orientations for each species.

Upon adsorption on the substrate held at above or equal room temperature all three molecules form densely packed and well-ordered adlayers with fully deprotonated carboxyl moieties [139, 160, 191, 192] (see also Sections 2.1 and 2.3). In the remaining part of this Section the abbreviations TPA, BDA and TDA refer to the deprotonated species. The iron was deposited after the molecule deposition in order to minimize exchange processes with the copper substrate. The substrate was held at temperatures in the range from 400-450 K during the iron deposition. The sample was then annealed at the same temperature for at least 5 minutes to facilitate the self-assembly process. In the case of BDA and TDA a substrate temperature of 475 K was also used. All obtained MOCNs were found to be robust, with their morphology being maintained up to a temperature of 500 K. In general, we obtained better results for the network formation at higher annealing temperatures, i.e., an increasing domain size and a lower defect concentration. In particular, the evolution of well–ordered network domains of the long molecules BDA and TDA requires a higher preparation temperature compared to TPA. In addition, no dependence of the network topology on the metal-ligand concentration ratio was found for BDA and TDA, as it was observed for TPA (i.e., the mononuclear and row-phases are encountered exclusively for the latter) [155].

(I) TPA networks

TPA forms various types of structures depending on the Fe-TPA concentration ratios and subsequent annealing temperatures. A comprehensive description of all Fe–TPA structures can be found in a previous paper by Lingenfelder et al. [155]. For comparison we focus here on the diiron network structures. As depicted in Figure 3.1, the networks consist of iron pairs surrounded by four carboxylate ligands. The molecules align symmetrically with respect to the iron dimer, i.e., there are two ligands at the bridging (normal to the diiron axis) and two at the axial positions (collinear with the diiron axis). The diiron axis is aligned with the $[0\bar{1}1]$ or $[011]$ substrate directions. The Fe–Fe spacing has been determined from the STM data and amounts to (4.7 ± 0.1) Å (the given error represent the standard deviation). The long axis of the TPA linkers also follows the close packed substrate directions, and thus the networks are aligned with the $[0\bar{1}1]$ or $[011]$ directions. There are two types of structures which differ in the relative orientation of the adjacent diiron units. In the phase shown in Figure 3.1(a), henceforth denoted as α–phase, all diiron units have the same orientation. The network structure possesses a rectangular unit cell with a dimension of 10.2 Å × 15.3 Å, which corresponds

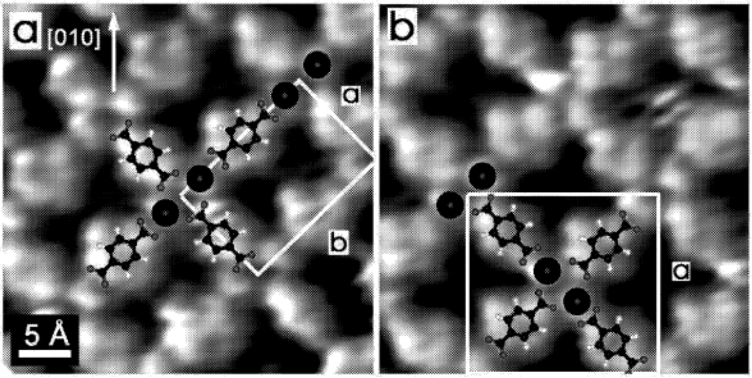

Figure 3.1: STM topographs of the TPA–Fe networks. **(a)** α–phase and **(b)** β–phase. Tentative models and the unit cells of the diiron arrays are superimposed over the data.

to $4a_0 \times 6a_0$ ($a_0 = 2.55$ Å being the nearest-neighboring atomic spacing of Cu(100)). The rectangular open cavities expose an area of 25 Å^2 of the Cu substrate. In another arrangement, represented in Figure 3.1(b) and denoted as β–phase, the orientation of the diiron units alternates by a rotation of 90° in adjacent network nodes. The square unit cell has a size of 18.1 Å × 18.1 Å ($5a_\mathrm{B} \times 5a_\mathrm{B}$, where $a_\mathrm{B} = \sqrt{2}a_0 = 3.61$ Å is the Cu bulk cubic lattice constant), as drawn in Figure 3.1(b). Furthermore the cavities are square shaped with an area of 35 Å^2. The α and β–phases are considered as isomeric structures, because they coexist on the surface with a balanced ratio.

In the α–phase two types of linkers can be identified: those with both ends bridging iron pairs and those with both ends serving as axial ligands. In contrast, all linkers in the β–phase are equivalent, i.e., each molecule is engaged as both a bridging and axial linker. The bridging ligands bind symmetrically to the two Fe atoms in a monodentate configuration while the axial ligands form bidentate bonds to one Fe atom. Each iron atom is thus coordinated by four carboxylate oxygen atoms in a distorted square-planar geometry. The distance from the iron to the four surrounding oxygen atoms is taken from the models and amounts to (2.0 ± 0.2) Å [155], which falls in the range of the typical Fe-carboxylate coordination bond length [193].

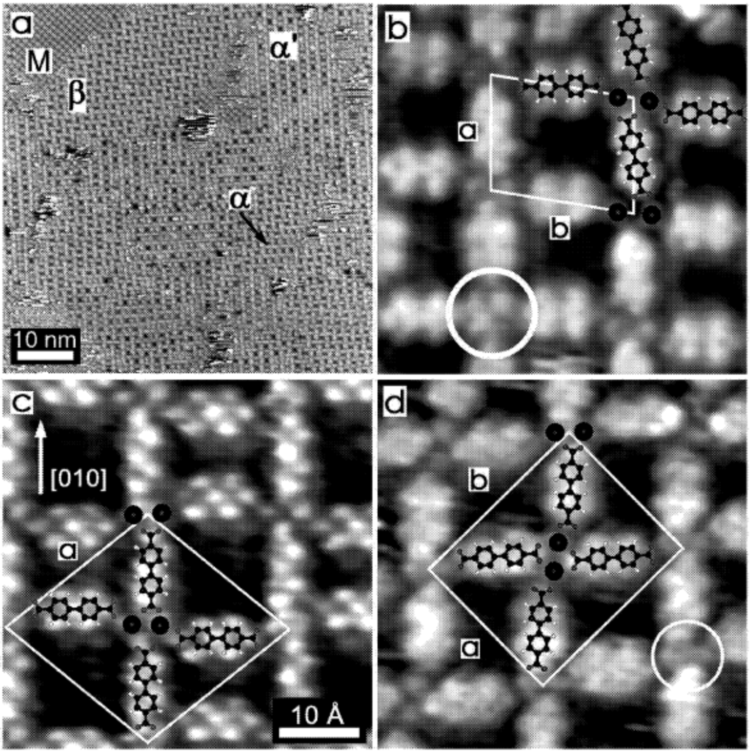

Figure 3.2: STM topographs of the BDA–Fe networks. **(a)** An overview showing the coexistence of the molecular phase (M), α–phase, α'–phase and β–phase. **(b-d)** High-resolution data of α-, α'- and β–phases. (All three images are in the same scale.) The circles in **(b)** and **(d)** mark out defect features.

(II) BDA networks

The BDA linkers form three coexisting distinct network phases upon iron deposition under the same conditions. Figure 3.2(a) shows an overview STM topograph, where the three phases are denoted as α, α' and β, respectively. The α'- and β–phase can form extended domains with approximately the same extension, whereas the α–phase domains are much smaller and appear considerably less frequently. Only very rarely the latter phase consists of more than three rows of cavities and it frequently contains defects. Moreover it does not occur in single isolated domains. The area at the upper-left corner in Figure 3.2(a) (marked by an **M**) is a domain formed by the molecular BDA.

In all the three network phases the nodal points consist of iron pairs. The structures differ, on the one hand, in the orientation of adjacent diiron units, and, on the other hand, in the coordination of the iron pairs by the ligands. In the α–phase, depicted in the high-resolution STM data in Figure 3.2(b), all diiron units have the same axial orientation, as it was also found in the α–phase of the TPA networks. Note that the diiron axis follows the [001] substrate direction, i.e., it is rotated by 45° with respect to the diiron units in the TPA phases. Thus, the network orientations and the molecular linkers are also rotated by 45°. The distance between the two bright bumps at the network nodes associated with the iron atoms amounts to (4.1 ± 0.3) Å, which is smaller than the Fe–Fe spacing in the TPA–Fe structures. The coordination of the diiron units is also remarkably different from that of the TPA–Fe networks. First of all, the axial ligands do not lie in line with respect to the diiron axis, but they are shifted up or down by $\approx$ 1.8 Å. The shifting is upward at one side and downward at the other side at a diiron unit. Due to the shifting of the axial linkers the iron pair in adjacent rows are displaced by about 3.6 Å along the [010] direction, i.e., the displacement is equal to the Cu bulk lattice constant a_{B}. This shifting of the axial linkers produces a staircase arrangement. Another distinction from the TPA–Fe is that the bridging ligands do not point to the center of the iron pair. The long axis of the molecules is tilted by about 10° with respect to the [010] axis, as shown in Figure 3.2(b). Consequently the apexes of the linkers point to one of the Fe atoms. As can be seen in Figure 3.2(b), the upper end of the molecule points to the left-side Fe and the lower one to the right-side Fe. Because of this arrangement the carboxylate groups cannot bridge the iron pair symmetrically, which is illustrated by the superimposed model. The iron coordination will be discussed in details below. A circle in Figure 3.2(b) marks a defect, which may occur in the domains. The unit cell of the diiron array is a rhomboid, as drawn in Figure 3.2(b), where $a = 14.4$ Å and $b = 18.4$ Å. The open cavities also have a rhombohedral shape with a size of 90 Å^2.

The second structure, the α'–phase, is depicted in Figure 3.2(c). The iron spacing within a diiron unit amounts to about (3.7 ± 0.1) Å, significantly smaller than the value in the α–phase. In this particular STM image each BDA molecule is resolved as seven protrusions. Similar to the α–phase the axial ligands are not in line with the diiron axis. However, the iron pairs linked by one axial ligand in Figure 3.2(c) have no displacement along the [010] direction, i.e., in this case the diiron units lie on a line aligned with the

[001] substrate direction. The up- and down-shifting of the axial ligands is opposite for adjacent nodes, resulting in the formation of consecutive wide and narrow rectangular cavities, 145 Å^2 and 55 Å^2 in size, respectively. The bridging linker molecules have a different appearance than the axial ligands: they have an asymmetric shape and they appear thinner than the axial molecules. Moreover, two outer protrusions on one side are brighter than on the other side. This could be an indication for a non-flat adsorption geometry. An influence of the scan direction can be excluded as the rotational domains show the same features. In addition the apexes of the bridging ligands do not point to the middle of the diiron units but rather close to one Fe atom. The bridging ligands at an iron pair point to different iron atoms. A detailed inspection reveals a correlation between the shifting of the bridging and the axial ligands: the bridging ligand is shifted towards the larger void (cf. Figure 3.2(c)). As drawn in Figure 3.2(c) the α'–phase possesses a rhombohedral diiron unit cell with $a = b = 23.1$ Å.

The third structure is shown in Figure 3.2(d) and denoted as β–phase. Similar to the TPA β–phase, the diiron orientation alternates in the structure. Each linker in this arrangement is engaged as a bridging ligand at one end and an axial ligand at the other end. The binding configuration of the diiron units is very close to that of the α–phase. Besides the alternating diiron orientation adjacent iron pairs differ in the ligand configuration: the axial ligands are oppositely shifted in neighboring network nodes. This leads to the existence of a rotational domain, which cannot be superimposed to the structure shown in Figure 3.2(d). Although it is theoretically possible, a structure with identical alignment of axial ligands for both iron dimer orientations has not been observed. Similar to the α-phase the Fe–Fe distance is found to be (4.1 ± 0.3) Å. The rectangular unit cell has the dimensions $a = 20.4$ Å and $b = 25.5$ Å and the area of the rectangular cavities is 90 Å^2.

If the Cu grid is superimposed to the STM data it turns out, that the ligands in all three phases have nearly identical adsorption positions. However, the exact sites could not be determined because it was not possible to resolve the Cu lattice simultanously with the molecular structures. It is worthwhile to mention that the network phases frequently comprise irregularities, as those marked by the circles in Figure 3.2(c) and (d), respectively.

(III) TDA networks

The TDA network structures comprising diiron units divide into two phases that evolve and coexist under the same experimental conditions. Similar to the other molecules adjacent diiron units possess either the same orientation, denoted as α–phase, or alternate

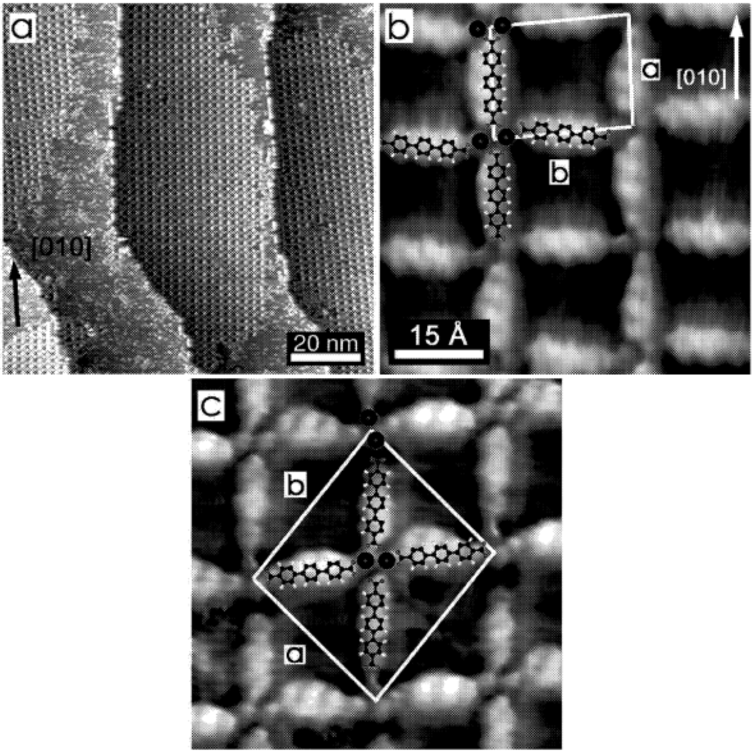

Figure 3.3: STM topographs of the TDA–Fe networks. **(a)** An overview where the two types of α–phase domains enclose an angle of about 4.8° with the high symmetry direction [010]. **(b)** and **(c)** High-resolution data of α- and β–phases (in the same scale).

by a rotation of 90° in the β–phase. The former phase is encountered more frequently than the latter phase, i.e., the α–phase occurs at least twice as frequent as the β–phase. Besides the 90° rotational domains two types of α–phase exist, which have a slightly different orientation with respect to the substrate, as shown in Figure 3.3(a). These two phases enclose an angle of about $4.8° \pm 0.3°$ with the high-symmetry direction [010] or [001] as the bisecting line.

Structural details of the two TDA networks are shown in Figure 3.3(b) and (c). The α–phase has a rhombohedral diiron unit cell (a = 18.8 Å and b = 23.7 Å) with open cavities exposing 260 ± 30 Å^2 of the Cu substrate. A similar binding configuration compared to that of the BDA–Fe α–phase has been found: the bridging ligands do not point to the middle of the diiron units and the axial ligands are displaced up or down off the diiron axis. The two slightly different oriented α–phases differ in their alignment of the axial ligands. While in one phase the left axial molecule is shifted downwards and the right axial ligand is shifted upwards at a diiron unit, as shown, e.g., in Figure 3.3(b), it is opposite for the other phase. Thus, the two phases are mirror domains with respect to the [010] or [001] directions. In contrast to the BDA α–phase, the detailed inspection of the TDA α–phase reveals that the bridging ligands as well as the axial linkers do not have identical orientations. Furthermore, the shape of the molecules varies significantly but no superstructure has been found for the variations. In the β–phase the iron pairs form a large rhombohedral unit cell ($a = 27.5$ Å and $b = 31.1$ Å), as drawn in Figure 3.3(c), where the area of the cavities is slightly smaller (220 Å^2). Also in this phase the iron pairs as well as the ligands display different shapes (see discussion below). The iron-iron distance in both phases amounts to (4.3 ± 0.5) Å, where the relatively large error arises from a broad distribution of the diiron spacing. An analogy to the BDA α'–phase has not been observed.

The STM data of the TDA network structures reveal some features that are absent for the other two linker molecules. Some of the linkers appear broadened or asymmetric, as can be seen in Figure 3.4 (molecules marked by circles), i.e., one end is narrower than the other. Since the width of the broadened features is too small for two parallel TDA molecules, we ascribe the broadening to a molecular movement. That means the molecules are oscillating between two sites during the STM data acquisition. The frequency of the oscillation is higher than the line scan frequency as the molecule is well resolved in the two positions (line scan: 2ms). Similar phenomena were reported previously in literature [194]. In the case of the asymmetric molecules the narrow end is fixed while the mobile end appears broadened. The data also shows that the oscillation always occurs at both axial positions of a diiron unit. This is corroborated by the fact that the opposite axial ligands are always shifted in an anti-phase manner, and hence both molecules presumably oscillate contrarily to each other. Consecutive images taken at the same area on the surface in a time frame of one hour show that the movements always occur at the same metal centers. The oscillations are responsible for the wide range of the apparent cavity size ($\Delta = 30$ Å^2). These oscillations do not occur in the β–phase.

The bistability of some axial linkers can be related to distortions of the network structure induced by the coupling of the adsorbates to the surface. The angle of about 2.4° of the α–phase structures to the [001] direction impedes that adjacent iron pairs

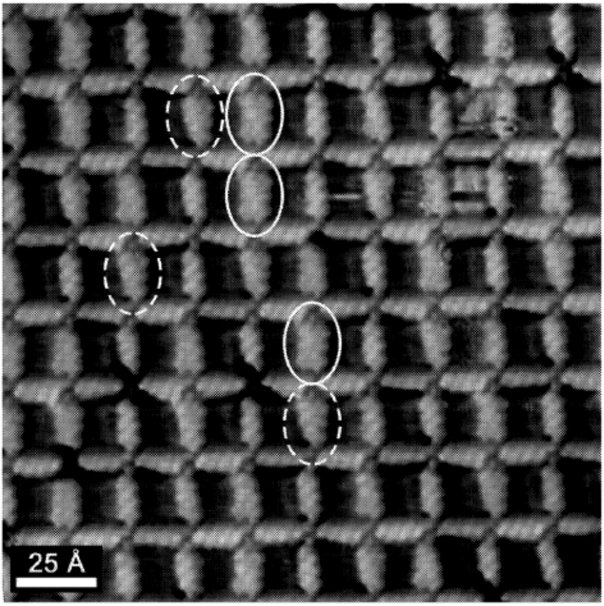

Figure 3.4: STM topograph of a TDA–Fe network domain showing the symmetrically (in solid circles) and the asymmetrically (in dashed circles) broadened molecules.

reside on exactly the same adsorption site. This causes slightly different coordination geometries due to the interaction with the substrate, and thus, it could result in the mobility of a few of the axial linkers.

Discussion and Conclusions

The topology of the networks is expected to be independent of the backbone lengths of the ligands without taking into account the influence of the copper substrate. Our observation demonstrates that the substrate plays a significant role in the network formation. The interaction of the molecules with the substrate induces drastic changes in the coordination configuration of the diiron units as the number of the aromatic rings varies from one to three. And thus, the overall network topology varies for the three molecules. The adsorbate–substrate interaction gives rise to favored orientations of the network structures with respect to the surface and, for symmetry reasons, the presence of rotational and mirror domains. Table 3.1 summarizes the topological parameters of

Structure	**Diiron Unit Cell**			**Fe-Fe**		**Cavity**	
	a **(Å)**	b **(Å)**	**orientation**	**spacing (Å)**	**orientation**	**exposed surface (Å^2)**	**shape**
TPA - α	10.2 ($4a_0$)	15.3 ($6a_0$)	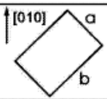	4.7 ± 0.1	[011] or [0$\bar{1}$1]	25	rectangle
TPA - β	18.1 ($5\sqrt{2}a_0$)	eq. to a	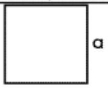	4.7 ± 0.1	[011] and [0$\bar{1}$1]	35	square
BDA - α	14.4 ($4\sqrt{2}a_0$)	18.4 ($\sqrt{52}a_0$)	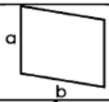	4.1 ± 0.3	[010] or [001]	90	rhomboid
BDA - α'	23.1 ($\sqrt{82}a_0$)	eq. to a	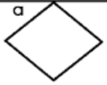	3.7 ± 0.1	[010] or [001]	145 & 55	rectangle
BDA - β	20.4 ($8a_0$)	25.5 ($10a_0$)	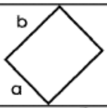	4.1 ± 0.3	[010] and [001]	90	rhomboid
TDA - α	18.8	23.7	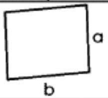	4.3 ± 0.2	[010] or [001]	260 ± 30	rhomboid
TDA - β	27.5	31.1	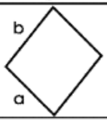	4.3 ± 0.5	[010] and [001]	220	rhomboid

Table 3.1: Summary of the topological parameters of the network phases ($a_0 = 2.55$ Å).

the obtained networks. TPA–Fe networks display most well–defined structures, strictly following the substrate lattice. The BDA–Fe networks are expected to be commensurate with the Cu substrate as well. In contrast, the unit cells of the TDA–Fe networks cannot be unambiguously correlated to the Cu(100) lattice. In particular the small angle of the α–phase domains to the high symmetry directions prevents adjacent iron pairs to possess identical adsorption sites. Nevertheless the distinct domain orientations with respect to the substrate are attributed to surface templating. The results demonstrate that the molecule–substrate interaction is sufficiently weak to allow the self-assembly of the favored diiron motif, but it is strong enough to alter the topology of the network structure.

Regarding the Fe coordination TPA is the only case where a square-planar coordination can be defined. The Fe coordination of the two longer molecules BDA and TDA is more complicated and cannot be deduced unambiguously from our data. The common motif where the axial ligands are always displaced off the diiron axis suggests two possibilities: supposing that all carboxylate groups lie in a same plane a planar trigonal coordination geometry can be achieved. Such configuration is very rare in three-dimensional compounds. However, the surface contribution must be taken into account here. In addition, the second carboxylate oxygen atom of the axial linkers may potentially form a hydrogen bond to the nearby bridging ligand, which may additionally stabilize this arrangement. The second scenario is a distorted tetrahedral coordination if the carboxylate moieties of the axial ligands are tilted out of the plane. An exact model for the three-dimensional coordination environment cannot be deduced from the STM data. In particular, the arrangement of the metal-carboxylate bonds is not directly accessible and may have a complicated 3D arrangement. Further studies are required to gain full insight into the coordination configuration. The different values of the Fe–Fe spacing are ascribed to a subtle balance between adsorbate–substrate and lateral coordination interactions. Hence, the Fe–Fe distance is a result of commensurability of the network structure with the copper surface registry. These differences in the spacing and coordination environment could give rise to differences in the electronic properties of these iron centers, which might result in distinct magnetic and catalytic properties [195, 196].

With regard to the growth conditions the three molecules differ mainly in the annealing temperature. The main driving force in the network formation is the appropriate binding of the carboxylate groups to the iron under the constraints of special adsorption sites for the iron atoms, the carboxylate oxygen and the aromatic rings, where the latter is expected to play a larger role. The higher required annealing temperature for BDA and TDA compared to TPA is a result of the reduced mobility of these molecules. The higher mass and the increased translation and rotation barriers of the longer ligands contribute to this reduction. Another reason can be an increased barrier for the evolution of long-range ordered network domains because of the formation of intermediate metastable complexes. Because the molecules form well-ordered domains before iron deposition the energy required to dissolve the molecular phase must also be taken into account. Generally speaking the preparation temperature needs to be sufficiently high to provide an adequate mobility of the molecules and iron atoms as well as to remove unwanted bonding like hydrogen bonds or to correct mis-engaged Fe-carboxylate bindings.

In conclusion, we have studied the self-assembly of two-dimensional open network structures formed by TPA, BDA and TDA and co-deposited iron on Cu(100). The size of the cavities increases almost one order of magnitude from the shortest (TPA) to longest (TDA) linker. The realized network structures result from the subtle interplay between the coordination interactions between metal centers and the carboxylate groups and the interactions of the linker molecules and Fe atoms with the substrate. The latter significantly affects the topology of the networks, e.g., orientation and geometry, whereby the iron-iron spacing varies from 3.7 Å to 4.7 Å. In principle one may exploit the substrate induced changes to steer the topology and more importantly the local metal coordination environment of surface–supported metal–organic networks by selecting proper substrates and linker molecules.

3.2 Fe-PVBA Structures - A Heterofunctional Ligand

The previous studies revealed the suitability of polytopic carboxylate linkers in conjunction with iron atoms for the engineering of a variety of two–dimensional networks [5, 7, 155, 156]. A drawback in both 2D and 3D arrangements is the frequently encountered stereoisomerism, preventing from the realization of structurally homogenous phases [5, 38, 155]. However, a strategy to act on the assembly of supramolecular arrays notably elaborated for the organization of open 3D dimetal–based systems using polycarboxylate and polypyridyl species consists in the careful choice of bridging ligands [173, 197, 198]. In order to address this issue we undertook a comparative study to explore homogenous coordination network formation and regular positioning of diiron centers at surfaces.

The key ideas are demonstrated in Figure 3.5, where the effect of linker functionality and reduced symmetry on the 2D organization of iron pairs mediated by exemplaric linear linkers is illustrated. (Note such configuration is stabilized by the surface. In 3D diiron carboxylate presents as paddle wheel units that are linked by the respective link [199].) A ditopic carboxylato species may act as either equatorial or axial linker (following the definition in ref. [197]), i.e., both network isomers **1** and **2** in Figure 3.5 may evolve [5] (cf. previous Section 3.1). In phase **1** each dicarboxylato species is employed strictly as an equatorial or as an axial linker. Hence all diiron units are lying parallel. By contrast in phase **2** the dicarboxylate acts as equatorial linker at one side and as axial linker at the other side. As a result adjacent diiron units are rotated by 90°. Now, when we use a dissymmetric linker molecule with a carboxylato group at one end

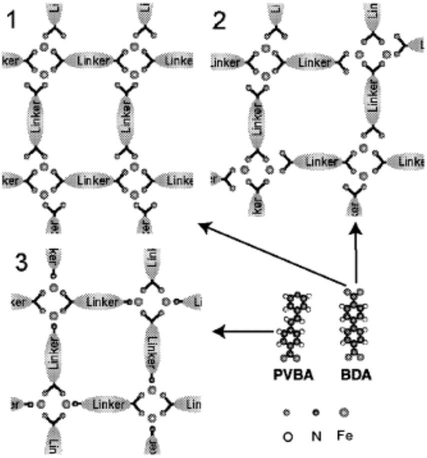

Figure 3.5: Concept of ligand control at 2D.

and a pyridyl group at the other end the isomerism vanishes. Rather, a unique favorable solution for network formation exists, since the pyridyl moiety couples preferentially in an axial fashion to the diiron units. As a consequence the iron pairs orientations in phase **3** must alternate.

The phases **1** and **2** illustrated in Figure 3.5 are encountered in TPA, TMLA, TDA and in particular the BDA network structures [5, 155, 156, 190] (see also previous Section 3.1). The heterofunctional linker 4–[*trans*–2–(pyrid–4–ylvinyl)]benzoic acid (PVBA) was employed to realize phase **3**. With appropriate surface concentrations and metal–ligand ratios 2D reticulated regular network structures comprising diiron units evolve after 450 K annealing for 5 min on the Cu(100) substrate (cf. Figure 3.6(a)). As illustrated in Figure 3.5, both rod-like molecules BDA and PVBA are comparable in length, comprise two aromatic rings as backbones and two functional endgroups. Whereas BDA is centrosymmetric with two terminal carboxyl moieties, the noncentrosymmetric species PVBA comprises a carboxyl and a pyridyl group at its extrema [200]. Under the employed preparation condition the molecules carboxyl groups are deprotonated, providing reactive carboxylato ligands for metal coordination [5,155]. The aromatic backbones are crucial for the engineering of nanoporous metal-organic networks because they promote the flat adsorption and orientational ordering of the linkers at the surface [5, 15, 155] (see also previous Section 3.1).

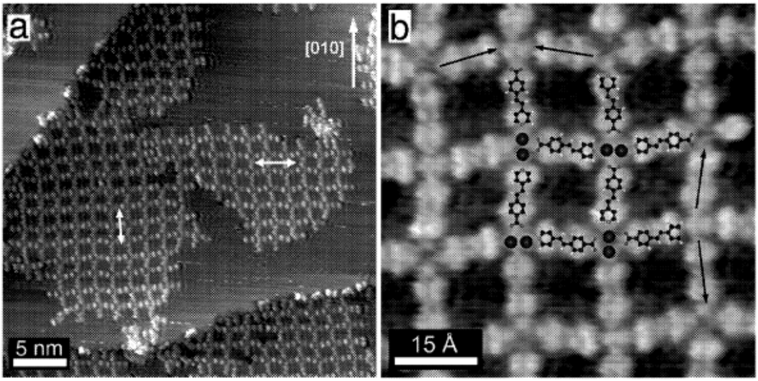

Figure 3.6: **(a)** STM topograph of PVBA network domains. Molecules along one direction, marked by arrows, exhibit the same orientation. **(b)** High resolution STM image of the PVBA-network structure. Tentative models are superimposed over the data indicating the coupling schemes. The arrows pointing to the pyridyl group illustrate the different orientations of the enantiomers.

High-resolution STM topographs allow for the identification of the diiron units, thus permitting the unambiguous distinction of different phases. Representative STM data of the metallosupramolecular BDA and PVBA networks is shown in Figure 3.2 and 3.6(b), respectively, where the iron atom pairs, i.e., two iron atoms spaced by ≈ 3.6 Å, are clearly resolved. Two phases, notably differing in the arrangement of the diiron units, are encountered in the Fe-BDA system. As anticipated in Figure 3.5, both parallel and alternating orientation of adjacent pairs exist, which is demonstrated in Fig. 3.2(c) and (d), respectively. These structures are described in detail in the previous Section 3.1. They represent energetically equivalent products resulting from the same sample preparation and reflect the phases **1** and **2** in Figure 3.5.

In marked contrast, a pure phase with regularly arranged diiron units could be reproducibly obtained in the case of Fe-PVBA networks. The STM data reveal that the orientation of adjacent diiron pairs strictly alternates. In Fig. 3.6(b) a high-resolution image is reproduced, which corresponds to the realization of the network **3** established on the conceptual grounds presented in Figure 3.5. As illustrated by the superimposed tentative model, for each PVBA molecule the carboxylate group forms two monodentate coordination bond with a diiron unit as an equatorial ligand, whereas the pyridyl moiety at the other side is engaged as an axial ligand in the linkage to the adjacent diiron unit.

This asymmetric bonding necessarily implies an alternating orientation of neighboring iron pairs. Since this is the only favorable coupling scheme, the defect concentration is minute.

The oblique shape of the framework voids reflects the crooked shape of the linker backbone. A closer inspection reveals some interesting features. Apart from a 90° rotation there exist two different molecular orientations as marked by the arrows in Figure 3.6(b). As shown in Figure 3.6(b), these orientations correspond to the two enantiomers of PVBA. Adjacent ligands along the cavity rows, indicated by arrows in Figure 3.6(a), must have the same orientation in order to form extended network structures. Two adjacent molecules with opposite chirality would result in a too wide or narrow gap between the open ends of the molecules which cannot be bridged by a single PVBA molecule. This implies an intrinsic error correction scheme to remove unwanted bindings of different neighboring enantiomers. Furthermore, the chiral resolution of the molecules within the rows entails a considerable mass transport at the surface, which limits the domain size compared to that of BDA. Apart from the rows, the chirality of the molecules does not exhibit a certain or conspicuous pattern, so that the domains are not necessarily homochiral. Hence, the network comprises only a quasiperiodic arrangement of diiron units.

We achieved improved control of nanoporous systems and transition metal atom pairs at metal substrates by choosing heterofunctional linker molecules. The results furthermore nicely reveal that nitrogen containing units can be readily employed in metal–directed assembly of organic species at surfaces. These findings exemplify the rational design principle in nanostructure synthesis at surfaces. Moreover the pyridyl ligands are not only interesting for structural aspects. Compared to the BDA–structures in Section 3.1 the replacement of the charged carboxylate axial ligand by the neutral pyridyl group is expected to result in an altered electronic structure of the coordinated diiron unit. This might be an appealing feature for the development of novel surfaces–supported catalysts.

3.3 Fe-Hydroxyl Coordination Networks

In the previous Sections 3.1 and 3.2 and related studies [5, 138, 155, 186, 188, 189, 201] the suitability of carboxylate and pyridyl organic linker molecules in conjunction with transition metal coordination centers for the construction of coordination structures at surfaces is demonstrated. These systems show a rich variety of distinctly arranged mono- and dinuclear transition metal units. The occurence of dinuclear coordination centers is a result of the bridging capability of the carboxylate moiety. In addition square–planar coordination geometries are encountered in the mono–iron carboxylate structures. These coordination environments are dictated by the specific carboxylate coordination of the metal centers. Hence, the exploration of new types of ligand molecules and binding motifs will extend the design strategies for low-dimensional architectures at surfaces.

Here we report on the synthesis of surface-supported metal–organic coordination structures possessing single threefold coordinated iron centers. The hexagonal (honeycomb) networks were attained by the self-assembly of the organic linker 4,4'–dihydroxybiphenyl (DHBP) and Fe atoms. The mono–iron centers are coordinated by the hydroxyl groups in a trigonal geometry. Honeycomb metal–organic networks are rarely encountered because trigonal coordination geometries do not occur very frequently [202–204]. Our results demonstrate that the surface–assisted assembly opens a new avenue of coordination chemistry. Furthermore we studied the influence of the substrate on the network topologies by using two distinct single crystal surfaces, Cu(100) and Ag(111), with fourfold and threefold symmetry, respectively. These surfaces have been also employed in previous studies of similar molecular nanostructures [136, 192]. The structures were characterized by scanning tunneling microscopy at room temperature under ultra–high vacuum conditions at the single–molecule level.

DHBP molecules and Fe atoms were subsequently deposited on the metal surfaces. The Fe deposition were performed at a substrate held at 400 K to increase mobility of the adsorbates. After the metal deposition the substrate was kept at the same temperature for 1 min to facilitate the network formation. By employing different preparation conditions we observed that at a lower deposition temperature ($\approx$375 K) the mobility of the ligands is not sufficient to form extended coordination structures while at higher preparation as well as post–preparation temperatures ($>$ 450 K) the coexistence of iron clusters and DHBP molecular phase is observed, signifying that the iron–hydroxyl coordination is weaker than the corresponding Fe–carboxylate coordination [5, 7, 155, 156]. At elevated substrate temperatures ($>$ 450 K) the iron is lost in irreversible competing surface processes, such as exchange reactions with surface Cu atoms or cluster formation.

In Figure 3.7(a) an overview of the network structures assembled at the Cu(100) surface is reproduced. The size of a single domain can exceed 40 nm in diameter. We observed four different domain orientations (three are present in Figure 3.7(a)), which are related to each other by rotation and mirror symmetry operations according to the surface symmetry point group. Although the structure is extended in two dimensions, a strict periodicity with a length of 22 Å is only obeyed in one direction (cf. the arrows in Figure 3.7(a)). These row orientations have an angle of $\pm(9.5^\circ \pm 0.5^\circ)$ to the

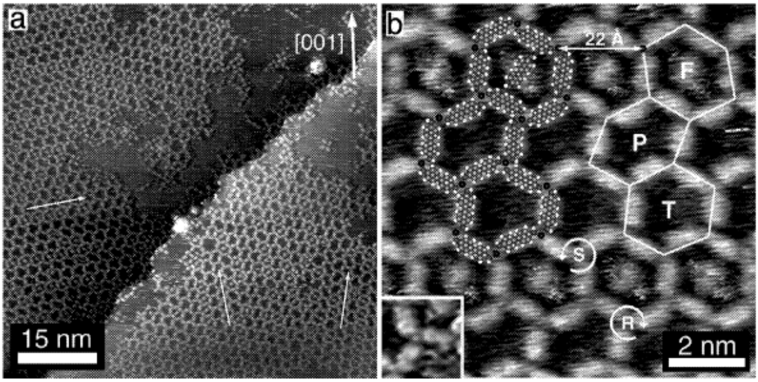

Figure 3.7: **(a)** STM topograph of the hexagonal network structure with three different domain orientations on Cu(100) as indicated by small arrows. **(b)** Detailed STM image of the network structure on Cu(100). Tentative models are superimposed on some cavities. The positions of the iron atoms are connected by white lines for the *F*-, *P*- and *T*–voids. The periodicity length of 22 Å along the $[06\bar{1}]$ direction is marked by an arrow. The bent arrows labelled with R and S denote clockwise and counter clockwise folding of the molecules at an iron center, respectively.

[001] or [010] crystal principal axes, which can be assigned to the [061] and equivalent substrate directions. One can distinguish three types of rows consisting of hexagonal cavities with different shapes (cf. Figure 3.7(b)). The first type of cavity, denoted as *T*–cavity, possesses almost a C_3 symmetry. The other two types reveal a less-symmetric parallelogram-like envelope (*F*- and *P*–cavity) as indicated in Figure 3.7(b). All types of voids occur at approximately the same frequency. About 75% of the *F*–cavities are filled by a single DHBP molecule. The other two types of cavities can also accommodate single DHBP molecules but the filling ratio is much lower: only 10% for the *T*- and 3% for the *P*–type (see, e.g., Figure 3.7(b)). We presume that the inclusion is stabilized by weak hydrogen bonds between the hydroxyl oxygen to the phenyl hydrogen atoms of the rim molecules. The preferential adsorption positions of the DHBP molecules would be an explanation why only one cavity type is dominantly filled. The cavity rows arrange according specific rules. First of all, the *P*- or a *F*–rows are always followed by another type of row, i.e., we have never observed two adjacent *P*- or *F*–rows. The majority of the *T*–rows also adjoins to other row types. Only less than 4% of the *T*–rows are adjacent to another *T*–row. The specific alignment of the molecules at the iron

centers prevent that the *P*- or *F*–rows can be adjacent to a row of the same type. (see detailed discussion below). Second of all, apart from the inserted *T*–rows the *P*- and *F*–rows are alternatingly arranged. Furthermore, only a few configurations between two *F*–rows are allowed, namely [*P*] and [*TP(nT)*], where nT stands for zero or more *T*–rows. Note that the arrangement is not necessarily identical for two different domains, i.e., no superstructure has been observed.

The single iron atoms in the network nodes, occasionally imaged as single protrusion at the network nodes (see inset in Figure 3.7(b)), form a distorted 2D hexagonal lattice with a nearest-neighbor distance of approximately 13 Å. In Figure 3.7(b) tentative models are superimposed over the STM topograph. The exact adsorption positions of the irons and the DHBP molecules with respect to the substrate are unknown, because we did not simultaneously resolve the atomic lattice of the copper surface. We assume that the molecules are preserved under the experimental conditions, in particular no deprotonation of the hydroxyl group occurs which is encountered for related aromatic carboxylic acids [136, 155, 190]. As shown in Figure 3.7(b) the central iron atom is coordinated by the three oxygen atoms of the surrounding hydroxyl moieties in a trigonal planar geometry. The angles between the ligands deviate from the 120° with one at $110°\pm5°$ and the other two at $125°\pm5°$. The hydroxyl moieties fold around the central Fe atom either clockwise (R) or counter clockwise (S), which creates 2D chirality [189,201]. A *T*–type hexagon consists of an alternating arrangement of three R- and three S–centers (-RSRSRS-) while a *F*–cavity has two R- and four S–centers (-RSSRSS-) and a *P*–cavity four R- and two S–centers (-SRRSRR-). The latter two voids possess an opposite arrangement of the chiral units. Altogether, the overall ratio of the two enantiomers is balanced resulting in a global racemic phase.

At the Ag(111) substrate we obtained more extended honeycomb structures, as shown in Figure 3.8(a). The network domains can grow continuously over entire terraces, frequently exceeding 100 nm in diameter. The STM image presented in Figure 3.8(a) shows two domains with a different orientation, as indicated by the arrows, which enclose an angle of $14.5° \pm 1°$. The domain boundary (dashed line) comprise distorted hexagons as well as pentagon–heptagon lattice faults. Figure 3.8(b) reveals two different types of hexagonal cavities (indicated by *T* and *C*). More than half of the cavities belong to the *T*–type which has a C_3 symmetry, similar to the *T*–type on Cu(100). The nearest-neighbor distance amounts to approximately 13 Å. The *C*–type hexagons are compressed in one direction leading to a shorter Fe–Fe spacing of about 11 Å along the compressed edges. In contrast to the copper substrate we have not found inclusions in the cavities (no *F*–type) here. There exist three *C*–cavity orientations within a net-

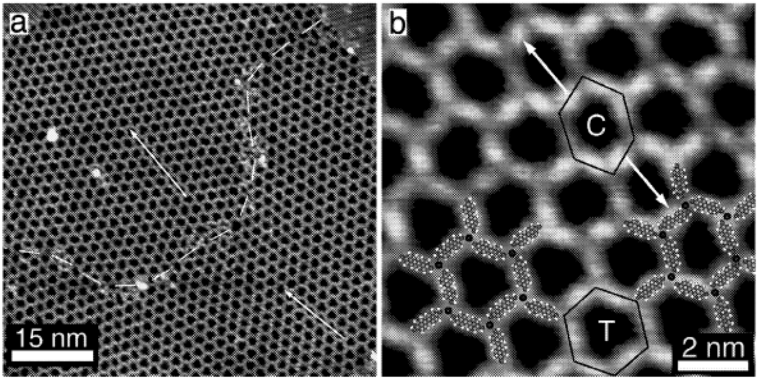

Figure 3.8: **(a)** STM topograph of the Fe–DHBP honeycomb structure on Ag(111). The two domains (indicated by the arrows) are separated by a clear domain boundary (dashed line). **(b)** STM image of a part of a network domain on Ag(111). The shape of the *C*- and *T*–cavities are highlighted by black contours. Tentative models for a *T*- and *C*–void are superimposed over the data. The *C*–cavities often go through the entire domain as indicated by the white arrows.

work domain with a rotation angle of 120°. The *C*–cavities tend to align in rows that frequently go through a single domain, as indicated by the arrows in Figure 3.8(b). Occasionally two *C*–rows can cross each other and various deviations from the two major types of hexagons can occur at the cross.

Also for this phase we could not determine the precise adsorption positions of the molecules and metal atoms due to the same reasons as for the copper substrate. In Figure 3.8(b) we present a tentative model of the molecular arrangement superimposed over the STM data. The molecule–molecule angles of the *T*–hexagons amount to 120°, as expected for a perfect honeycomb. For the *C*–cavity the angles can deviate by approximately 20° from 120°. The coordination also shows the characteristic 2D chirality as on the Cu(100) surface. Similarly, the *T*–cavities comprise alternately arranged chiral centers. The tentative model of the *C*–void presented in Figure 3.8(b) reveals a (-RSSRSS-) as it was found for the *P*- or *F*-hexagons on Cu(100). Hence, the overall structure including all domain orientations represents a racemic phase.

The networks formed on both surfaces display a common threefold coordination of the iron atoms by the hydroxyl groups. The evolution of topologically identical structures at the substrates bearing different symmetries indicates that the metal–ligand interaction dominates the network formation. Despite the similarities the structures at the two surfaces differ in the shape and organization of the hexagons, the existence of different rotational and mirror domains and the size of single domains. We attribute these differences to the specific adsorbate–substrate interactions at the two surfaces. Due to these interactions the molecules and metal atoms prefer certain adsorption sites at the surface. Hence, the realized structures are a result of the interplay between the metal–ligand interactions and relaxation forces arising from the substrate registry.

Hexagonal structures have already been achieved via hydrogen bonding on various substrates using the self-complementary carboxyl group or other special designed functional moieties [12, 136, 140, 141, 192, 205]. Compared to the H–bonding systems the metal–coordination reveals several advantages: (1) higher thermal stability (≈ 400 K), most H–bonding open networks collapse at that temperature; (2) structural flexibility, in particular the bonding angles may deviate from 120°, which facilities the growth of extended network domains at various surfaces; (3) specific bonding, which reduces the frequently encountered structural faults in the H–bonded assemblies.

The fabrication of two-dimensional MOCNs with a hexagonal topology demonstrates that a planar trigonal coordination of single iron atoms can be realized by employing hydroxyl ligands. This result extends the previously reported design strategies of the surface-assisted coordination assemblies.

3.4 Novel Coordination Structures via Ionic Interactions

In the previous Sections and in the literature it has been shown that the concepts of supramolecular chemistry have been successfully employed to attain surface-supported nanostructures with programmable topology via molecular self–assembly [5–8, 12, 156, 190, 205–208]. The specific interactions between the building blocks to steer the molecular arrangement comprise hydrogen-bonds, metal coordination and dipolar forces. Recently, ionic self-assembly, i.e., the coupling of different components by electrostatic forces, has become a powerful tool to fabricate materials with unique structural and chemical properties [209–211]. Charge units are organized by employing Coulomb interactions resulting in versatile supramolecular systems. The advantage of the ionic self-assembly lies in the simplicity and flexibility of the synthesis processes and the abundance of the starting molecular building blocks. To our knowledge, the concepts of the ionic self-assembly have been only used for bulk materials, such as liquid crystals [211], and the fabrication process is always carried out in wet–chemical environments. Here we demonstrate the potential of ionic interactions to construct rationally designed 2D networks at a metal surface under solvent-free "dry" (ultra-high vacuum) conditions. Organic molecular anions and alkali metal cations can cooperatively assemble into nano-scale architectures at a surface via ionic bonding. The specific properties of the interaction facilitates the growth of almost defect-free network domains at modest temperatures. The topology of the structures is tailored by choosing organic linker molecules with defined geometries.

The molecular structures of the three symmetric linear organic molecules used in this study, namely TPA, BDA and TDA, are shown in Table 1.1. A common structural feature of the molecules is the linear aromatic backbone, which entails the flat-lying molecular adsorption at the metal surface, i.e., with the aromatic rings parallel to the surface (see refs. [4,8,136,160,191] and also Sections 2.1 and 2.3). The carboxyl groups at both ends of the molecules, with an $O\cdots O$ distance along the long axis of 7.1 Å, 11.4 Å and 15.7 Å, respectively, deprotonate when the molecules adsorb at a Cu(100) surface above 300 K, and thus become anionic carboxylate species [139,160,192]. In the remaining part of the Section the abbreviations TPA, BDA and TDA refer to the deprotonated ionic species. On top or before the organic precursor layer with a coverage below full monolayer saturation Cs atoms were deposited onto the substrate according to the procedure described in Section 1.3. The Cs atoms adsorbed at the metal surface undergo partial charge transfer to the substrate and behave as cations [212–214]. Thus the carboxylate linkers and the Cs ions represent complementary building blocks for ionic coupling. At proper concentrations and molecule-to-Cs ratios, the mixtures of the molecular anions and the Cs cations readily self-assemble at room temperature or moderate elevated temperatures (≈ 350 K) into two-dimensional architectures stabilized by ionic interactions.

In Figure 3.9(a-c) STM topographs of the cavity structures of TPA, BDA and TDA are presented, respectively. In all images the molecular linkers and the central Cs atoms are clearly resolved. The structures evolve under certain Cs–molecule ratios at a room temperature substrate. A variety of other Cs ion directed structures have been found under different conditions (see discussion below). As shown in Figure 3.9(a-c) all three molecules organize with Cs in square network structures comprising open voids. The models superimposed on the data display that in all three cases the central Cs atom is surrounded by four carboxylate moieties, signifying the attractive interaction between the positive charged Cs atoms and the negative charged carboxylate groups. At a first glance the overall charge of the four carboxylate groups is not balanced by the central Cs ion. However, the metal substrate may effectively screen the unbalanced charge. In

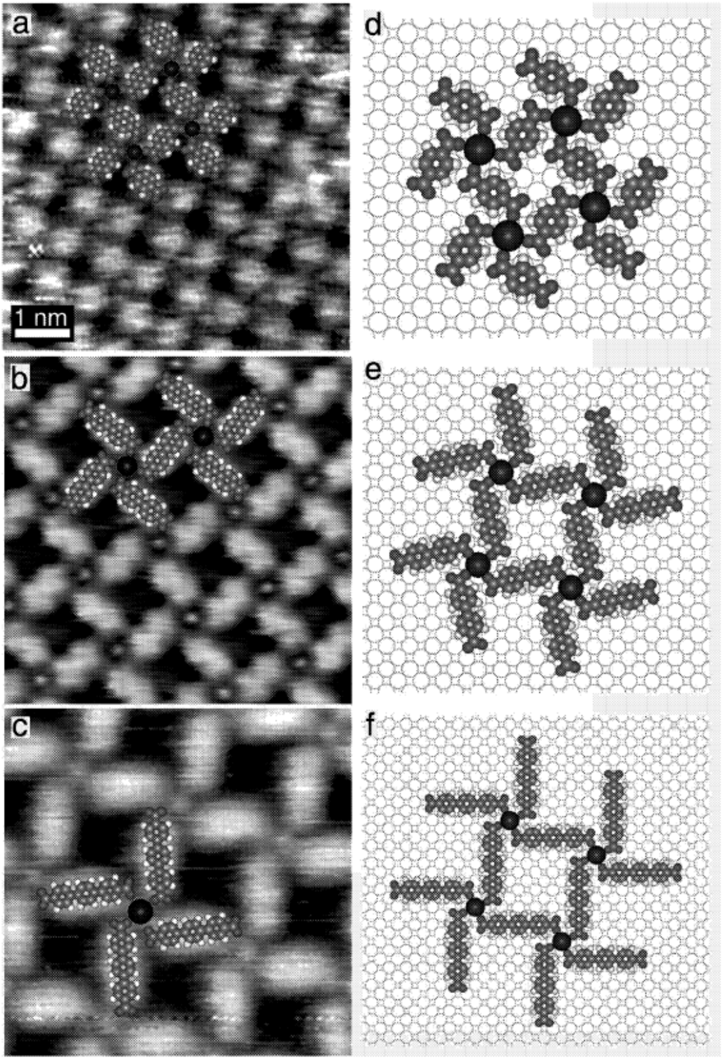

Figure 3.9: (a-c) STM topographs of (a) TPA-, (b) BDA- and (c) TDA-Cs cavity-networks. (All images with the same scale indicated in (a).) **(d-f)** Respective models of the three networks in (a-c). All constituents are assumed to reside in the same plane parallel to the surface and the Cs ions occupy the substrate hollow sites. The unit cells with respect to the copper surface are found to be [2, 4 / 4, -2], [5, 3 / 3, -5] and [7, 3 / 3, -7] in the TPA-, BDA- and TDA-networks, respectively.

addition, the partial charge transfer of the chemisorbed molecule to the surface must be taken into account, which may result in a reduced effective negative charge at the carboxylate groups. Another common feature of the cavity structures is the alignment of the linkers with respect to the central Cs ion. The molecules do not point directly to the metal atom generating a propeller arrangement, so that only one oxygen atom of the carboxylate group is in direct contact with the Cs ion. The propeller structures were also observed in various Fe–carboxylate coordination complexes assembled at surfaces [155, 189, 201]. Similar to the transition metal complexes, the Cs propellers represent two-dimensional chiral species, i.e., the four linkers are folded either clockwise or counter-clockwise at a Cs ion. The chiral information is expanded over the network domain via the linkage of propeller motifs with the same chirality, and thus resulting in homochiral domains. The symmetry of the substrate accounts for the presence of mirror structures. These mirror domains contain opposite chiral motifs as exemplified by Figure 3.10(d) for the BDA structures.

In all three cavity networks the Cs ions are arranged in a square lattice following certain substrate directions. The unit cells can be assigned to the matrix notations [2, 4 / 4, -2], [5, 3 / 3, -5] and [7, 3 / 3, -7] (and mirror orientations) with respect to the Cu(100) surface for the TPA-, BDA- and TDA-networks, respectively. Tentative models for the cavity network structures are presented in Figure 3.9(d-f). We assume that all constituents reside in the same plane parallel to the surface and that the Cs ions occupy the substrate hollow sites. As seen in the models all three structures might be stabilized by potential ionic hydrogen bonds between the carboxylate oxygen and the phenyl hydrogen atoms [215]. The formation of the well-defined structures suggests that besides the ionic binding motif the surface also plays a significant role in the self-assembly process. Due to the adsorbate-substrate coupling the molecular species and the Cs ions prefer certain adsorption configurations, e.g., specific adsorption sites or molecular orientations with respect to the substrate. Thus, the balance between the ionic interactions and the adsorbate-substrate interactions determines the overall topology. The interaction between the Cs cations and oxygen anions is strongest for the shortest distance with a lower limit given by the effective ion radii of the atoms. In addition, the molecules in the propeller shaped motif have to find the energetically best position with respect to the substrate which results in the observed network orientations. The gradually decrease in bond strength with increasing distance of the ions accounts for the flexibility of the ionic interaction, which is reflected by the occurrence of large (up to 50 nm in diameter) and almost defect free network domains. In principle the bond lengths are not restricted to a narrow range as in the case of the transition metal coordination due to the chemical nature of this bonding type.

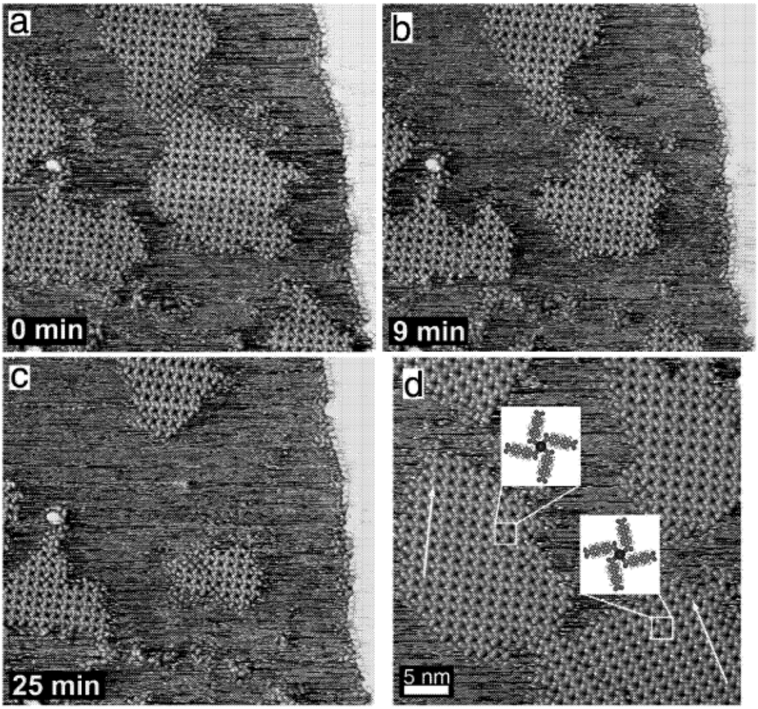

Figure 3.10: (a-c) Consecutive STM images taken at the same area of the substrate. The size of the BDA network domains shrink while scanning. **(d)** An overview of the BDA networks showing two different homochiral domains. Insets show the models of the opposite molecular folding at a Cs atom in the two domains. The arrows indicate the network orientation.

The structures are often affected while scanning. A series of STM consecutive images taken at the same area of the sample at ∼ 4 min intervals exemplify the influence exerted by the tip (three images with indicated time are represented in Figure 3.10(a-c)). The change of the network island size is ascribed at least partially to the tip influence because the domains always shrink with progressing time. This must be accompanied by a substantial mass transport at the surface which is also present during the assembly of the structures at room temperature. Moreover the fuzziness of the bare copper substrate between the network domains in the STM topographs indicates a significant amount of mobile adsorbates. Since the interaction is expected to be weaker than the transition metal coordination the network structures might be subjected to dynamic growth processes which result in the continuous alteration of the domains at room temperature. A similar mobility of the components is expected in the case of the Fe coordinated networks in Section 3.1 but the significant difference in the preparation temperature ($\sim$ 450 K instead of 300 K) signifies the simplicity of the ionic interaction. The high temperatures in the case of the transition metal networks are partially due to the prevention of unwanted bindings, such as the formation of stable metal clusters, which does not occur for alkali metals.

As mentioned above, at different Cs concentrations other phases have been observed. Images of three TPA structures with a slightly different Cs-molecule ratio are presented in Figure 3.11. All assemblies have the central propeller motif in common. Some of the carboxylate moieties do not bind to Cs ions, but form ionic hydrogen bonds with the neighboring molecules [215]. It is interesting to note that some of the structures have a much lower symmetry than the cavity structures and that the unit cell contains up to eleven TPA molecules. Despite these complicated structures the size of the domains exceeds 30 nm in diameter. Due to the small differences in the Cs-TPA ratio different structures coexist on the substrate under the same conditions. All structures found for TPA are aligned with their principal axis off the high symmetry directions of the substrate. The corresponding mirror domains have opposite chirality due to the central propeller motif in the structures. A close packed structure was also found for BDA at lower Cs concentrations (cf. Figure 3.12(a)). The chiral propeller motifs are arranged in a square lattice and they are linked via potential ionic hydrogen bonds between carboxylate groups and phenyl hydrogen atoms (see model in Figure 3.12(b)). This structure is found to grow in large long–range ordered domains with dimensions of over 50 nm. This might be also attributed to the adsorption configuration of the molecules, shown in Figure 3.12(b), which is identical to that found in the molecular phase (see Section 2.3). Apart from the two networks shown in Figure 3.9(b) and 3.12(a) no other Cs-BDA structures were observed.

The longest linker, TDA, can form another network phase, which is topologically different from the structures obtained for TPA and BDA. In Figure 3.12(c) a closely packed arrangement of TDA molecules comprising elongated voids is presented. A close inspection reveals that the local binding of the linkers to the central Cs ion is identical to the cavity phase in Figure 3.9(c). The major difference to the cavity network is the presence of both chiral propeller motifs in this structure. Furthermore the folding of the molecules at the Cs ions is opposite at adjacent network nodes resulting in the alternating arrangement of the chiral motifs, and thus a racemic phase. In Figure 3.12(d)

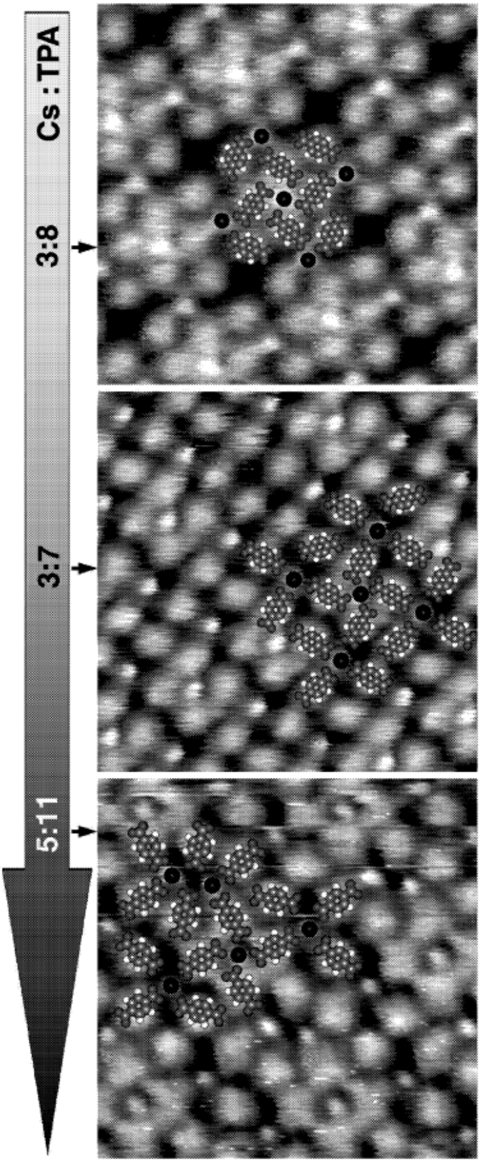

Figure 3.11: STM topographs of three Cs-TPA networks with slightly different Cs-TPA ratios. The Cs-molecule ratio in the unit cell is indicated for each structure.

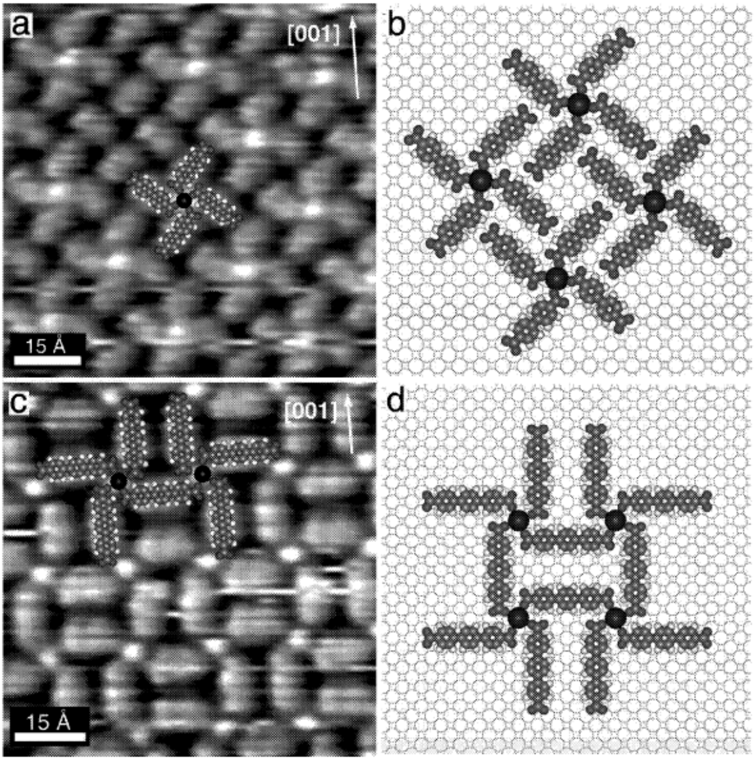

Figure 3.12: **(a)** STM image of the BDA structure with a low Cs-BDA ratio. The molecules are not continuously linked by Cs atoms. **(b)** Model of the low Cs BDA-phase shown in (a). The propeller shaped entities are linked together by potential hydrogen bonds between the carboxylate moieties and phenyl hydrogen atoms. **(c)** STM image of the TDA heterochiral network structure. **(d)** Model of the TDA heterochiral phase illustrating the alternating arrangement of Cs atoms with opposite molecular folding.

a tentative model illustrating the molecular organization of the heterochiral phase is presented. The Cs ions are arranged in a (5×5) lattice and the molecular arrangement of neighboring parallel TDA molecules generates the elongated cavities. The heterochiral phase coexist with the homochiral structures shown in Figure 3.9(c) under the same conditions which suggest that they are isomeric structures close in energy. A heterochiral phase is totally absent for TPA and BDA. We attribute this difference to the fact that the molecules prefer different adsorption sites at the surface. As seen in Figure 3.9(f) and 3.12(d) the TDA linkers align with the high-symmetry [001] or [010] substrate directions. Hence, the molecules possess the same orientation in the mirror domains. The chiral information is not mediated via the molecular orientation but rather by the alignment of the Cs ions with respect to the carboxylate moieties of the linkers. While in the homochiral phase the metal ions bind at different sides to the molecules with respect to the long axis of the TDA molecule, they are linked to the same side in the heterochiral phase. This does not involve a molecular reorientation and the different configurations yield no apparent energetic difference. In the cases of TPA and BDA, the formation of heterochiral arrangements would possibly involve changes in the molecular adsorption configuration compared to the cavity structures which might be energetically less favorable for the TPA and BDA molecules, and thus similar heterochiral phases do not occur. This interplay between the adsorbate-adsorbate and adsorbate-substrate interactions might in principle be a way to steer (chiral) molecular organizations.

The capability of relatively small molecules to form various coordination structures depending on the metal-ligand concentration ratio has been also observed in other Fe–coordination systems [5,155]. The variety of structures of the longer molecules is mostly due to structural isomerism (see Section 3.1). TPA with only one aromatic ring in the molecular backbone structure is expected to adopt more easily the best suited position and molecular orientation to achieve an effective binding to metal ions compared to the longer ligands. Hence, the diversity of coordination structures for small ligands is a direct consequence of the adsorbate-substrate interactions.

In conclusion, we have demonstrated that the ionic self-assembly can be successfully applied to construct two-dimensional network structures at a metal surface with predictable topologies. Since ionic coupling is a very flexible and simple method it represents a unique route to assemble 2D periodic nanostructures at surfaces. In particular the molecular building blocks, in this case carboxylic acids, are abundant in chemistry and can be designed for the specific needs. We believe that this technique may find general application in low-dimensional nanomaterial synthesis in future.

Chapter 4

Functional Aspects of Metal-Organic Coordination Structures

Metal-organic coordination networks (MOCNs) have attracted wide interest because they provide a novel route towards porous materials that may find applications in molecular recognition, catalysis, gas storage and separation [56, 57]. By using appropriate organic molecular linkers connecting to metal nodes it is possible to control pore size and functionality of open coordination networks [169, 174, 179, 180, 183, 216, 217]. The utilization of such structures supported at surfaces is thus of great technological interest. Single crystal surfaces were studied long time as model systems of the active part of catalysts in heterogeneous catalysis. The reactions involve that one or more reactants adsorb and diffuse on the surface. These processes include specific binding sites, conformation and transport phenomena of the molecules. The chemistry of the interface can be altered by the functionalization of the surface, i.e., the modification of the chemical composition of a surface by incorporation of selected chemical elements or functional groups. It is known that the modification of metal surfaces with molecular layers, e.g. tartaric acid [218], can create enantioselective catalysts. The coating of surfaces with 2D open void structures allows guest molecules to bind only to the substrate exposed by the cavities of the molecular layer. Since the guest species will also interact with this adlayer it can be used to steer the binding to the substrate. Thus, the binding strength and conformation of the guest molecules will be altered compared to the bare surface, which might be eventually exploited in a variety of applications.

Equally important for the functionality are the metal coordination centers of the MOCNs. Transition metal elements, e.g. vanadium, manganese, iron, cobalt, nickel, copper, zinc, molybdenum and tungsten, play a key role in biological processes. Their chemical activity is essential for the function of enzymes in all living organisms. These systems are the objectives of a tremendous amount of scientific investigations. In particular, the reaction mechanisms of the so-called heme and non-heme iron centers with dioxygen have been studied extensively [59, 60, 219, 220]. The most prominent examples are hemoglobin and cytochrome P–450. Many proteins containing iron units transport dioxygen and oxygenate a variety of substrates. The iron(II)-dioxygen reactions also mediate the controlled generation of protein and nucleic acid radicals as well as the assembly of the mineral core in the iron storage protein ferritin. In order to understand the physical properties and reactivities of the biological iron centers chemists have prepared models to mimic their structure and functions. The fabrication and study of surface supported complexes represents yet another way to mimic the active centers. This approach offers a number of advantages: the simplicity and flexibility of the fabrication and the unique possibility to study the reactions at single metal centers by scanning probe methods in real space and time. On the other hand, it introduces the presence of a surface support, which is absent in the biological proteins but may strongly influence the chemical properties of the active centers. Investigations on these systems, in particular to relate molecular structure with chemical reactivity, could ultimately result in functional mimics, which could provide an economical source of methanol as an alternative fuel or could be used in water purification and the cleanup of toxic waste.

Magnetic properties of the metal centers, strongly correlated with the electronic structure, and thus the reactivity, represents another interesting issue of these coordination systems. The research in the field of molecular magnetism is concerned with the magnetic states and ordering of molecule based magnets. In most cases bulk magnetic properties like long-range ordering are under investigation. The magnetic moments arise either from organic radicals or transition metal ions constituting the magnetic subunits, but also hybrid structures have been synthesized [65, 184]. Supramolecular magnetic materials are based on these subunits and by their controlled assembly a rich diversity of architectures and magnetic properties can be obtained (see, e.g., ref. [184] and references therein). The magnetic subunit is not or only slightly affected when it is arranged in supramolecular networks. This is an advantage of the molecular approach over the conventional magnetic systems, where the magnetic moment per atom in bulk materials considerably deviates from that of an isolated atom. Furthermore, the electronic properties of the metal atoms are altered when adsorbed on surfaces. The magnetic anisotropy energy as well as the easy axis of the magnetization is influenced by the substrate-adsorbate hybridization [221, 222]. In particular, the charge of the metal ion as well as the surrounding ligands of the metal–organic complexes is strongly affected by the metal substrate which effectively screens any unbalanced charge. On the other hand, hybridization of the metal complexes with the substrate might be an additional source of an enhanced magnetic anisotropy as well as the substrate electrons could mediate a magnetic coupling between the periodically spaced metal centers. The elucidation of these questions is thus of great scientific interest.

In this Chapter we study the functional properties of the fabricated MOCNs presented in Chapter 3. The response of the open cavity structures and iron coordination centers to the adsorption of large organic (C_{60}) and small gas (O_2) molecules is the subject of the Sections 4.1 and 4.2, respectively. Temperature-controlled STM experiments were performed to probe the bond strength of the co–adsorbed molecular species and to test the thermal stability of the oxygenated MOCNs. In Section 4.3 the magnetic properties of the TPA and BDA networks (see Section 3.1) are discussed. The XMCD measurements reported in the Section 4.3 as well as the XAS data in Section 4.2 are the result of a joint experiment with P. Gambardella, S. Clair and S. Pons from the EPF Lausanne.

4.1 Exploring Bonding Phenomena in Functionalized Nanocavities

The inclusion of guest species (ions, molecules) into tailored host systems exploiting non-covalent binding is at the origin of supramolecular chemistry [42, 223–225]. A key feature in supramolecular inclusion is that the guest components are bound to the hosts reversibly by weak interactions, such electrostatics forces, hydrogen bonding, van der Waals forces, stacking forces, or metal coordination. Surface-supported MOCNs comprising tailored pore sizes and chemical functionality provide versatile templates for the handling and organization of functional species at the nanoscale. In order to test the suitability of 2D coordination networks for host-guest interactions we performed temperature controlled adsorption experiments of C_{60} and other organic guest molecules.

C_{60} adsorption in open coordination networks

The linker molecules used for the present study are 1,4-benzenedicarboxylic acid (TPA), 1,2,4-benzenetricarboxylic acid (TMLA) and 4,1',4',1"-terphenyl-1,4"-dicarboxylic acid (TDA) as depicted in Table 1.1. In Section 3.1 and ref. [5, 7, 155] the 2D iron coordination structures on Cu(100) of these linker molecules are described in detail. The structures comprise nanometer-size cavities exposing the Cu surface with specific topology and chemical functionality. They represent two-dimensional (2D) analogues to previously described 3D porous metal-organic framework structures [174, 180]. The different backbone length (~ 7 Å for TPA and TMLA; ~ 15 Å for TDA) controls the cavity dimensions, whereas the additional side group of TMLA bestows a specific chemical functionality to the cavities. Earlier investigations revealed that TMLA and Fe assemble in MOCNs of almost identical topology as Fe-TPA MOCNs [5], which implies that the side groups at the ortho position of the TMLA molecules do not participate in the network formation. Instead, they modify the chemical properties of the pores, that is, the nanocavities of Fe-TPA MOCNs are enclosed by non-polar aromatic rings, whereas the rims of Fe-TMLA MOCNs comprise a highly reactive moiety. The 2D MOCNs of the TDA molecule can be regarded as a higher analogue to the networks obtained with TPA or TMLA. The large cavities reflect the increased length of the linker molecule. In the Fe-TPA and Fe-TMLA MOCNs the cavities are of the dimension of a small molecule (for example, ~ 5 Å $\times$ 5 Å for the type-C phase) while the Fe-TDA MOCNs provide large rectangular cavities extending to the nanometer range (~ 20 Å $\times$ 15 Å). The present approach therefore provides an elegant means to deliberately divide up a surface at the molecular scale [5, 12]. As the chemical properties of the cavities are furthermore expected to depend on both the linker molecules (aromatic backbones and side groups) and node atoms, they can be regarded as nanoscale hosts providing a well-defined local chemical environment.

The simplest way to test the suitability of the engineered 2D MOCNs for organization of functional materials and host-guest chemistry is to study their structural stability and steering effects in the coadsorption of nanoscale objects. As a trial species, C_{60} molecules were chosen, which can be easily brought to the surface. Controlling C_{60}–surface interactions and positioning is of both scientific and technological interest [12,226]. The C_{60} molecules were deposited by OMBE ($T_{\mathrm{sub}} = 680...710$ K) onto the nanostructured surface held at 300 K. The STM images in Fig. 4.1 demonstrate that the cavities of the Fe-TPA MOCNs indeed can accommodate single C_{60} molecules. On the MOCN-modified surface shown in Fig. 4.1(a) (left image), well-ordered ladder-type networks exist offering two types of elongated cavities (labeled A and B respectively). It is evident that exclusively C_{60} monomers are bound in the offered MOCN host sites, revealing that the MOCN Fe centers cannot effectively bind C_{60}. Moreover, the guests preferentially reside in the larger B-type cavity, and frequently, strings of C_{60} are encountered following the skeleton provided by the ladder-type structure. The smaller type-A cavities cannot hold C_{60} at the given temperature (300 K). This behavior is associated

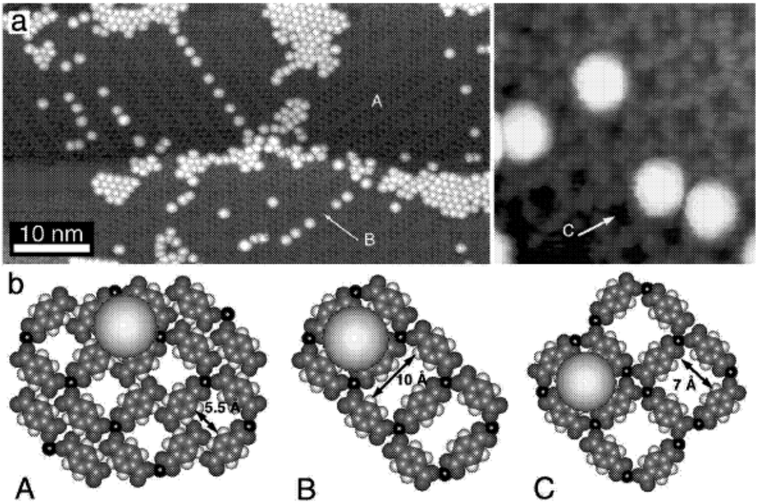

Figure 4.1: Adsorption of single C_{60} in Fe-TPA host networks. **(a)** As seen in the left STM image, ladder-type MOCN account for linear arrangements of single C_{60} (white spheres) with preferential occupation of larger cavities available (C_{60} clusters are on areas with bare Cu substrate). The right image shows C_{60}-monomer accommodation in cavities of type-C network. **(b)** Top-view models for C_{60} adsorption in the cavities encountered in (a) with molecules drawn to scale. Possible configurations are labeled in the model and data by A,B and C. In the van der Waals geometries used for modelling, the molecules appear smaller than in the STM images.

with the fact that in the larger cavities the fullerenes can interact more effectively with the Cu substrate. The corresponding models shown in Fig. 4.1(b) demonstrate that the smaller type-A cavity provides only limited space for C_{60} uptake, whereas the rectangular B cavity is sterically better suited as a host. Type-C Fe-TPA MOCNs cavities may be similarly used to host single C_{60} and keep them apart, as demonstrated by the STM image and the corresponding model in Fig. 4.1(a) (right image) and Fig. 4.1(b), respectively. In contrast, on the bare Cu surface, cf. left part of the STM image in Fig. 4.1(a), the fullerenes form clusters with hexagonal local order, reflecting effective attractive lateral interfullerene interactions [227].

The STM image in Fig. 4.2(a) reveals that C_{60} molecules can also be accommodated in Fe-TMLA MOCNs without altering the network topology. Again, only individual

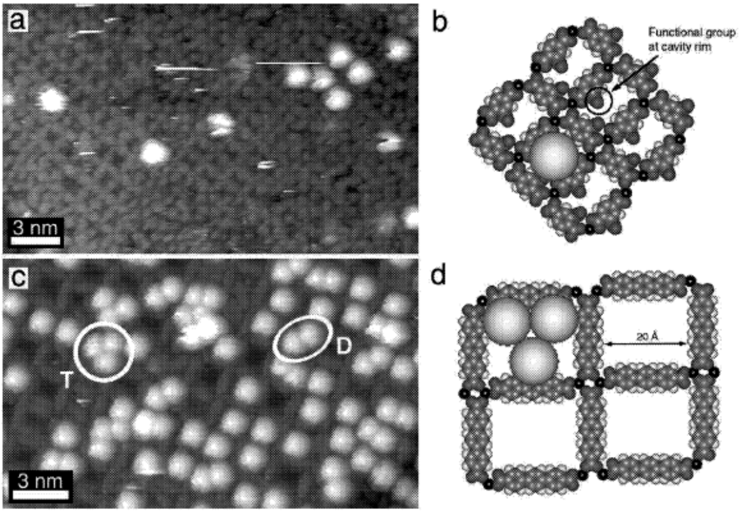

Figure 4.2: Adsorption of C_{60} in Fe-TMLA and Fe-TDA network hosts. **(a)** Similar to the Fe-TPA networks, Fe-TMLA networks host C_{60} monomers. **(b)** Model of accommodation of a C_{60} monomer in Fe-TMLA MOCN cavities. The indicated functional side group at the ortho position, which is supposed to be rotated by 90° out of the molecular plane to avoid too small oxygen-to-oxygen distances, strongly affects the chemical reactivity of the cavity. **(c)** The mesoscale cavities in 2D reticulated Fe-TDA networks can host C_{60} monomers, dimers (D) or trimers (T). **(d)** Model of rectangular Fe–TDA cavity and accommodation of a C_{60} trimer.

C_{60} monomers are found accommodated in the cavities (a tentative model is given in Fig. 4.2(b)), hence the presence of the reactive side groups in the cavities does not alter the adsorption sites. In contrast, with the mesoscale Fe-TDA MOCN cavities, the available Cu substrate patches are significantly larger than the space occupied by a single C_{60} molecule at the (100) surface. The coadsorption experiments with Fe-TDA networks demonstrate that they remain intact on C_{60} exposure, and thus can be used as a host system. An example is given by the STM image depicted in Fig. 4.2(c), which reveals that single cavities typically host monomers, dimers or trimers of C_{60}. The corresponding model (Fig. 4.2(d)) demonstrates that with the accommodation of a C_{60} trimer, most of the available space provided by the cavity is occupied. Accordingly, tetramers were only very rarely observed.

A crucial property of the systems described here is the reversibility and strength of the C_{60}–cavity interactions. Whereas adsorbed C_{60} molecules bond strongly to the pristine Cu(100) substrate and drive the formation of surface reconstructions [227], we may use the tailored MOCNs to control the C_{60}-substrate coupling. Moreover, the robustness of the networks used suggests that the guests may be even released by thermal activation or other processes. To gain insight into this issue, we probed the thermal ejection of C_{60} hosts, by warming up the system for a time interval of 10 minutes at the indicated temperature. It was found that C_{60} molecules are ejected from the Fe-TPA cavities when a threshold temperature of 370 K is exceeded. STM measurements taken after annealing revealed that C_{60} molecules have disappeared from the cavities and aggregate in clusters on bare Cu patches where no networks interfere. It is known that the desorption of C_{60} from bare Cu surfaces occurs at significantly higher temperatures (730 K for the case of Cu(110)) [228]. The significantly lower temperature detected for the cavity release signals that the C_{60} molecules in the MOCNs interact only weakly with the Cu substrate and the cavity rims. This is associated with the rigidity of the nanopores and the inert chemical nature of the phenyl rings. The corresponding space limitations result in a small contact area and hence a weaker coupling between C_{60} and Cu surface atoms. In contrast, the cavities of the Fe-TDA MOCN are considerably larger than the space occupied by a single C_{60} molecule. Thus C_{60} should be able to bind to the Cu surface more strongly, coming closer to the situation of adsorption at the pristine surface. Indeed, we found that the threshold temperature to release C_{60} adsorbed in Fe-TDA cavities must exceed 500 K, the highest temperature explored in our experiments (MOCNs become unstable for $T > 500$ K).

There is no release of C_{60} molecules from both types of Fe-TMLA cavities up to temperatures as high as 420 K, implying that the host-guest interaction is enhanced here despite the similar host size with regard to the same type of Fe–TPA MOCN cavities. As the C_{60}-Cu gap is similar in both cases, contributions from the C_{60}-substrate interaction are expected to be comparable. The increased bonding strength thus indicates that the additional side group at the TMLA ortho position strongly modifies the chemical properties of the nanocavities. As suggested in Fig. 4.2(b), the cavity rim interferes in the host-guest interactions (we presume that in the course of network formation this group is deprotonated by the reactive Fe adatoms, so that a carboxylate exists). The enhanced accommodation energy is associated with a local contribution from the reactive group at the MOCN rims, which interacts more strongly with C_{60} molecules than the aromatic ring in the case of TPA. The substantial C_{60}-rim interaction strength is further supported by manipulation experiments. Manipulation of individual C_{60} molecules with the STM tip often results in local network disintegration in the case of Fe–TMLA networks,

MOCN type	T_{eject} (K)	Dominant host-guest interaction
TPA (A)	< 300	Aromatic ring-to-C_{60}
TPA (B, C)	370	Cu-to-C_{60} (loose-contact)
TMLA	Destructive	Functionalized rim-to-C_{60}
TDA	> 500	Cu-to-C_{60} (close-contact)
Cu(110)	730	Cu-to-C_{60} (close-contact)

Table 4.1: Threshold temperatures for C_{60} ejection from different MOCN cavities; dominating hostguest interactions expected from modeling for each case are listed.

whereas Fe-TPA networks remain intact after undergoing the same operation. Heating up to 450 K leads also to a disintegration of the Fe-TMLA network architecture, that is, the uptake of C_{60} in Fe–TMLA nanocavities is irreversible, which again is associated with the enhanced local reactivity in the vicinity of the molecular side group.

Table 4.1 summarizes the threshold temperatures for the release of C_{60} guest molecules from the respective surface–supported MOCN cavities. The dominating host-guest interactions for each case, from weak C_{60}-phenyl coupling to strong C_{60}-Cu binding, are indicated. In conclusion, our findings demonstrate that surface–supported Fe–carboxylate MOCNs with controlled pore size and functionality represent robust templates for the handling and organization of functional species at the nanoscale. In particular, we demonstrated their aptitude to accommodate C_{60} molecules, whereby the corresponding host-guest interactions can be steered by constructing MOCN architectures with specific topology and functionalized rims. This tuning of the lateral and adsorbate-substrate interactions of included guests is particularly important for selective adsorption or surface chemical reactions. Generally speaking, however, engineering MOCNs at surfaces is expected to provide a versatile rationale towards the fabrication of novel patterned layered materials and templates for positioning nanoscale objects, which may comprise functionalities of interest in a great variety of fields, such as sensing, heterogenous catalysis, molecular electronics or magnetism.

Binding of organic species in 2D metallosupramolecular receptor arrays

Similar to the behavior encountered in biological systems, as exemplified by the exclusive coupling of enzymes to their substrates, supramolecular receptors exhibit selectivity, i.e., only guests with specific geometric (steric) and electronic properties are accommodated in appropriate hosts. Following this so-called key and lock or molecular recognition principle, the design of supramolecular systems with controlled host-guest interactions has become an extensively pursued goal [41]. A classical example is molecular recognition in the binding between crown ethers and alkali ions [229]. Such systems also nicely illustrate the concept of cooperativity: Albeit the binding forces between alkali metals to a single binding site are weak, the cumulative effect of organized multiple binding sites accounts for appreciable and selective host-guest interactions.

In the last decades much attention has been focused on self-assembly of molecular receptors containing a cavity, such as cyclodextrins and calix[n]resorinarenes, at liquid-solid interfaces [230–237]. Monolayers of these molecules are able to recognize and bind specific guest species via supramolecular interactions. Recently several examples have shown that supramolecular systems with open voids can be fabricated from self-assembly of simple molecular components at liquid-solid or vacuum-solid interfaces, which represent model systems to study supramolecular inclusion phenomena [12, 136, 156, 238, 239]. In particular, such model systems are addressable by scanning tunneling microscopy (STM). Because STM is capable of resolving real–space structures at the molecular level, detailed structural information, e.g., actual binding sites or configurations of the bonded guests can be obtained. In particular, STM revealed directly that nanocavities in two-dimensional porous supramolecular layers are able to accommodate C_{60} or other molecules as guests [12, 140, 156, 240]. Furthermore, such observations allow to address the dependency of guest-host interactions on the shape and chemical nature of the nanocavities [156]. Here we report a systematic STM investigation on the use of metallosupramolecular nanocavity arrays as receptors that reversibly host various organic molecules. High–resolution data provide detailed structural information on the accommodation. The reversibility of the host-guest interactions is demonstrated by annealing experiments. Because the receptors are arranged in a square lattice with 3.4-nm periodicity which dictates the spatial organization of the guest species, a template is at hand to fabricate two-dimensional molecular nanoarrays.

The STM image reproduced in Fig. 4.3 depicts the nanoporous metallosupramolecular arrays employed in this study, which are obtained on a Cu(100) substrate by hierarchical self–assembly of Fe atoms and trimesic acid (TMA, cf. Table 1.1) molecules. Preparation procedure and structural evolution have been detailed in previous publications [7, 189]. The dark areas in the STM topograph represent the nanocavities, which comprise square-lattice arrays with a 3.4 nm periodicity. The cavity domains cover almost the entire surface when proper preparation parameters are used, i.e., the Cu substrate atoms are only exposed in the nanocavities or at domain boundaries, while otherwise the surface is covered by the metal-organic adlayer. The nanocavities are thermally stable for temperatures as high as 500 K. The inset in

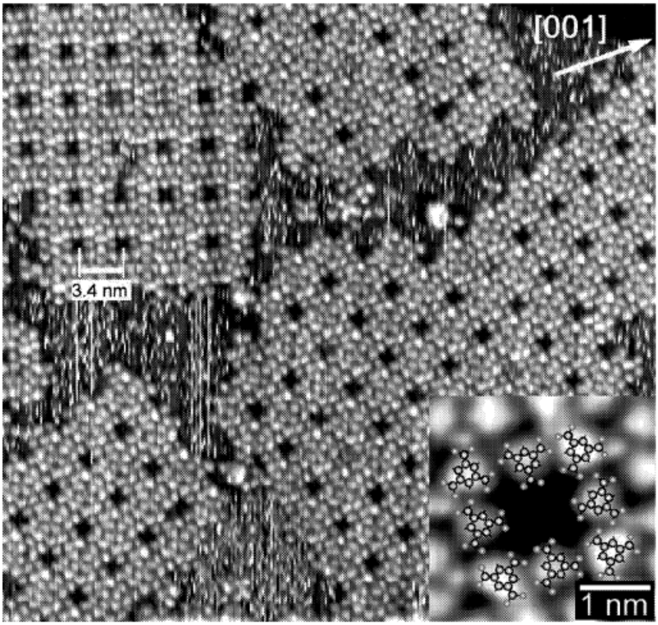

Figure 4.3: Arrays of two-dimensional metallosupramolecular nanocavities fabricated on the square Cu(100) substrate by hierarchical assembly of trimesic acid molecules and Fe atoms. The tentative model in the inset shows a single nanocavity surrounded by eight uncoordinated carboxylate groups.

Fig. 4.3 demonstrates that the nanocavities have a broad-branch X-shape with an opening of 1 nm. Each nanocavity is surrounded by eight TMA molecules. Because the apex of a TMA molecule carries an unsaturated carboxylate group [7, 149, 189], the nanocavities are decorated by a total of eight reactive ligands (cf. model in the inset of Fig. 4.3). The geometry and chemistry of the nanocavities resembles that of crown ethers. Thus this structure represents a model system to study host-guest interactions.

As exemplary guest species we employed the biomolecules cystine (LL enantiomer) and LL-phenylalanine (Phe) dipeptide, as well as the fullerene C_{60} (cf. Figure 4.4). Small doses of these molecules were deposited on the nanocavity-covered substrate by thermal sublimation under ultra-high vacuum conditions (temperatures employed were 413 K (cystine), 445 K (Phe-dipeptide), and 690 K (C_{60}), respectively). The temperature of the substrate supporting the nanocavities was kept at 300 K during the molecular

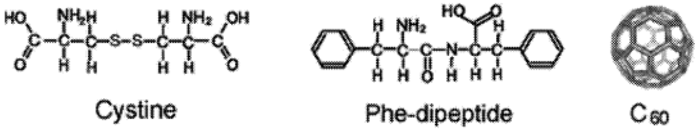

Figure 4.4: Guest molecules used with the Fe-carboxalyte receptor arrays.

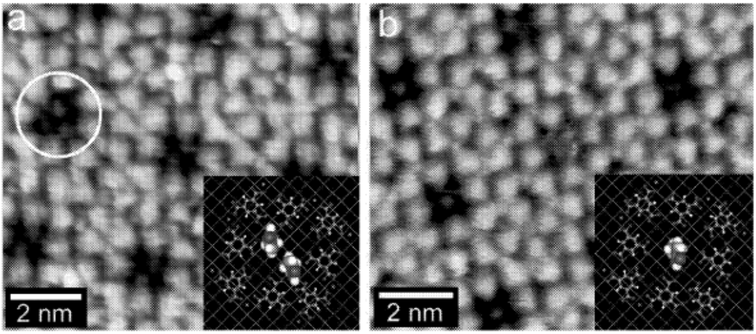

Figure 4.5: Accommodation of cystine molecules in the Fe–carboxylate receptor network. **(a)** Following deposition at 300 K, cavities with two–protrusion features are associated with two cystine molecules anchored on the Cu substrate in an upright configuration. A nanocavity comprising even three cystine molecules is marked with a white circle. **(b)** Upon 430 K annealing, the nanocavities typically accommodate a single cystine guest at their centers. Insets illustrate tentative models of the guest adsorption configuration.

beam exposure. The STM measurements were conducted subsequently in situ at room temperature using the same apparatus.

In Fig. 4.5(a) an STM topograph of the nanocavities following exposure to cystine is reproduced. While the network topology and appearance remains unaffected, at the interior of most nanocavities two protrusions are resolved. These features are exclusively observed upon cystine deposition, and moreover their number increases monotonically with the cystine dosage. Hence they are associated with cystine molecules decorating preferentially the nanocavities. The two–protrusion feature could represent either a single cystine molecule coupled with both carboxylic groups to the residual Cu surface (flat-lying adsorption) or to a pair of cystine molecules adsorbed with their long axis perpendicular to the surface (up–right standing adsorption). However, because some of the nanocavities include three protrusions, (as marked by the cycle in Fig. 4.5(a)), the flat-lying scenario is excluded, whence each protrusion is associated with a single cystine adsorbed in an up–right configuration. Due to lack of spectroscopic information the binding configuration cannot be fully characterized. Nevertheless, the up–right adsorption suggests that the cystines bind to the surface via their carboxylic endgroups, whereby presumably a carboxylate is formed (cf. inset in Fig. 4.5(a)). This binding scheme is frequently encountered in the adsorption of carboxylic acids on copper or other surfaces and has been extensively studied [16, 143, 144, 147, 149, 241]. Both symmetric bidentate and asymmetric monodentate bonding were reported depending on the adsorbates' coverage [16, 143, 144, 147, 149, 241]. For the long–chain molecules with a chain length comparable to cystine the orientation of the chain prefers to align with surface normal or slightly tilted off the surface normal [144, 147], which corroborates our interpretation. A close inspection of Fig. 4.5(a) moreover reveals that in the nanocavities the two molecules always reside at two opposite diagonal positions, suggesting that the surrounding carboxylate groups at the rim of the nanocavity imposes steric confinement to the cystine guests. The influence of the nanocavity rim to the cystine binding is discussed in further detail below.

The cystine molecules adsorbed in the nanocavities can be removed by thermal annealing. The removal is a progressive process: at 430 K one cystine is released and the second one remained but shifted to the center of the nanocavity, as shown in Fig. 4.5(b). Upon further increasing the temperature to 490 K also the remaining molecule is released and most of the nanocavities are empty. The temperature difference and the shifting of the single cystine to the nanocavity center indicate that the intermolecular cystine interactions and those with the nanocavity rim are repulsive rather than attractive. Furthermore the two–step releasing process reveals that the accommodation energy is slightly larger when only single cystines are trapped in the nanocavities. These processes are completely reversibly - after the guest removal the empty cavities present their original structure.

The accommodation of the larger and more complex Phe-dipeptide biomolecules is demonstrated by the STM image in Fig. 4.6(b), where a decoration of all nanocavities is clearly resolved. Considering the length of this species (~ 1.3 nm) with the terminating unreactive bulky phenyl rings at both ends, steric hindrance prevents from the inclusion of the complete molecule in a nanocavity. As revealed in Fig. 4.6(b), the imaged appearance of the hosted Phe-dipeptide molecules is not well defined, i.e., they appear as irregular frizzled objects. This is associated with a partial accommodation of the Phe-dipeptide which allows for the flexible molecules to undergo conformational

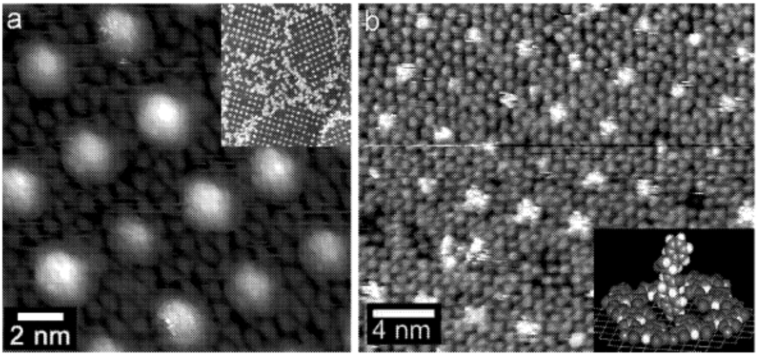

Figure 4.6: Nanoarrays of biomolecules and fullerenes. **(a)** The flexible molecule Phe-phe dipeptide is imaged as frizzy protrusion, which is associated with molecular conformational changes during the STM imaging process. The model in the inset shows the suggested upright adsorption configuration. **(b)** Single C_{60} molecules included in the nanocavities, the different inner structure reflects distinct adsorption configurations. Inset: mesosopic organization of C_{60} array domains.

changes possibly provoked by the interaction with the tip, producing the unstable STM features. Moreover, the dimension of the Phe-dipeptide molecules is compatible with an uptake of exclusively single molecules in the nanocavities. As a consequence, a well–ordered single–molecule nanoarray Phe-dipeptide species evolves.

The STM data in Fig. 4.6(a) demonstrates the accommodation of the fullerene C_{60} in the nanocavities. Clearly each nanocavity hosts a single C_{60} molecule, which reflects the nanometer size of C_{60}, whose van der Waals diameter of 1 nm fits well to the nanocavity void (note that the apparent size of the C_{60} molecules is magnified by imaging effects). The apparent height of the adsorbed C_{60} molecules is not a constant for different molecules, which is understood as a result from C_{60} molecules in different adsorption configurations, with specific orientation or positioning. Moreover the STM data suggest that the C_{60} molecules are fixed in the cavities, because their apparent height remains unchanged. The C_{60} molecules are preferentially occupying the nanocavities, i.e., at the metal–organic adlayer no adsorption occurs. For higher doses when almost all the nanocavity sites are occupied the surplus C_{60} molecules accumulate at the boundaries of the nanocavity domains (cf. the inset of Fig. 4.6(a)). Thus the nanocavity arrays can be used as a template to assemble square lattices of individual C_{60} molecules at the surface.

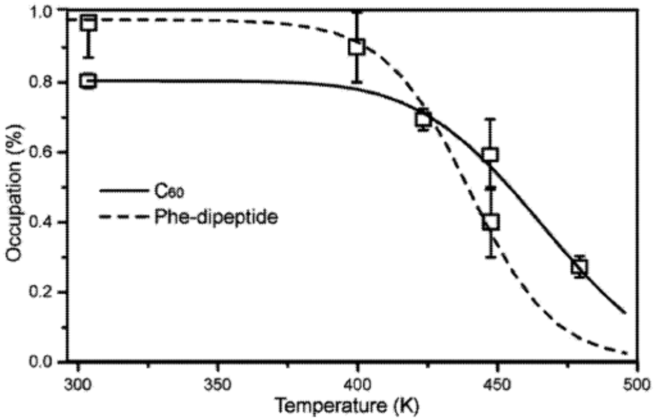

Figure 4.7: Thermal release of C_{60} and Phe-phe dipeptide guests from Fe-trimesate receptors as monitored in annealing experiments. For temperatures exceeding 400 K appreciable release occurs. C_{60} molecules are more strongly bound to the hosts than the dipeptide species. The curves are drawn as a guide for eyes.

In order to estimate the strength of the host–guest interactions, step–wise annealing experiments were performed, i.e., the samples with guest species (Phe-dipeptide, C_{60}) accommodated in the nanocavities were annealed to a desired temperature (for a duration of 5 minutes) and then cooled down to 300 K for STM observations. From a detailed analysis of molecular–level data we could directly obtain the guest concentration remaining after each annealing cycle and verify the characteristics of the emptied nanocavities. The respective results are summarized in the diagram in Fig. 4.7. With both guest species significant release is encountered for temperatures exceeding $\sim$ 400 K. A careful inspection of STM data reveals that guest release does not strictly correlate with thermal desorption into the gas phase, rather we observed, notably evident for the case of C_{60}, a significant accumulation of the released species at the domain boundaries of the metal-organic adlayer. I.e., while the cavity accommodation is clearly reversible leaving the hosts unchanged, and the thermal release reflects system-specific host-guest interactions, they cannot be unambiguously quantified by standard thermal desorption theorems.

The C_{60} guests show the strongest coupling to the nanocavities. However, their release occurs at temperatures significantly lower than those required for desorption of

C_{60} from clean Cu surfaces (730 K in the case of Cu(110) [228]). This is associated with the spatial confinement of C_{60} molecules at the nanocavities, whose 1 nm pore diameter prevents from strong interactions with the Cu substrate atoms as occurring in the interaction of C_{60} with pristine Cu(100) [227]. Presumbly the nanocavity rim binds to the C_{60} through the carboxylate functions via donor–acceptor interaction [156, 242]. After the thermal releasing the nanocavities remain unchanged, confirming the reversibility of the host–guest interactions. This is in contrast to previous studies, where the thermal removal of the C_{60} guests from the Fe-trimellate nanocavities, with reactive carboxylate groups at cavity rims, went along with the destruction of the nanocavities [156]. For the latter case the nanocavities are defined by the backbones of single molecules spanning up the coordination networks, whereas in the present case the nanocavities are embedded in a more complex and rigid metal–organic matrix, which accounts for higher stability. Compared to the case of C_{60} the Phe-dipeptide guests are released at lower temperatures, which reflects weaker binding forces. Because both ends of the Phe-dipeptide molecule are phenyl rings, the host–guest interaction is attributed to the hydrogen bonds between the phenyl rings and the carboxylate groups at the nanocavity rim.

In conclusion, we have investigated supramolecular host–guest inclusion phenomena at the single–molecule level. Our STM observations on Fe–carboxylate receptor arrays reveal that engineering two–dimensional metallosupramolecular systems at surfaces opens up new vistas for the control of functional molecular species. Many important aspects can be addressed in great detail, notably binding sites and configurations. We also have demonstrated that the accommodation of cystine, C_{60} and Phe–dipeptide molecules at the hosts is completely reversible, as evidenced by thermal removal of the respective guest species. Distinct behavior was found for each system, exemplifying the selectivity of the host–guest interaction. Last but not least the supramolecular nanocavity arrays represent templates to achieve patterns of functional molecules in regular two–dimensional superlattices.

4.2 Oxygen Adsorption on Mono- and Dinuclear Fe Coordination Centers

In this Section we study the structural and chemical modification of the TPA and BDA coordination structures supported at a Cu(100) surface (see Section 3.1 and ref. [155]) upon exposure to dioxygen molecules. Oxygen gas (99.998% purity) was dosed into the vacuum chamber at partial pressures between $3\times10^{-9}\ldots3\times10^{-8}$ mbar for up to 45 min (corresponding to dosages of a few tens of L, where 1 L = 1 Langmuir) and substrate temperatures in the range from 140 K to 400 K. STM experiments were performed at room temperature to reveal the geometrical rearrangement of the structures. The electronic state of the Fe atoms is characterized by Fe L-edge x-ray absorption measurements. All investigated structures comprising mono- and dinuclear iron centers show pronounced differences at the iron atoms in the STM images after oxygen dosing. This adsorption is accompanied by a significantly reduced thermal stability of the structures which leads in the case of the TPA diiron structures (cf. Section 3.1) to a destruction of the phase below room temperature. Marked changes has been also found in the Fe L-edge XAS data after oxygen adsorption, which is associated with the chemisorption of the gas molecule and the potential cleavage of the dioxygen bond by the dinuclear Fe units.

STM images of the oxygenated structures are shown in Figure 4.8(a-d) (see also Section 3.1 and ref. [155]). The TPA flower (Fig. 4.8(a)) and TPA double row (Fig. 4.8(b)) structures contain mononuclear iron centers coordinated by four carboxylate oxygen atoms in a slightly distorted square planar geometry [155]. TPA single row phase and BDA network, presented in Figures 4.8(c) and (d), respectively, consist of dinuclear Fe complexes. The structures differ mainly in the Fe-Fe spacing ($\sim$ 4.7 Å for TPA and $\sim$ 3.8 Å for the BDA structures, cf. Section 3.1). In addition, the Fe coordination environment is square planar for the TPA network and in the case of the BDA structures it is expected to be trigonal planar or tetrahedral (cf. Section 3.1). As shown in Figure 4.8(a,b,d) the iron centers with adsorbed oxygen appear altered in the STM topographs compared to unaffected coordination centers. Depending on the tip the oxygenated Fe atoms are usually imaged as dark spots. The altered centers can be unambiguously related to adsorbed oxygen molecules as the number of dim iron atoms increases with higher oxygen dosage (cf. the consecutive STM images in Figure 4.9). Once the oxygen is adsorbed the iron atom remains dark, i.e., no desorption has been observed under the experimental conditions. While the structures of the mononuclear TPA phases and the BDA network is preserved upon oxygen dosing at room temperature (tested for dosage of at least 100 L) the TPA diiron structures readily change its morphology at already low dosages. At about 25 L the initially well-ordered TPA single rows are essentially destroyed, i.e., the TPA molecules change their positions and form a disordered phase consisting of different iron complexes. Figure 4.8(c) shows an often observed configuration of dinuclear metal centers surrounded by four TPA molecules. Compared to the TPA diiron structure presented in Section 3.1 the bridging ligands remain in their position but the axial ligands are shifted upwards and downwards with

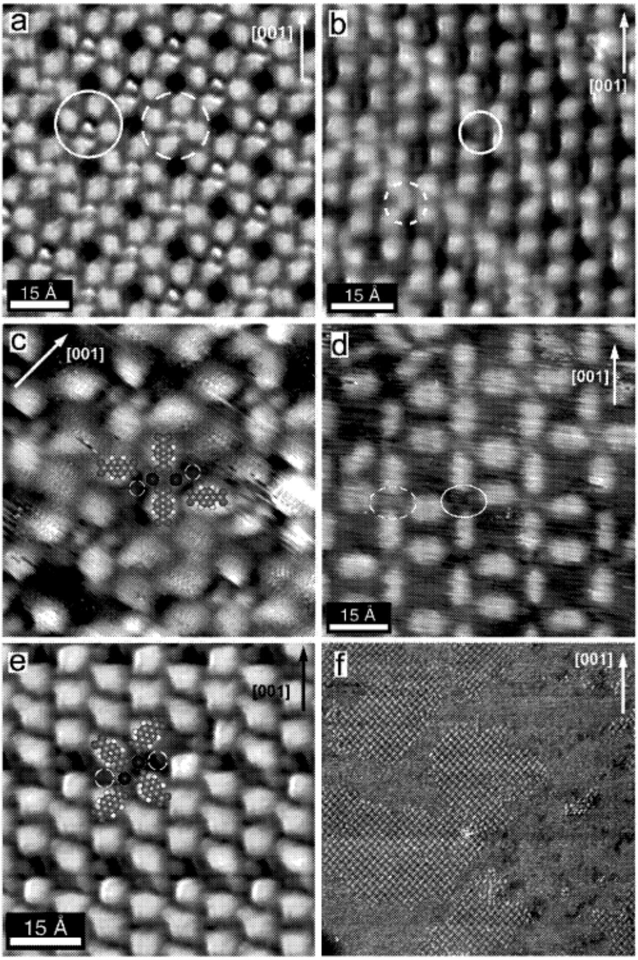

Figure 4.8: **(a-d)** STM images of the oxygenated phases of (a) TPA flowers, (b) TPA double rows, (c) TPA diiron network and (d) BDA network. O_2 dosing and scanning were performed at room temperature. The iron centers with adsorbed oxygen molecules appear darker ((a,b,d) circles) compared to the unaltered centers ((a,b,d) dashed circles). In the case of the TPA diiron network the structure is not preserved. The dashed circles in (c,e) indicate a hole appearing after molecule rearrangement and annealing, respectively. **(e-f)** Oxygenated TPA phases (e) and BDA networks (f) after annealing at 450 K and 340 K, respectively. While all oxidized TPA structures result in a similar coordination structure after annealing the BDA forms only the molecular phase.

respect to the iron dimer axis leaving two dark holes next to the iron atoms (indicated by circles in Figure 4.8(c)). As suggested by the model in Figure 4.8(c) the former chelating bonding of the axial ligands has been changed to a monodentate configuration, where the second carboxylate oxygen atom can potentially form a hydrogen bond to the phenyl hydrogen of the bridging ligand.

In the case of the BDA network the adsorption of molecular oxygen also affects the iron centers, as can be seen in Figure 4.8(d), but no structural rearrangement occurs at room temperature. Nevertheless, the thermal stability of the oxygenated phase is considerably reduced. While the pristine network is stable at temperatures up to 500 K, the oxidized structures collapse at ≈ 340 K. Annealing the oxygenated phase above this temperature results in the formation of the BDA molecular phase, as shown in Figure 4.8(f). The oxygenated monoiron TPA structures, flower phase and double rows, undergo a structural transition at about 430 K and 380 K, respectively. This transition to a disordered phase can be also induced by the tip while scanning over the oxidized structures. However, we could not determine any conclusive voltage and time dependence for this process. Upon annealing the disordered oxidized TPA phases at 450 K a new structure evolves, presented in Figure 4.8(e). This phase is characterized by diiron coordination centers where the axial ligands are similarly shifted as in the case of the oxidized single rows (cf. models in Figure 4.8(c) and (e)). A hole is located next to each iron atom, marked by the circles in Figure 4.8(e), which is presumably occupied by the oxygen atom of the FeO species. Besides the TPA molecules involved in the metal coordination there exist also molecules which are only connected to their neighbors by hydrogen bonds. Hence, the structure is not strictly periodic because the width of the bright molecular stripes in Figure 4.8(e) can vary. We also examined the reactivity to dioxygen of this phase but no structural modification has been observed.

The post–annealing phase, shown in Figure 4.8(e), is also formed in the case of the oxygenated TPA monoiron structures upon warming up to 450 K. This suggests that the adsorbed oxygen also undergo a chemical reaction with the single Fe centers at elevated temperatures which is accompanied by a structural rearrangement. Differences in the thermal stability of the respective oxygenated structure can be related to the chemical reactivity of the metal centers, i.e., the diiron compounds are more unstable than the single iron complexes. Furthermore, the significant difference in the decomposition temperatures between the TPA flower (430 K) and double row ($\sim$380 K) phase might be also a result of the different number of stabilizing hydrogen bonds in the structures.

In order to follow the time dependence of the adsorption and reaction process of the O_2 molecules with the diiron coordination centers of the TPA and BDA networks, we acquired a series of consecutive STM images of the same area covered with the respective network structure. In Figure 4.9 four images for each structure are presented ((a) TPA network, (b) BDA network). The areas were scanned in 5 min intervals and the acquisition of one image took $\sim$ 4.5 min. For each image the time after the beginning of the oxygen dosing ($P_{O_2} \approx 5 \times 10^{-9}$ mbar) is given. The initially bright diiron centers of the TPA network become darker upon exposure to oxygen (cf. the dashed and solid ellipses in Figure 4.9(a)). Hence, the destabilized axial ligands change their positions or even detach from the structure, as indicated by the arrows in Figure 4.9(a). This structural relaxation is more likely if two adjacent iron centers are affected by the oxygen. The structure collapses with progressing time and dosage. The complex highlighted by the double ellipse in Figure 4.9(a) detaches because of the oxygen induced destabilization of an adjacent node and, eventually, it moves away from the island. Although in this particular case the tip might enhance the removal of the axial ligands the destabilization and geometrical changes are due to the reaction of the iron atoms with oxygen molecules.

In contrast to the TPA network the BDA diiron structure does not show such structural changes. In Figure 4.9(b) we can identify three different network nodes. The unaffected coordination centers (dashed ellipses) become first dim after oxygen adsorption (solid ellipses). After a while they turn into dark nodes, marked by the double ellipses, consisting of two well-resolved round features. In the STM topograph at the bottom of Figure 4.9(b) there exist three BDA linkers with both ends connecting to modified Fe nodes but no apparent geometrical deviation is observed.

Figure 4.10 shows the total XAS spectra ($\mu^+ + \mu^-$) of the pristine and oxygenated networks and the XAS data of a comparable amount (0.025 ML) of Fe deposited on clean Cu(100) at 400 K. The employed oxygen dosage for the XAS experiments amounts to 200 L and 100 L for the mono- and diiron structures, respectively. Compared to the Fe/Cu(100) XAS the networks possess narrower spectral features and a pronounced multiplet structure signifying that strong coordination bonds exist between the central Fe atoms and the carboxylate ligands. The ligand field imposed by the surrounding carboxylate groups significantly affects the configuration of the Fe electronic states. Although the network structures possess different coordination environments, the XAS spectra reveal similar features marked by the downward pointing arrows at the spectra for the TPA flowers in Figure 4.10. This phase shows the most pronounced features compared to the other structures. The XAS data of the diiron structures is expected to be a linear combination of Fe centers with slightly different electronic configurations due to the existence of isomeric structures. Notably, the XAS data of the flower complex resembles the absorption spectrum of an oxygen–bridged Fe(II) complex with D_{4h}

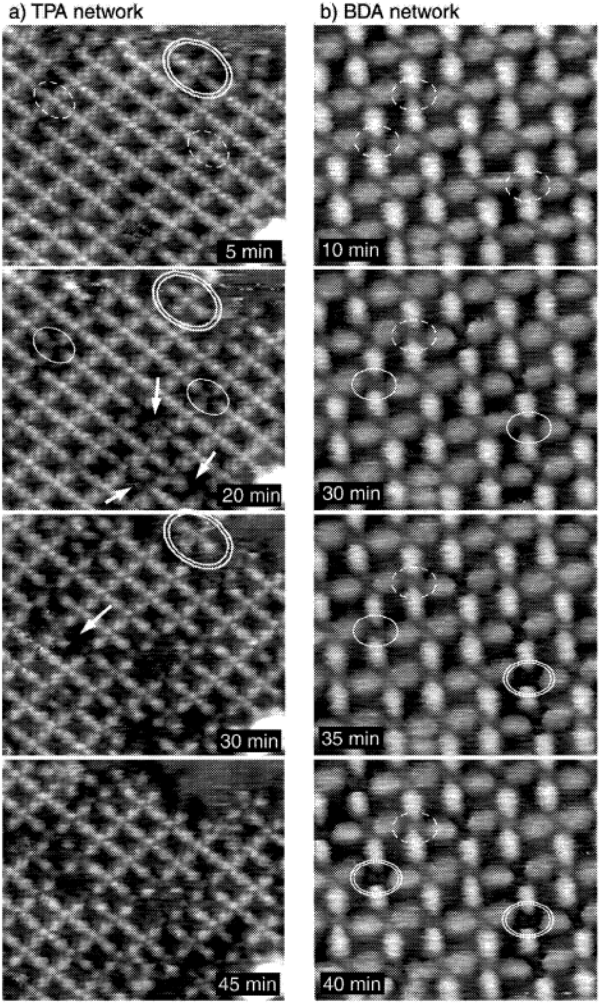

Figure 4.9: STM topographs of a TPA (a) and BDA network (b) while dosing oxygen ($P_{O_2} \approx 5 \times 10^{-9}$ mbar). The respective area was scanned in 5 min intervals (~ 4.5 min per image). For each image the starting time is given after the beginning of oxygen dosing. **(a)** The dashed and solid ellipses indicate pristine and altered iron dimers, respectively. The double ellipse shows a cross shaped complex which first detaches and then leaves the structure. **(b)** The dashed, solid and double ellipses indicate the three stages of BDA iron dimers. First, the unaffected iron (dashed el.) turns into dim centers (solid el.). After a while they undergo a further transition into a black center (double el.) with two broad round features.

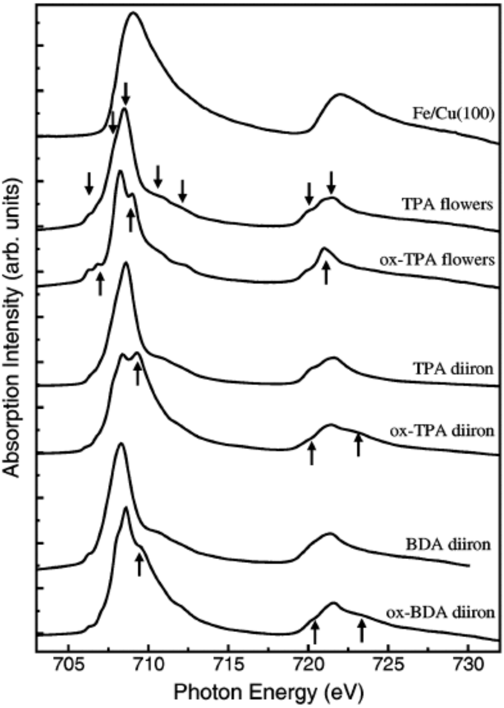

Figure 4.10: Comparison between the Fe XAS spectra ($\mu^+ + \mu^-$) at the $L_{2,3}$ edges for 0.025 ML Fe/Cu(100) and the pristine and the oxygenated networks. The data were measured at 5 K.

symmetry [243]. After oxygen dosing the XAS spectra change significantly for all three considered structures. The spectral weight at the L_3 edge is shifted to higher photon energies compared to the regular structures. Upward pointing arrows mark the changes in the spectral structure after the adsorption of oxygen. Similar features were found for all three structures and reveal a strong influence of the additional oxygen ligand on the electronic configuration of Fe. Note, that the XAS spectra presented for the oxygenated phases are a linear combination of the spectra of unaffected and modified Fe centers. According to the STM studies and the employed oxygen dosage the number of modified Fe atoms is expected to be close to saturation.

The spectrum of the oxygenated flower phase can be simulated by calculating the

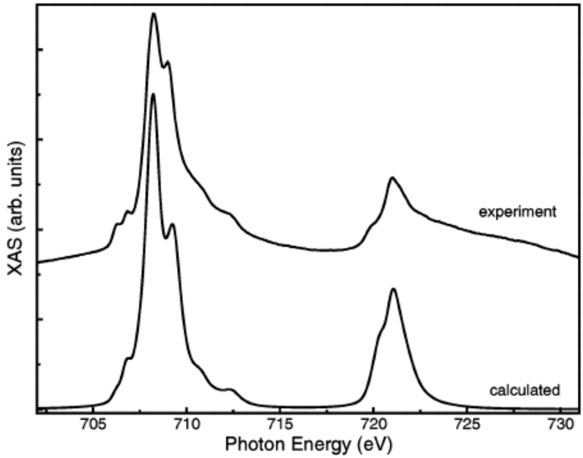

Figure 4.11: Comparison between the calculated and experimental XAS spectra ($\mu^+ + \mu^-$) of the oxygenated TPA flower phase. The calculated spectrum of an Fe2+ ion in an octahedral crystal field with strong tetrahedral distortion reproduces all spectral features observed in the experimental data.

XAS of an Fe^{2+} ion in an octahedral crystal field with strong tetragonal distortion (cf. Figure 4.11). All spectral features in the experimental data can be reproduced by the calculated spectrum. This shows, that, although charge transfer with the substrate is present [244], the local Fe electronic configuration is largely determined by the molecular ligands. For the other structures theoretical investigations are still in progress.

The combined STM and XAS experiments show that oxygen molecules bind to the iron centers of mono- and diiron coordination structures and induce significant changes in the electronic configuration of the Fe atoms. Although the actual binding configuration of the oxygen is not known, e.g., end-on or side-on attachment of the O_2 molecule, we presume that the oxygen remains in the molecular form when adsorbed on the mononuclear iron structures. At elevated temperatures it is expected that the (activated) oxygen molecule dissociates. This is reflected by the phase shown in Figure 4.8(e) which is also attained by annealing the oxidized TPA single row phase. The Fe^{2+} ions used for the calculated XAS spectra of the TPA flower phase suggest that no oxidative charge transfer occurs from the $Fe(TPA)_4$ complex to the O_2 molecule. However, the calculation represents only a preliminary result. Moreover, it is known for the conventional 3D mimics, that only very few ferrous complexes having non-porphyrin ligands (non-heme) react with dioxygen to form stable adducts [59]. Additional information from theory is also required in order to understand the phase transformation at elevated temperatures.

Different binding configurations of oxygen molecules are also discussed for the diiron structures in the literature [59]. Besides mononuclear binding modes several bridging configurations, where the O_2 long axis is parallel or perpendicular to the Fe dimer orientation, have been proposed and verified. Diiron(II) complexes of 3D mimics readily bind oxygen molecules and usually form peroxo-diiron(III) adducts (LFe^{2+}-$Fe^{2+}L$ + $O_2 \leftrightarrow LFe^{3+}$-$O_2^{2-}$-$Fe^{3+}L$, where L denotes the ligands). The alteration of the ligands affects the reactivity of the metal centers and also the stability of the peroxo-diiron(III) species. Usually, attachment of oxygen molecules to the metal centers is accompanied by a ligand rearrangement [220]. Some of the synthesized peroxo-diiron(III) complexes are very unstable and decompose at relatively low temperatures ~ 200 K. However, the utilization of these complexes in the catalytic oxidation of substrates, e.g., hydroxylation or oxygenation of alkanes, stable oxo or peroxo intermediates are required.

In our study we examined the response to dioxygen of two related diiron complexes. Since the TPA diiron structure is not stable upon oxygen adsorption we assume that the O–O bond is cleaved forming a complex where each oxygen atom is attached to one iron atom. In the rearranged structure the FeO oxygen atom replaces one of the coordination bonds to the carboxylate groups. We presume that the oxidation state of iron is changed from Fe(II) to Fe(III), but theoretical input is needed to clarify this issue and shed light on the reaction mechanism of the oxidation. In contrast to the TPA diiron network the BDA structure is preserved upon exposure to oxygen at room temperature, although the thermal stability is considerably reduced. The observation of two adsorption steps in the STM experiments indicate that there exist several stages in the reaction with oxygen which are separated by energy barriers. We believe that the intermediate state represents an adsorption configuration with an intact oxygen molecule (cf. nodes marked by solid ellipses in Figure 4.9). The final state could be a reconfiguration of the oxygen molecule, i.e., the binding mode changes from a (mononuclear) end-on or bridging to another bridging configuration involving potential charge transfer. But similar to the TPA diiron structure the dark centers could be also due to the dissociation of the oxygen molecule. Nevertheless, the oxygenated BDA complex reveals a higher stability compared to that of TPA. This is attributed to the differences in the coordination configuration.

Activation of oxygen molecules by transition metal complexes in proteins is an extensively studied phenomena with a high potential for industrial applications. The fabrication and investigation of such biological mimics at surfaces represents a new way to examine the intriguing properties of these systems. Simple synthesis and surface mediated charge transfer are the assets of this approach. Especially the high–resolution and manipulation capability of scanning probe methods as well as the high sensitivity of x-ray absorption techniques enables one to study the chemical reaction in great structural and chemical detail. The measurements of the response of surface–supported metal complexes to O_2 molecules reported in this Section represent preliminary results, but also demonstrate the potential of this approach. Further theoretical investigations and experiments are required to get insight into the mechanisms of dioxygen activation by heme and non-heme complexes.

4.3 Magnetic Properties of Metal-Coordination Structures at Surfaces

In this Section we report on the magnetic properties of Fe centers in the TPA flower, TPA diiron and BDA network phases at a Cu(100) surface. The coordination structures are described in detail in Section 3.1 and ref. [155]. X-ray absorption spectroscopy (XAS) and x-ray magnetic circular dichroism (XMCD) measurements of Fe–TPA and Fe–BDA metal–organic coordination networks (MOCNs) were performed to reveal valence state and magnetic configuration of the metal centers. We show that the Fe centers in mono- and dinuclear Fe–carboxylate coordination complexes possess a valence state close to Fe^{2+} that is markedly different from that of Fe atoms deposited on a bare Cu(100) surface. The Fe ions present an intermediate spin configuration and show paramagnetic behavior down to 5 K. We also show that the magnitude of the spin and orbital moment as well as the occurrence of in–plane, out–of–plane magnetic anisotropy can be effectively controlled by the coordination geometry. Furthermore, our measurements reveal that the magnetic properties of the Fe centers are predominantly determined by the metal–ligand interactions rather than by the interaction with the substrate.

The XAS experiments were conducted at beamline ID08 of the European Synchrotron Radiation Facility in Grenoble. Preparation of the coordination structures phases was carried out *in situ* and characterized by STM in a UHV chamber directly connected to the high–field magnet chamber of the ID08 beamline. XAS spectra were measured at the $L_{2,3}$ Fe edges in total electron yield mode using circularly polarized light with $99 \pm 1\%$ degree of polarization in magnetic fields of up to 6 T. The XMCD spectra were obtained by taking the difference of the XAS spectra recorded for parallel (μ^+) and antiparallel (μ^-) alignment of the photon spin with applied magnetic field $\mathbf{B}$. To probe the out–of–plane and in–plane magnetization the sample was rotated between normal incidence ($\theta = 0°$) and grazing incidence ($\theta = 70°$) with respect to the direction of the photon beam. STM images of the samples were recorded prior to XAS measurements which enabled us to optimize the self–assembly parameters of the MOCNs to ensure the homogeneity of the samples by probing different regions of the surface.

XAS spectra of the different phases (Fig. 4.10) are presented and discussed in the previous Section 4.2. The XAS data reveals that the electronic structure of the Fe centers is mainly determined by the strong coordination bonds to the carboxylate ligands. Comparing the spectra of the Fe complexes to experimental data [243] or simulated spectra (cf. Section 4.2) suggests a +2 oxidation state of the iron atoms, which is often encountered in such systems. The XAS spectra change significantly upon O_2 dosing as described in the previous Section 4.2, indicating that the additional on–top ligand significantly affects the electronic state of the Fe centers. Analogue conclusions apply to the magnetic properties of Fe in the MOCNs. Figures 4.12 (a) and (b) show the μ^+ and μ^- spectra of Fe(TPA)$_4$ (flowers) and ox-Fe(TPA)$_4$ (oxygenated flowers) recorded at $T = 5$ K and $\mathbf{B} = 6$ T (top panel) and the corresponding XMCD (bottom panel) at $\theta = 0°$ and 70°. Both phases present a sizeable dichroism indicating that the Fe d-states are exchange–split in the presence of the ligand field and possess a nonzero magnetic moment. There are remarkable differences between Fe(TPA)$_4$ and ox-Fe(TPA)$_4$. First, the magnitude of the Fe moment is significantly larger in ox-Fe(TPA)$_4$ compared to Fe(TPA)$_4$, as shown by the amplitude of the XMCD intensity relative to the total XAS signal in the two cases. Second, the magnetic anisotropy easy axis changes abruptly from in–plane in Fe(TPA)$_4$ to out–of–plane in ox-Fe(TPA)$_4$, as given by the comparison of the XMCD at $\theta = 0°$ and 70° for each phase.

Applying the XMCD sum rules [108, 111] to the spectra reported in Figure 4.12 allows to determine the effective spin moment $m_S + m_T$, where m_S and m_T represent the magnetic spin and dipole moment, and the orbital moment m_L of Fe in the MOCNs, provided that the number of unoccupied d-states is known ($n_d = 3.34$ in bulk bcc Fe [116], $n_d = 4$ in Fe^{2+}, the n_d values for the coordination structures are expected to be close to 4). The corresponding values, obtained after subtraction of the substrate background signal and the step–like contribution of $2p \rightarrow 4s$ transitions [103] are reported in Table 4.2. We note that these values, measured at $\mathbf{B} = 6$ T and $T = 5$ K, do not represent the full saturated magnetic moments (see the magnetization curves in the insets of Fig. 4.12), and that m_S and m_T cannot be easily separated in the present case [112]. We can say, however, that the spin configuration in the two phases is intermediate with respect to the low–spin (S=0) and high–spin (S=2) states of an Fe^{2+} ion. This can be attributed to the strength and symmetry of the ligand field as in planar

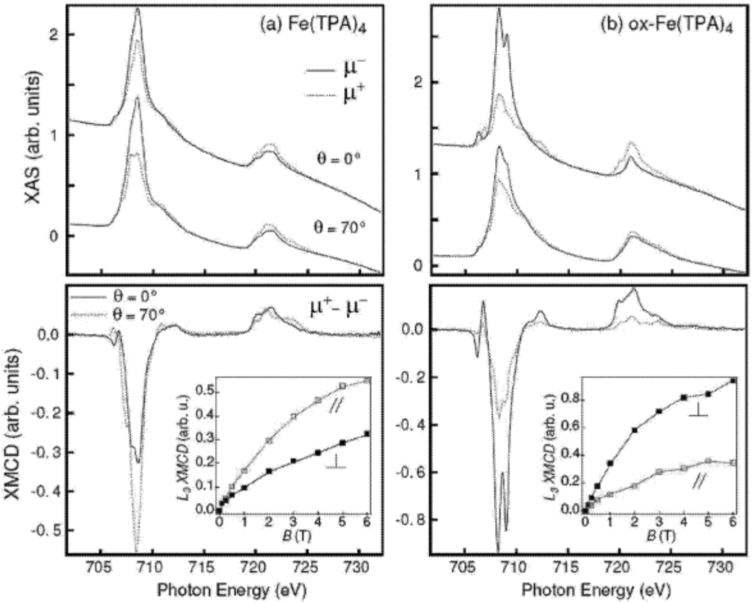

Figure 4.12: XAS spectra recorded for parallel (μ^+, dotted line) and antiparallel (μ^-, solid line) alignment of the photon spin with applied field $\mathbf{B} = 6$ T at $\theta = 0°$ and 70°, $T = 5$ K for (a) Fe(TPA)$_4$ and (b) ox-Fe(TPA)$_4$ coordination networks shown in Fig. 4.8(a). The spectra have been normalized to the same $\mu^+ + \mu^-$ L_3 edge intensity for comparison. The corresponding XMCD ($\mu^+ - \mu^-$) is shown in the bottom panels for $\theta = 0°$ (solid lines) and $\theta = 70°$ (dotted lines). The magnetization curves in the insets are obtained by recording the L_3 XMCD intensity at 708.3 eV as a function of $\mathbf{B}$, for $\theta = 0°$ (full squares) and $\theta = 70°$ (open squares).

Fe^{2+} compounds (e.g., Fe-phthalocyanines where S=1 [245]) but also to the presence of covalent interactions between the Fe atoms and the Cu substrate leading to noninteger spin values. The balance of such interactions is evidently altered in ox–Fe(TPA)$_4$ relative to Fe(TPA)$_4$, resulting in a strongly enhanced effective spin moment, and different preferential orientation of m_{L} (Table 4.2). As predicted by a perturbative treatment of the spin–orbit interaction [246], m_{L} favors the in–plane orientation of the easy axis in the Fe(TPA)$_4$ phase and out–of–plane in ox–Fe(TPA)$_4$. The slow saturation of the hard axis magnetization as a function of $\mathbf{B}$ (Fig. 4.12, insets) indicates that the magnetic

	$(m_S + m_T)/n_d$ [μ_B]	m_L/n_d [μ_B]
Fe-TPA flowers	$0.29\,(0.34) \pm 0.03$	$0.05\,(0.10) \pm 0.02$
Fe-TPA ox–flowers	$0.64\,(0.22) \pm 0.04$	$0.13\,(0.06) \pm 0.02$
Fe-TPA diiron	$0.27\,(0.26) \pm 0.04$	$0.04\,(0.05) \pm 0.02$
Fe-BDA	$0.19\,(0.26) \pm 0.02$	$0.03\,(0.07) \pm 0.01$
Fe/Cu(100)	$0.45\,(0.39) \pm 0.03$	$0.05\,(0.04) \pm 0.01$

Table 4.2: Magnetic spin (m_S), dipole (m_T), and orbital (m_L) moment of Fe in the MOCNs per number of unoccupied *d*-states (n_d) as derived by application of the XMCD sum rules to the data shown in Fig. 4.12. The values between parentheses correspond to $\theta = 70°$. The number of holes n_d is not known for the coordination structures, but it is expected to be close to 4. $n_d = 3.34$ for the Fe/Cu(100) system.

anisotropy is significant in both Fe(TPA)$_4$ and ox–Fe(TPA)$_4$. The high–field slope of the magnetization curves also suggests that the saturation magnetic moments might differ in the in–plane and out–of–plane directions, an effect that has been observed in single–crystals of high–spin Fe^{2+} cubic compounds with tetragonal distortion [247].

Paramagnetic behavior is also observed down to $T = 5$ K for both diiron structures, TPA and BDA networks, as shown by the absence of remanent magnetization and by the monotonous slope of the magnetization curves in Fig. 4.13 and correspondingly for the TPA flower phases in Figure 4.12. Also, the amplitude of the XMCD intensity of all considered structures relative to the total XAS signal follows a Curie–like behavior during field–cooled measurements from 300 K to 5 K (not shown), typical for paramagnetic systems. In Figure 4.13(a,b) (top panel) the μ^+ and μ^- XAS spectra are presented for the TPA and BDA diiron structures. Similarly to the pristine TPA flower phase the dinuclear iron centers reveal an in–plane easy magnetization axis. This anisotropy seems to be more pronounced in the BDA structure compared to that of TPA. The magnetic moments obtained for these structures are summarized in Table 4.2. Their magnitude is slightly smaller than the moments found for the monoiron TPA flower structure. Although, the XAS spectra of the BDA network reveal clear changes upon O$_2$ dosing (cf. Figure 4.10) no reversal of the easy magnetization axis has been observed for this system (not shown), although the anisotropy is very weak. The negligible magnetic coupling between the Fe atoms in the network nodes is easily explained by their substantial separation (> 10 Å, cf. Section 3.1 and ref. [155]), with the TPA and BDA molecules not being able to couple adjacent Fe moments. The possibility of employing shorter linker molecules, and/or fully 2D reticulated architectures to mediate a ferromagnetic or antiferromagnetic interaction between the transition-metal centers is of great interest for future studies.

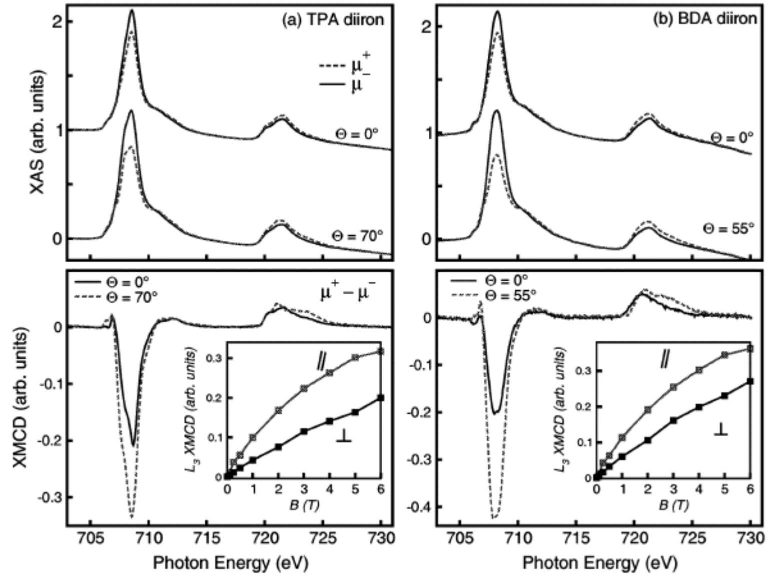

Figure 4.13: XAS spectra recorded for parallel (μ^+, dotted line) and antiparallel (μ^-, solid line) alignment of the photon spin with applied field $\mathbf{B} = 6$ T at $\theta = 0°$ and 55° or 70°, $T = 5$ K or 10 K for (a) TPA diiron and (b) BDA diiron coordination networks, respectively. The spectra have been normalized to the same $\mu^+ + \mu^-$ L_3 edge intensity for comparison. The corresponding XMCD ($\mu^+ - \mu^-$) is shown in the bottom panels for $\theta = 0°$ (solid lines) and $\theta = 55°$ or $\theta = 70°$ (dotted lines). The magnetization curves in the insets of the TPA and BDA structures are obtained by recording the L_3 XMCD intensity at 708.6 eV and 708.0 eV, respectively, as a function of $\mathbf{B}$, for $\theta = 0°$ (full squares) and $\theta = 70°$ (open squares).

In conclusion, our results represent the first characterization of the electronic and magnetic properties of transition metal centers in metal–organic supramolecular compounds synthesized at surfaces. The rich multiplet structure observed in the $L_{2,3}$ XAS and XMCD spectra of Fe in mononuclear Fe(TPA)$_4$ complexes self–assembled on Cu(100) compared to the relatively featureless spectra of Fe deposited on the bare substrate indicates the dominant influence of the ligand bonds on the electronic ground state of the metal centers. This result proves that genuine coordination architectures have been obtained and suggests that the rich variety of motifs and design principles of coordination chemistry can be generally employed at surfaces to develop molecule–based materials with tailored electronic and magnetic properties, which may originate from that of the building blocks or emerge as a new property from the molecule–substrate interaction. XMCD data allowed to determine the existence of a strongly anisotropic magnetic moment localized on the Fe atoms in Fe(TPA)$_4$. Oxidation of this phase provides an additional oxygen ligand per Fe atom. The modification of the ligand field significantly enhances the magnitude of the Fe magnetic moment and causes the reversal of the magnetic anisotropy axis from in–plane to out–of–plane.

Conclusions and Perspectives

In the present thesis supramolecular architectures at well-defined metal surfaces were studied. The major part is concerned with the exploration of intermolecular forces governing the formation of highly ordered 2D assemblies. In addition, the chemical and magnetic properties of the functionalized surfaces have been examined.

In conventional 3D coordination chemistry a rich variety of supramolecular structures have been synthesized and characterized. Recently, it was demonstrated, that the concepts of this approach can be also applied at surfaces to construct highly ordered supramolecular structures. We explored the main driving forces for the fabrication of surface supported supramolecular architectures, namely hydrogen bonding, metal–ligand interactions and electrostatic forces. It is shown, how these types of interactions can be utilized to steer the formation of supramolecular assemblies at surfaces. The results considerably broaden the previously reported design principles of supramolecular nanostructures at surfaces.

Hydrogen–bonded motifs were examined in the formation of low-dimensional assemblies of TPA, PDA, BDA and SDA molecules (cf. Table 1.1) at a Cu(100) surface. The investigations of these simple aromatic carboxylic acids revealed how the protonation status of the carboxyl moieties affects the topology of the assemblies. The catalytic activity of the copper substrate facilitates the irreversible deprotonation of the COOH group at approximately room temperature. This is accompanied by a rearrangement in the molecular structures which has been shown in detail for the TPA/Cu(100) system. Alteration of the symmetry and functionality of the molecular backbone is expressed in distinct supramolecular assemblies. The comparative studies of the TPA/PDA and BDA/SDA systems provides valuable information how the dimensionality and symmetry of supramolecular architectures at surfaces can be effectively controlled by the number and symmetry of molecular binding sites.

Further control on the topology of the assemblies can be achieved by metallo-supramolecular engineering. This approach is in particular interesting because besides the increased bond strength compared to hydrogen bridge bonds it introduces transition metal centers bearing intriguing and unprecedented properties. The concepts of coordination chemistry have been successfully applied to the surface by employing various aromatic molecular linkers comprising carboxyl, pyridyl and hydroxyl functional groups in conjunction with Fe atoms. Interactions between the adsorbates and the substrate result in distinct supramolecular coordination structures of closely related organic ligands. Furthermore, the occurrence of structural isomerism is addressed in a comparative study of heterofunctional and homofunctional linker molecules, PVBA and BDA, respectively. The attained improved control on the structural motif by the heterofunctional ligand is due to the fact that each functional end group binds preferentially to one of the two binding sites of the metal center, i.e., axial and bridging positions. The results furthermore nicely reveal that nitrogen as well as hydroxyl containing units can be readily employed in metal–directed assembly of organic species at surfaces, which expands the recently reported coordination motifs of carboxylic ligands. Furthermore, we introduced a novel strategy for the construction of well-ordered supramolecular architectures at metal surfaces. By making use of the oppositely charged alkali metal ions and carboxylate molecules we were able to construct long–range ordered 2D structures at a Cu(100) surface. Electrostatic forces dominate the interaction between the components and mediate a coupling between the different units which is of intermediate strength similar to the above mentioned forces. It is expected that in the case of the ionic structures the substrate is more important in the determination of the supramolecular topology compared to the transition metal coordination networks. The results suggest that the substrate might be also used to influence deliberately the coordination geometry and thus the electronic state of the metal centers.

The realized coordination structures have been employed to investigate the chemical and magnetic properties of surface–supported supramolecular architectures. Adsorption studies employing C_{60} guest molecules revealed the robustness of the open network structures and demonstrated the suitability of these functionalized surfaces to control the binding strength of guest species to the substrate. Moreover, the chemical reactivity of the Fe centers was probed by exposing the coordination structures to oxygen molecules. Upon oxygen adsorption distinct structural and electronic modification of the metal centers are observed by STM and XAS measurements, respectively. Activation of oxygen molecules especially by Fe coordination centers constitutes an important phenomena in biological systems. Hence, the simple synthesis and powerful characterization methods represent a novel and promising approach for the understanding of the underlying reaction mechanisms.

The magnetic properties of surface–supported Fe coordination structures were explored by means of XAS and XMCD. Fe $L_{2,3}$ XAS and XMCD spectra of the compounds revealing a rich multiplet structure indicate the dominant influence of the coordination bonds on the electronic state of the metal centers. Furthermore, the Fe atoms are found to have an intermediate spin ground state and show paramagnetic behavior down to 5 K. The adsorption of oxygen molecules serving as an additional on–top ligand induces significant changes in the ligand field imposed on the Fe center. It is demonstrated for the monoiron TPA "flower phase" that the adsorbed oxygen molecule enhances the magnitude of the Fe magnetic moment and causes the reversal of the magnetic anisotropy axis from in–plane to out–of–plane. The experiments illustrate the potential of the creation of self-assembled supramolecular magnetic materials at surfaces.

The presented results in thesis give rise for several future investigations and developments. For the envisioned future applications, e.g., (biomimetic) catalysts, high–density magnetic storage devices or molecular electronics, it is mandatory to continue the exploration of the principles of supramolecular engineering at surfaces. A deeper understanding of the emerging chemical and physical properties from the molecules or metal centers, by correlating structure and functionality, will provide design strategies for the construction of novel materials. In addition to the experimental work, thorough theoretical analysis is required for the detailed understanding of the structural and functional properties as well as the kinetics of the self-assembly processes. Studies employing non–metal substrates will be of great interest for electrical transport and optical applications. Moreover, the step towards the synthesis of surface–supported supramolecular assemblies under mild conditions, e.g., solution processed functionalized surfaces, constitutes an appealing evolution from a technological point of view. The advent of scanning probe microscopies like atomic force microscopy (AFM) and scanning tunneling microscopy (STM) has stimulated a considerable increase in research activity in surface chemistry. This increase is part of a more general interest in nanotechnology. Hence, the synergetic cooperation between surface scientist, organic chemists and theoreticians in the interdisciplinary field of material research, which has already introduced new ideas and concepts to manifold technological areas, e.g., heterogenous catalysis, selective gas storage and organic (opto-) electronics, opens the avenue towards novel materials with unprecedented physical properties.

Bibliography

[1] J. K. Gimzewski and C. Joachim, Science **283**, 1683 (1999).

[2] W. Ho, J. Chem. Phys. **117**, 11033 (2002).

[3] T. A. Jung, R. R. Schlittler, and J. K. Gimzewski, Nature **386**, 696 (1997).

[4] M. Böhringer, K. Morgenstern, W.-D. Schneider, R. Berndt, F. Mauri, A. De Vita, and R. Car, Phys. Rev. Lett. **83**, 324 (1999).

[5] A. Dmitriev, H. Spillmann, N. Lin, J. V. Barth, and K. Kern, Angew. Chem. Int. Ed. **42**, 2670 (2003).

[6] J. V. Barth, J. Weckesser, C. Cai, P. Günter, L. Bürgi, O. Jeandupeux, and K. Kern, Angew. Chem. Int. Ed. **39**, 1230 (2000).

[7] H. Spillmann, A. Dmitriev, N. Lin, P. Messina, J. V. Barth, and K. Kern, J. Am. Chem. Soc. **125**, 10725 (2003).

[8] T. Yokoyama, S. Yokoyama, T. Kamikado, Y. Okuno, and S. Mashiko, Nature **413**, 619 (2001).

[9] M. Schunack, L. Petersen, A. Kühnle, E. Laegsgaard, I. S. I. Johannsen, and F. Besenbacher, Phys. Rev. Lett. **86**, 456 (2001).

[10] F. Rosei, M. Schunack, P. Jiang, A. Gourdon, E. Laegsgaard, I. Stensgaard, C. Joachim, and F. Besenbacher, Science **296**, 328 (2002).

[11] K. W. Hipps, L. Scudiero, D. E. Barlow, and J. M. P. Cooke, J. Am. Chem. Soc. **124**, 2126 (2002).

[12] J. A. Theobald, N. S. Oxtoby, M. A. Phillips, N. R. Champness, and P. H. Beton, Nature **424**, 1029 (2003).

[13] G. P. Lopinski, D. J. Moffatt, D. D. Wagner, and R. A. Wolkow, Nature **392**, 909 (1998).

[14] A. Kühnle, T. R. Linderoth, B. Hammer, and F. Besenbacher, Nature **415**, 891 (2002).

[15] J. V. Barth, J. Weckesser, G. Trimarchi, M. Vladimirova, A. De Vita, C. Cai, H. Brune, P. Günter, and K. Kern, J. Am. Chem. Soc **124**, 7991 (2002).

[16] V. Humblot, M. O. Lorenzo, C. J. Baddeley, S. Haq, and R. Raval, J. Am. Chem. Soc. **126**, 6460 (2004).

[17] L. A. M. M. Barbosa and P. Sautet, J. Am. Chem. Soc. **123**, 6639 (2001).

[18] T. Zambelli, J. V. Barth, J. Wintterlin, and G. Ertl, Nature **390**, 495 (1997).

[19] G. A. Somorjai, J. Phys. Chem. B **106**, 9201 (2002).

[20] M. Dürr, A. Biedermann, Z. Hu, U. Höfer, and T. F. Heinz, Science **296**, 1838 (2002).

[21] G. S. MacCarty and P. S. Weiss, J. Phys. Chem. B **106**, 8005 (2002).

[22] X.-C. Guo and R. J. Madix, J. Phys. Chem. B **107**, 3105 (2003).

[23] M. O. Lorenzo, S. H. T. Bertrams, P. Murray, R. Raval, and C. J. Baddeley, J. Phys. Chem. B **103**, 10661 (1999).

[24] J. Wintterlin, Adv. Catal. **45**, 131 (2000).

[25] F. Besenbacher, I. Chorkendorff, B. S. Clausen, B. Hammer, A. M. Molenbroek, J. K. Nørskov, and I. Stensgaard, Science **279**, 1913 (1998).

[26] S. Rusponi, T. Cren, N. Weiss, M. Epple, P. Buluschek, L. Claude, and H. Brune, Nat. Mater. **2**, 546 (2003).

[27] M. Bode, M. Getzlaff, and R. Wiesendanger, Phys. Rev. Lett. **81**, 4256 (1998).

[28] W. Wulfhekel and J. Kirchner, Appl. Phys. Lett. **75**, 1944 (1999).

[29] R. Yamachika, M. Grobis, A. Wachowiak, and M. F. Crommie, Science **304**, 281 (2004).

[30] M. F. Crommie, C. P. Lutz, and D. M. Eigler, Science **262**, 218 (1993).

[31] A. J. Heinrich, C. P. Lutz, J. A. Gupta, and D. M. Eigler, Science **298**, 1381 (2002).

[32] K.-F. Braun and K.-H. Rieder, Phys. Rev. Lett. **88**, 096801 (2002).

[33] J. S. Lindsey, New J. Chem. **15**, 153 (1991).

[34] G. M. Whitesides, J. P. Mathias, and C. T. Seto, Science **254**, 1312 (1991).

[35] M. M. Conn and J. J. Rebek, Chem. Rev. **97**, 1647 (1997).

[36] M. C. T. Fyfe and J. F. Stoddart, Coord. Chem. Rev. **183**, 139 (1999).

[37] G. R. Desiraju, *Crystal engineering: The design of organic solids* (Elsevier, Amsterdam, 1989).

[38] B. Moulton and M. J. Zaworotko, Chem. Rev. **101**, 1629 (2001).

[39] D. Braga, Chem. Commun. **22**, 2751 (2003).

[40] F. Vögtle, *Supramolecular chemistry* (Wiley, New York, 1989).

[41] J. L. Atwood, J. E. D. Davies, D. D. MacNicol, F. Vögtle, and J.-M. Lehn, eds., *Comprehensive Supramolecular Chemistry* (Pergamon, Oxford, 1996).

[42] J.-M. Lehn, *Supramolecular Chemistry: Concepts and Perspectives* (VCH, Weinheim, Germany, 1995).

[43] G. A. Jeffrey and W. Saenger, *Hydrogen bonding in biological systems* (Springer, Berlin, 1991).

[44] T. Kawai, H. Tanaka, and T. Nakagawa, Surf. Sci. **386**, 124 (1997).

[45] M. Furukawa, H. Tanaka, K.-I. Sugiura, Y. Sakata, and T. Kawai, Surf. Sci. Lett. **445**, L58 (2000).

[46] J. Weckesser, A. De Vita, J. V. Barth, C. Cai, and K. Kern, Phys. Rev. Lett. **87**, 096101 (2001).

[47] J. N. O'Shea, J. Schnadt, P. A. Brühwiler, H. Hillesheimer, N. Mårtensson, L. Patthey, J. Krempasky, C. Wang, Y. Luo, and H. Ågren, J. Phys. Chem. B **105**, 1917 (2001).

[48] T.-Q. Nguyen, M. L. Bushey, L. E. Brus, and C. Nuckolls, J. Am. Chem. Soc. **124**, 15051 (2002).

[49] A. McNutt, S. Haq, and R. Raval, Surf. Sci. **531**, 131 (2003).

[50] S. De Feyter and F. C. De Schryver, Chem. Soc. Rev. **32**, 139 (2003).

[51] G. Wilkinson, R. D. Gillard, and J. A. McCleverty, eds., *Comprehensive coordination chemistry* (Pergamon, Oxford, 1987).

[52] B. J. Holliday and C. A. Mirkin, Angew. Chem. Int. Ed. **40**, 2022 (2001).

[53] A. Werner, Z. Anorg. Chem. **3**, 267 (1893).

[54] M. Fujita, Chem. Soc. Rev. **27**, 417 (1998).

[55] B. Olenyuk, J. A. Whiteford, A. Fechtenkötter, and P. J. Stang, Nature **398**, 796 (1999).

[56] M. E. Davis, Nature **417**, 813 (2002).

[57] A. Stein, Adv. Mater. **15**, 763 (2003).

[58] R. Vilar, Angew. Chem. Int. Ed. **42**, 1460 (2003).

[59] A. L. Feig and S. J. Lippard, Chem. Rev. **94**, 759 (1994).

[60] E. I. Solomon, T. C. Brunold, M. I. Davis, J. N. Kemsley, S.-K. Lee, N. Lehnert, F. Neese, A. J. Skulan, Y.-S. Yang, and J. Zhou, Chem. Rev. **100**, 235 (2000).

[61] S.-W. Hla and K.-H. Rieder, Annu. Rev. Phys. Chem. **54**, 307 (2003).

[62] J. R. Hahn and W. Ho, Phys. Rev. Lett. **87**, 166102 (2001).

[63] T. H. Rod and J. K. Nørskov, Surf. Sci. **500**, 678 (2002).

[64] N. Lorente, R. Rurali, and H. Tang, J. Phys.: Condens. Matter **17**, S1049 (2005).

[65] O. Kahn, *Molecular magnetism* (Wiley-VCH, New York, 1993).

[66] J. R. Galán-Mascarós and K. R. Dunbar, Angew. Chem. **115**, 2391 (2003).

[67] S. Piligkos, G. Rajaraman, M. Soler, N. Kirchner, J. van Slageren, R. Birchner, S. Parsons, H.-U. Güdel, J. Kortus, W. Wernsdorfer, G. Christou, and E. K. Brechin, J. Am. Chem. Soc. **127**, 5572 (2005).

[68] M. Ruben, J. Rojo, F. J. Romero-Salfuero, L. H. Uppadine, and J.-M. Lehn, Angew. Chem. Int. Ed. **43**, 3644 (2004).

[69] D. Maspoch, D. Ruiz-Molina, K. Wurst, N. Domingo, M. Cavallini, F. Biscarini, J. Tejada, C. Rovira, and J. Veciana, Nat. Mater. **2**, 190 (2003).

[70] G. J. Halder, C. J. Kepert, B. Moubaraki, K. S. Murray, and J. D. Cashion, Science **298**, 1762 (2002).

[71] O. Kahn and C. J. Martinez, Science **279**, 44 (1998).

[72] G. Binnig, H. Rohrer, C. Gerber, and E. Weibel, Phys. Rev. Lett. **49**, 57 (1982).

[73] I. Giaever, Phys. Rev. Lett. **5**, 147 (1960).

[74] J. Bardeen, Phys. Rev. Lett. **6**, 57 (1961).

[75] E. L. Wolf, *Principles of Electron Tunneling Spectroscopy* (Oxford University Press, New York, 1985).

[76] J. Tersoff and D. R. Hamann, Phys. Rev. Lett. **50**, 1998 (1983).

[77] A. Selloni, P. Carnevali, E. Tosatti, and C. D. Chen, Phys. Rev. B **31**, 2602 (1985).

[78] N. D. Lang, Phys. Rev. **34**, 5947 (1986).

[79] C. J. Chen, *Introduction to Scanning Tunneling Microscopy* (Oxford University Press, New York, 1993).

[80] J. Stroscio and W. Kaiser, eds., *Scanning Tunneling Microscopy* (Academic Press, San Diego, 1993).

[81] J. K. Gimzewski, E. Stoll, and R. R. Schlittler, Surf. Sci. **181**, 267 (1987).

[82] H. Ohtani, R. J. Wilson, S. Chiang, and C. M. Mate, Phys. Rev. Lett. **60**, 2398 (1988).

[83] P. H. Lippel, R. J. Wilson, M. D. Miller, C. Wöll, and S. Chiang, Phys. Rev. Lett. **62**, 171 (1989).

[84] C. J. Chen, J. Vac. Sci. Tech. A **9**, 44 (1991).

[85] M. T. et al., Surf. Sci. Rep. **13**, 265 (1991).

[86] M. Tsukada, H. Kakeshima, N.Issahiki, and K. Kobayashi, Surf. Sci. **266**, 253 (1992).

[87] C. Doyen, D. Drakova, J. V. Barth, R. Schuster, T. Gritsch, R. J. Behm, and G. Ertl, Phys. Rev. B **48**, 1738 (1993).

[88] P. Sautet and C. Joachim, Phys. Rev B **38**, 12238 (1988).

[89] R. F. Lin, G. S. Blackmann, M. A. V. Hove, and G. A. Samorjai, Acta Cryst. B **43**, 368 (1987).

[90] P. Sautet and C. Joachim, Chem. Phys. Lett. **185**, 23 (1991).

[91] V. M. Hallmark, S. Chiang, K. P. Meinhardt, and K. Hafner, Phys. Rev. Lett. **70**, 3740 (1993).

[92] P. Sautet, Chem. Rev. **97**, 1097 (1997).

[93] M. P. Seah and W. A. Dench, Surf. Interface Anal. **1**, 2 (1979).

[94] D. A. Shirley, Phys. Rev. B **5**, 4709 (1972).

[95] J. Chastian and R. C. King, *Handbook of X-ray Photoelectron Spectroscopy: A Reference Book of Standard Spectra for Identification and Interpretation of XPS Data* (Physical Electronics Inc., Eden Prairie, Minnesota, 1995).

[96] J. Stöhr, *NEXAFS Spectroscopy* (Springer, Berlin, 1992).

[97] G. van der Laan, B. Thole, G. Sawatzky, J. B. Goedkoop, J. Fuggle, J. Esteva, R. Karnatak, J. P. Remeika, and H. Dabkowska, Phys. Rev. B **34**, 6529 (1986).

[98] C. Chen, Phys. Rev. Lett. **65**, 448 (1990).

[99] G. Schütz, W. Wagner, W. Wilhelm, P. Kienle, R. Zeller, R. Frahm, and G. Materlik, Phys. Rev. Lett. **58**, 737 (1987).

[100] C. Chen, N. Smith, and F. Sette, Phys. Rev. B **43**, 6785 (1991).

[101] Y. Wu, J. Stöhr, B. Hermsmeier, M. Samant, and D. Weller, Phys. Rev. Lett. **69**, 2307 (1992).

[102] D. Weller, Phys. Rev. Lett. **75**, 3752 (1995).

[103] C. Chen, Y. Idzerda, H.-J. Lin, N. Smith, G. Meigs, E. C. G. Ho, E. Pellegrin, and F. Sette, Phys. Rev. Lett. **75**, 152 (1995).

[104] M. Tischer, O. Hjortstam, D. Arvantitis, J. Dunn, F. May, K. Baberschke, J. Trygg, and J. Wills, Phys. Rev. Lett. **75**, 1602 (1995).

[105] J. Stöhr, J. Mag. Mag. Mat. **200**, 470 (1999).

[106] T. Jo and G. Sawatzky, Phys. Rev. B **43**, 8771 (1991).

[107] J. Erskine and E. Stern, Phys. Rev. B **12**, 5016 (1975).

[108] B. Thole, P. Carra, F. Sette, and G. van der Laan, Phys. Rev. Lett. **68**, 1943 (1992).

[109] N. Smith, C. Chen, F. Sette, and L. Mattheiss, Phys. Rev. B **46**, 1023 (1992).

[110] M. Altarelli, Phys. Rev. B **47**, 597 (1993).

[111] P. Carra, B. Thole, M. Altarelli, and X. Wang, Phys. Rev. Lett. **70**, 694 (1993).

[112] J. Stöhr and H. König, Phys. Rev. Lett. **75**, 3748 (1995).

[113] H. Dür and G. van der Laan, Phys. Rev. B **54**, R760 (1996).

[114] R. Wu and A. Freeman, J. Mag. Mag. Mat. **200**, 498 (1999).

[115] R. W. D. Wang and A. Freeman, Phys. Rev. Lett. **71**, 3581 (1993).

[116] R. Wu and A. Freeman, Phys. Rev. Lett. **73**, 1994 (1994).

[117] G. Daalderop, P. Kelly, and M. Schuurmans, Phys. Rev. B **50**, 9989 (1994).

[118] J. Weckesser. Ph.D. thesis, Ecole Polytechnique Fédérale de Lausanne (EPFL), Switzerland (2000).

[119] A. Dmitriev. Ph.D. thesis, Ecole Polytechnique Fédérale de Lausanne (EPFL), Switzerland (2003).

[120] H. Brune, H. Röder, K. Bromann, and K. Kern, Thin Solid Films **264**, 230 (1995).

[121] B. Fischer. Ph.D. thesis, Ecole Polytechnique Fédérale de Lausanne (EPFL), Switzerland (1998).

[122] M. Bott, T. Michely, and G. Comsa, Rev. Sci. Instrum. **66**, 4135 (1995).

[123] BESSY II, http://www.bessy.de.

[124] ESRF, http://www.esrf.fr.

[125] SAES Getters SpA, http://www.saesgetters.com.

[126] M. Succi, R. Canino, and B. Ferrario, Vacuum **35**, 579 (1985).

[127] E. Umbach, M. Sokolowski, and R. Fink, Appl. Phys. A **63**, 565 (1996).

[128] S. R. Forrest, Chem. Rev. **97**, 1793 (1997).

[129] M. J. S. Dewar and W. Thiel, J. Am. Chem. Soc. **99**, 4899 (1977).

[130] J. P. Stewart, J. Comp. Chem. **10**, 221 (1989).

[131] N. Lorente, M. F. G. Hedouin, R. E. Palmer, and M. Persson, Phys. Rev. B **68**, 155401 (2003).

[132] D. Philp and J. F. Stoddart, Angew. Chem. Int. Ed. **35**, 1154 (1996).

[133] J. L. Prins, D. N. Reinhoudt, and P. Timmerman, Angew. Chem. Int. Ed. **40**, 2382 (2001).

[134] G. M. Whitesides, E. E. Simanek, J. P. Mathias, C. T. Seto, D. N. Chin, M. Mammen, and D. M. Gordon, Acc. Chem. Res. **28**, 37 (1995).

[135] Q. Chen, D. J. Frankel, and N. Richardson, J. Chem. Phys. **116**, 460 (2002).

[136] A. Dmitriev, N. Lin, J. Weckesser, J. V. Barth, and K. Kern, J. Phys. Chem. B **106**, 6907 (2002).

[137] Q. Chen and N. Richardson, Nat. Mater. **2**, 324 (2003).

[138] C. C. Perry, S. Haq, B. G. Frederick, and N. Richardson, Surf. Sci. **409**, 512 (1998).

[139] Q. Chen, C. C. Perry, B. G. Frederick, P. W. Murray, S. Haq, and N. V. Richardson, Surf. Sci. **446**, 63 (2000).

[140] S. J. H. Griessl, M. Lackinger, F. Jamitzky, T. Markert, M. Hietschold, and W. M. Heckl, J. Phys. Chem. B **108**, 11556 (2004).

[141] H. Yan, J. Lu, L. Wan, and C.-L. Bai, J. Phys. Chem. B **108**, 11251 (2004).

[142] M. Śledź, J. Janczak, and R. Kubiak, J. Mol. Struct. **595**, 77 (2001).

[143] D. S. Martin, R. J. Cole, and S. Haq, Phys. Rev. B **66**, 155427 (2002).

[144] L. H. Dubois, B. Zegarski, and R. Nuzzo, Langmuir **2**, 412 (1986).

[145] B. Parker, B. Immaraporn, and A. J. Gellman, Langmuir **17**, 6638 (2001).

[146] S. W. Han, S. W. Joo, T. H. Ha, Y. Kim, and K. Kim, J. Phys. Chem. B **104**, 11989 (2000).

[147] M. Wühn, J. Weckesser, and C. Wöll, Langmuir **17**, 7605 (1901).

[148] B. Lindberg, A. Berndtsson, R. Nilsson, and R. Nyholm, Acta Chem. Scand. A **32**, 353 (1978).

[149] N. Lin, A. Dmitriev, J. Weckesser, J. V. Barth, and K. Kern, Angew. Chem. Int. Ed. **41**, 4779 (2002).

[150] T. A. Witten and L. M. Sander, Phys. Rev. B **27**, 5686 (1983).

[151] S. Chiang, Chem. Rev. **97**, 1083 (1997).

[152] A. F. Lee, K. Wilson, R. M. Lambert, A. Goldoni, A. Baraldi, and G. Paolucci, J. Phys. Chem. B **104**, 11729 (2000).

[153] T. Steiner, New J. Chemistry **1998**, 1099 (1998).

[154] J. V. Barth, J. Weckesser, N. Lin, A. Dmitriev, and K. Kern, Appl. Phys. A **76**, 645 (2003).

[155] M. A. Lingenfelder, H. Spillmann, A. Dmitriev, S. Stepanow, N. Lin, J. V. Barth, and K. Kern, Chem. Eur. J. **10**, 1913 (2004).

[156] S. Stepanow, M. Lingenfelder, A. Dmitriev, H. Spillmann, N. Lin, X. Deng, C. Cai, J. V. Barth, and K. Kern, Nat. Mater. **3**, 229 (2004).

[157] D. Bonifazi, H. Spillmann, A. Kiebele, M. de Wild, P. Seiler, F. Cheng, H.-J. Güntherodt, T. Jung, and F. Diederich, Angew. Chem. Int. Ed. **43**, 4759 (2004).

[158] L. Pérez-García and D. B. Amabilino, Chem. Soc. Rev. **31**, 342 (2002).

[159] V. Humblot, S. M. Barlow, and R. Raval, Prog. Surf. Sci. **76**, 1 (2004).

[160] S. Stepanow, T. Strunskus, M. Lingenfelder, A. Dmitriev, H. Spillmann, N. Lin, J. V. Barth, C. Wöll, and K. Kern, J. Phys. Chem. B **108**, 19392 (2004).

[161] M. Vladimirova, G. Trimarchi, J. Weckesser, K. Kern, J. V. Barth, and A. De Vita, Acta Mater. **52**, 1589 (2001).

[162] S. Leininger, B. Olenyuk, and P. J. Stang, Chem. Rev. **100**, 853 (2000).

[163] J. Y. Lu, M. A. Lawandy, J. Li, T. Yuen, and C. L. Lin, Inorg. Chem. **38**, 2695 (1999).

[164] P. J. Stang, N. E. Persky, and J. Manna, J. Am. Chem. Soc. **119**, 4777 (1997).

[165] D. Venkataraman, G. B. Gardner, S. Lee, and J. S. Moore, J. Am. Chem. Soc. **117**, 11600 (1995).

[166] M. Fujita, Y. J. Kwon, S. Washizu, and K. Ogura, J. Am. Chem. Soc. **116**, 1151 (1994).

[167] L. R. MacGillivray, R. H. Groeneman, and J. L. Atwood, J. Am. Chem. Soc. **120**, 2676 (1998).

[168] S. R. Batten and R. Robson, Angew. Chem. Int. Ed. **37**, 1460 (1998).

[169] M. Eddaoudi, D. B. Moler, H. Li, B. Chen, T. M. Reinecke, M. O'Keeffe, and O. M. Yaghi, Acc. Chem. Res. **34**, 319 (2001).

[170] Y. Cui, O. R. Evans, H. L. Ngo, P. S. White, and W. Lin, Angew. Chem. Int. Ed. **41**, 1159 (2002).

[171] S. R. Seidel and P. J. Stang, Acc. Chem. Res. **25**, 972 (2002).

[172] C. N. Rao, S. Natarajan, and R. Vaidhyanathan, Angew. Chem. Int. Ed. **43**, 1466 (2004).

[173] F. A. Cotton, C. Lin, and C. A. Murillo, Acc. Chem. Res. **34**, 759 (2001).

[174] O. M. Yaghi, M. O'Keeffe, N. W. Ockwig, H. K. Chae, M. Eddaoudi, and J. Kim, Nature **423**, 705 (2003).

[175] W. Lin, W. Lin, G. K. Wong, and T. J. Marks, J. Am. Chem. Soc. **118**, 8034 (1996).

[176] A. Facchetti, E. Annoni, L. Beverina, M. Morone, P. Zhu, T. J. Marks, and G. A. Pagani, Nat. Mater. **3**, 910 (2004).

[177] Y.-H. Kiang, G. B. Gardner, S. Lee, Z. Xu, and E. B. Lokovsky, J. Am. Chem. Soc. **121**, 8204 (1999).

[178] A. J. Fletcher, E. J. Cussen, T. J. Prior, M. J. Rosseinsky, C. J. Kepert, and K. M. Thomas, J. Am. Chem. Soc. **123**, 10001 (2001).

[179] M. Eddaoudi, J. Kim, N. Rosi, D. Vodak, J. Wachter, M. O'Keeffe, and O. M. Yaghi, Science **295**, 469 (2002).

[180] N. L. Rosi, J. Eckert, M. Eddaoudi, D. T. Vodak, J. Kim, M. O'Keeffe, and O. M. Yaghi, Science **300**, 1127 (2003).

[181] O. M. Yaghi, G. Li, and H. Li, Nature **378**, 703 (1995).

[182] L. Pan, N. Ching, X. Huang, and J. Li, Inorg. Chem. **39**, 5333 (2000).

[183] J. S. S. amd D. Whang, H. Lee, S. I. Jun, J. Oh, Y. J. Jeon, and K. Kim, Nature **404**, 982 (2000).

[184] O. Kahn, Acc. Chem. Res. **33**, 647 (2000).

[185] H. Srikanth, R. Hajndl, B. Moulton, and M. J. Zaworotko, J. Appl. Phys. **93**, 7089 (2003).

[186] A. Semenov, J. P. Spatz, M. Möller, J.-M. Lehn, B. Sell, D. Schubert, C. H. Weidl, and U. S. Schubert, Angew. Chem. Int. Ed. **38**, 2547 (1999).

[187] U. Ziener, J.-M. Lehn, A. Mourran, and M. Möller, Chem. Eur. J. **8**, 951 (2002).

[188] D. G. Kurth, N. Severin, and J. P. Rabe, Angew. Chem. Int. Ed. **41**, 3681 (2002).

[189] P. Messina, A. Dmitriev, N. Lin, H. Spillmann, M. Abel, J. V. Barth, and K. Kern, J. Am. Chem Soc. **124**, 14000 (2002).

[190] N. Lin, S. Stepanow, F. Vidal, J. V. Barth, and K. Kern, Chem. Comm. **2005**, 1681 (2005).

[191] S. Stepanow, N. Lin, F. Vidal, A. Landa, M. Ruben, J. V. Barth, and K. Kern, Nano Lett. **5**, 901 (2002).

[192] N. Lin, D. Payer, A. Dmitriev, T. Strunskus, C. Wöll, J. V. Barth, and K. Kern, Angew. Chem. Int. Ed. **44**, 1488 (2005).

[193] R. B. King, ed., *Encyclopedia of Inorganic Chemistry* (Wiley, Chichester, 1994).

[194] J. K. Gimzewski, C. Joachim, R. R. Schlittler, V. Langlais, H. Tang, and Johannsen, Science **281**, 531 (1998).

[195] D. Lee and S. J. Lippard, Inorg. Chem. **41**, 2704 (2002).

[196] H. Andres, E. L. Bominaar, J. M. Smith, N. A. Eckert, P. L. Holland, and E. Münck, J. Am. Chem. Soc. **124**, 3012 (2002).

[197] F. A. Cotton and R. A. Walton, *Multiple Bonds Between Metal Atoms* (Clarendon Press, Oxford, UK, 1993).

[198] F. A. Cotton, C. Lin, and C. A. Murillo, Proc. Natl. Acad. Sci. USA **99**, 4810 (2002).

[199] M. Eddaoudi, J. Kim, D. Vodak, A. Sudik, J. Wachter, M. O'Keeffe, and O. M. Yaghi, Proc. Natl. Acad. Sci. USA **99**, 4900 (2002).

[200] C. Cai, B. Müller, J. Weckesser, J. V. Barth, Y. Tao, M. M. Bösch, A. Kündig, C. Bosshard, I. Biaggio, and P. Günter, Adv. Mater. **11**, 750 (1999).

[201] A. Dmitriev, H. Spillmann, M. Lingenfelder, N. Lin, J. V. Barth, and K. Kern, Langmuir **20**, 4799 (2004).

[202] L. R. MacGillivray, S. Subramanian, and M. J. Zaworotko, Chem. Comm. **1994**, 1325 (1994).

[203] X. Xu, M. Nieuwenhuyzen, and S. L. James, Angew. Chem. Int. Ed. **41**, 764 (2002).

[204] A. B. Mallik, S. Lee, and E. B. Lobkovsky, Cryst. Growth Des. **5**, 609 (2005).

[205] S. De Feyter, A. Gesquiére, M. Klapper, K. Müllen, and F. C. De Schryver, Nano Lett. **3**, 1485 (2003).

[206] H. Yan, S. H. Park, G. Finkelstein, J. H. Reif, and T. H. LaBean, Science **301**, 1882 (2003).

[207] A. Chworos, I. Severcan, A. Y. Koyfman, P. Weinkam, E. Oroudjev, H. G. Hansma, and L. Jaeger, Science **306**, 2068 (2004).

[208] S. Berner, M. de Wild, L. Ramoino, S. Ivan, A. Baratoff, H.-J. Güntherodt, H. Suzuki, D. Schlettwein, and T. A. Jung, Phys. Rev. B **68**, 115410 (2003).

[209] C. F. J. Faul and M. Antonietti, Adv. Mater. **15**, 673 (2003).

[210] T. Zhang, C. Spitz, M. Antonietti, and C. F. J. Faul, Chem. Eur. J. **11**, 1001 (2005).

[211] Y. Zakrevskyy, B. Smarsly, J. Stumpe, and C. F. J. Faul, Phys. Rev. E. **71**, 021701 (2005).

[212] N. D. Lang, Phys. Rev. B **4**, 4234 (1971).

[213] B. Woratschek, W. Sesselmann, J. Kuppers, and G. Ertl, Phys. Rev. Lett. **55**, 1231 (1985).

[214] H. Petek and S. Ogawa, Annu. Rev. Phys. Chem. **53**, 507 (2002).

[215] M. Meot-Ner, Chem. Rev. **105**, 213 (2005).

[216] M. Fujita, Struct. Bond. **96**, 177 (2000).

[217] K. Biradha, Y. Hongo, and M. Fujita, Angew. Chem. Int. Ed. **39**, 3843 (2000).

[218] M. A. Keane and G. Webb, J. Catal. **136**, 1 (1992).

[219] M. M. Abu-Omar, A. Loaiza, and N. Hontzeas, Chem. Rev. **105**, 2227 (2005).

[220] S. V. Kryatov and E. V. Rybak-Akimova, Chem. Rev. **105**, 2175 (2005).

[221] R. Kawakami, E. Escorcia-Aparicio, and Z. Qiu, Phys. Rev. Lett. **77**, 2570 (1996).

[222] R. Kawakami, M. Bowen, H. Choi, E. Escorcia-Aparicio, and Z. Qiu, Phys. Rev. B **58**, R5924 (1998).

[223] D. J. Cram and J. M. Cram, Science **183**, 803 (1974).

[224] J.-M. Lehn, Struct. Bonding **6**, 1 (1973).

[225] J.-M. Lehn, Pure Appl. Chem. **50**, 871 (1978).

[226] K. Lee, H. Song, and J. T. Park, Acc. Chem. Res. **36**, 78 (2003).

[227] M. Abel, A. Dmitriev, R. Fasel, N. Lin, J. V. Barth, and K. Kern, Phys. Rev. B **67**, 245407 (2003).

[228] R. Fasel, R. G. Agostino, P. Aebi, and L. Schlapbach, Phys. Rev. B **60**, 4517 (1999).

[229] G. Gokel, *Crown Ethers and Cryptands* (The Royal Society of Chemistry, Cambridge, 1991).

[230] K. D. Schierbaum, T. Weiss, E. U. Thoden van Velzen, J. F. J. Engbersen, D. N. Reinhoudt, and W. Göpel, Science **265**, 1413 (1994).

[231] A. Friggeri, F. C. J. M. van Veggel, and D. N. Reinhoudt, Langmuir **14**, 5457 (1998).

[232] M. T. Rojas, R. Königer, J. F. Stoddart, and A. Kaifer, J. Am. Chem. Soc. **117**, 336 (1995).

[233] J. D. Faull and V. K. Gupta, Langmuir **17**, 1470 (2001).

[234] S. Flink and D. N. R. F. C. J. M. van Veggel, Adv. Mater. **12**, 1315 (2002).

[235] E. Menozzi, R. Pinalli, E. A. Speets, B. J. Ravoo, E. Dalcanale, and D. N. Reinhoudt, Chem. Eur. J. **10**, 2199 (2004).

[236] G.-B.Pan, J.-M. Liu, H.-M. Zhang, L.-J. Wan, Q.-Y. Zheng, and C.-L. Bai, Angew. Chem. Int. Ed. **42**, 2747 (2003).

[237] S. Höger, Chem. Eur. J. **10**, 1320 (2004).

[238] S. J. H. Griessl, M. Lackinger, M. Edelwirth, M. Hietschold, and W. M. Heckl, Single Mol. **3**, 25 (2002).

[239] J. Lu, S. B. Lei, Q. D. Zeng, S. Z. Kang, C. Wang, L. J. Wan, and C. L. Bai, J. Phys. Chem. B **108**, 5161 (2004).

[240] S. J. H. Griessl, M. Lackinger, F. Jamitzky, T. Markert, M. Hietschold, and W. M. Heckl, Langmuir **20**, 9403 (2004).

[241] W. S. Sim, P. Gardner, and D. A. King, J. Phys. Chem. **100**, 12509 (1996).

[242] L. Fomina, A. Reyes, and S. Fomine, Int. J. Quant. Chem. **89**, 477 (2002).

[243] G. Peng, J. van Elp, H. Jang, J. L. Que, and W. H. A. ans S. P. Cramer, J. Am. Chem. Soc. **117**, 2515 (1995).

[244] A. Seitsonen, unpublished.

[245] A. Lever, J. Chem. Soc. **1965**, 1821 (1965).

[246] P. Bruno, Phys. Rev. B **39**, 865 (1989).

[247] E. König and A. Chakravarty, Theoret. Chim. Acta **9**, 151 (1967).

Acknowledgements

I thank Professor Klaus Kern, the director of my thesis, for giving me the opportunity to work in his research group. His guidance, motivating energy and ongoing support has made it possible to accomplish this thesis.

I am grateful to Nian Lin who supervised this work. He was directly involved in planning and realization of the experiments as well as the analysis and interpretation of the data. His engagement and enthusiasm have been a constant motivation for me and his ideas contributed a lot to the success of this thesis. Furthermore, his careful reading of the manuscript is gratefully acknowledged.

I am also grateful to Johannes Barth who followed the projects and was closely involved in the data evaluation. His competence and fresh views have been a major source for advancing the whole concept. I truly appreciate his guidance in the preparation of the publications.

I thank my predecessor Alexandre Dmitriev as well as Hannes Spillmann and Magali Lingenfelder for introducing me to the mysteries of scanning tunneling microscopy and supramolecular chemistry. I also want to express my gratitude to the other present and former group members Franck Vidal, Frederic Leroy, Robin Ohmann and Dietmar Payer for fruitful discussions and their help in the lab. I thank you all for the nice and relaxed atmosphere and the time we shared in and outside the institute.

I also thank the other members of the jury for judging this thesis: Prof. H. Vogel, Dr. R. Fasel, and Dr. M. Ruben.

I am indebted to the colleagues in Bochum and Lausanne, particularly Thomas Strunskus and Pietro Gambardella, for their help in conducting synchrotron measurements on organic and metal-organic systems at BESSY II and ESRF in Berlin and Grenoble, respectively. In particular, I thank them for introducing me to the realms of surface chemistry and magnetism and the pleasant time at these dark places. My sincere gratitude also to Sylvain Clair, Stephane Pons, Jan Honolka, Peter Bencock and Stefan Stanescu with whom I shared a nice time at ESRF.

I am grateful to C. Cai and M. Ruben for providing some of the organic material. Moreover, I appreciate the exchange of ideas and fruitful collaboration with Mario Ruben.

The atmosphere in our department was always cooperatively and pleasant. For this, I thank all people working in Kern's group. Didi Payer, Stephan Rauschenbach and Sören Neubeck became more than good colleagues during my time in Stuttgart. It is a pleasure to work and spend the spare time with you.

Finally, I thank my family. Their support and love is the most important of all.

Curriculum vitae

Name	Sebastian Michael Stepanow
Date of Birth	November 22, 1977
Nationality	German
12/2005	Ph.D. Thesis, EPF Lausanne, Switzerland
2002-2005	Research assistant in the group of Prof Dr K. Kern at the Max-Planck-Institute for Solid State Research in Stuttgart, Germany
2002	Diploma thesis in the group of Prof Dr F. Bechstedt at the Institute for Solid State Theory and Theoretical Optics of the Friedrich-Schiller-University in Jena: "Optische Absorption von Supergittern in gekreuzten äußeren elektrischen und magnetischen Feldern"
1997-2002	Diploma studies in physics at Friedrich-Schiller-University in Jena, Germany
1996-1997	Military Service
1986-1996	High School at the Hermann-Matern-School and Domgymnasium Merseburg, Germany
1984-1986	Elementary School "Schule für Deutsch-Sowjetische-Freundschaft Rosenthal" in Merseburg, Germany

Publications

S. Stepanow, S. Glutsch, A. B. Hummel, C. Blöser, H. G. Roskos, and K. Köhler, "Semiconductor superlattice in crossed electric and magnetic fields", submitted.

M. Lingenfelder, H. Spillmann, A. Dmitriev, S. Stepanow, N. Lin, J. V. Barth, and K. Kern, "Towards surface-supported supramolecular architectures: Tailored coordination assembly of 1,4-benzenedicarboxylate and Fe on Cu(100)", Chem. Eur. J. **10**, 1913 (2004).

S. Stepanow, M. Lingenfelder, A. Dmitriev, H. Spillmann, E. Delvigne, N. Lin, X. Deng, C. Cai, J. V. Barth, and K. Kern, "Steering molecular organization and host-guest interactions using two-dimensional nanoporous coordination systems", Nat. Mater. **3**, 229 (2004).

S. Stepanow, T. Strunskus, M. Lingenfelder, A. Dmitriev, H. Spillmann, N. Lin, J. V. Barth, C. Wöll, and K. Kern, "Deprotonation-driven phase transformation in terephthalic acid self-assembly on Cu(100)", J. Phys. Chem. B **108**, 19392 (2004).

N. Lin, S. Stepanow, F. Vidal, J. V. Barth, and K. Kern, "Manipulating 2D metal-organic networks *via* ligand control", Chem. Comm. **2005**, 1681 (2005).

S. Stepanow, N. Lin, F. Vidal, A. Landa, M. Ruben, J. V. Barth, and K. Kern, "Programming supramolecular assembly and chirality in two-dimensional dicarboxylate networks on a Cu(100) surface", Nano Lett. **5**, 901 (2005).

F. Vidal, E. Delvigne, S. Stepanow, N. Lin, J. V. Barth, and K. Kern, "Chiral phase transition in two-dimensional supramolecular assemblies of prochiral molecules", J. Am. Chem. Soc. **127**, 10101 (2005).

A. Dmitriev, H. Spillmann, S. Stepanow, T. Strunskus, C. Wöll, A. P. Seitsonen, M. Lingenfelder, N. Lin, J. V. Barth, and Klaus Kern, ”Asymmetry induction by supramolecular self-assembly at surfaces: Mesoscopic organization of homochiral trimellate layers on Cu(100)”, submitted.

S. Stepanow, N. Lin, J. V. Barth, and K. Kern, ”Binding of organic species in two-dimensional metallosupramolecular receptor arrays - A molecular level investigation of host-guest interactions”, submitted.

S. Stepanow, N. Lin, J. V. Barth, and K. Kern , ”Surface-templated assembly of 2D metal-organic coordination networks”, in preparation.

N. Lin, S. Stepanow, and K. Kern, ”Rational design of two-dimensional nanoporous networks via ionic self-assembly of dicarboxylate linkers and Cs ions at a metal surface”, in preparation.

N. Lin, S. Stepanow, J. V. Barth, and K. Kern, ”Oxygen induced structural and chemical change of surface-supported carboxylate bridged dinuclear iron compounds”, in preparation.

T. Classen, M. Lingenfelder, T. Strunskus, S. Stepanow, N. Lin, C. Wöll, and K. Kern, ”Self-assembly of Di-Phenylalanine at Cu(100) and Cu(110) surfaces”, in preparation.

P. Gambardella *et al.*, ”Magnetism of metal-organic coordination structures at metal surfaces”, in preparation.

S. Stepanow, N. Lin, D. Payer, and K. Kern, ”Metal-organic honeycomb networks assembled via trigonal Fe-hydroxyl coordination on metal surfaces”, in preparation.